Title
Search for variation of the fine-structure constant and violation of Lorentz symmetry using atomic dysprosium

Author
Leefer, Nathan Alexander

Publication Date
2013

Peer reviewed|Thesis/dissertation

Search for variation of the fine-structure constant and violation of Lorentz symmetry using atomic dysprosium

by

Nathan Alexander Leefer

A dissertation submitted in partial satisfaction of the
requirements for the degree of
Doctor of Philosophy

in

Physics

in the

Graduate Division

of the

University of California, Berkeley

Committee in charge:

Professor Dmitry Budker, Chair
Professor Holger Müller
Professor Robert Harris

Spring 2013

Search for variation of the fine-structure constant and violation of Lorentz symmetry using atomic dysprosium

Nathan Alexander Leefer

Abstract

Search for variation of the fine-structure constant and violation of Lorentz symmetry using atomic dysprosium

by

Nathan Alexander Leefer

Doctor of Philosophy in Physics

University of California, Berkeley

Professor Dmitry Budker, Chair

We report on the spectroscopy of radio-frequency transitions between nearly-degenerate, opposite-parity excited states in atomic dysprosium (Dy). Theoretical calculations predict that these states are very sensitive to variation of the fine-structure constant, α, owing to large relativistic corrections of opposite sign for the opposite-parity levels. The near degeneracy reduces the relative precision necessary to place constraints on variation of α competitive with results obtained from the best atomic clocks in the world. Additionally, the existence of several abundant isotopes of Dy allows isotopic comparisons that suppress common-mode systematic errors. The frequencies of the 754-MHz transition in ^{164}Dy and 235-MHz transition in ^{162}Dy were measured over the span of two years. Linear variation of α is found to be $\dot{\alpha}/\alpha = (-5.8 \pm 6.9) \times 10^{-17}$ yr^{-1}, consistent with zero. The same data are used to constrain the dimensionless parameter k_α, characterizing a possible coupling of α to a changing gravitational potential. We find that $k_\alpha = (-5.5 \pm 5.2) \times 10^{-7}$, essentially consistent with zero and the best constraint to date.

The same data are used to report a joint test of local Lorentz invariance and the Einstein Equivalence Principle for electrons. We present many-body calculations which demonstrate that the energy splitting of these states is particularly sensitive to violations of both special and general relativity. Lorentz violation for electrons is limited at the level of 10^{-17}, matching or improving the best laboratory and astrophysical limits by up to a factor of 10, and gravitational redshift anomalies for electrons to the level of 10^{-8}. With some enhancements, our experiment may be sensitive to Lorentz violation at the level of 9×10^{-20}.

We also report measurements of the differential polarizability between the nearly degenerate, opposite parity states. The differential scalar and tensor polarizabilities due to additional states were measured for the $|M| = 7, \ldots, 10$ sublevels in ^{164}Dy and ^{162}Dy and determined to be $\overline{\boldsymbol{\alpha}}^{(0)}_{BA} = 180\,(45)_{\text{stat}}\,(8)_{\text{sys}}$ mHz cm^2/V^2 and $\overline{\boldsymbol{\alpha}}^{(2)}_{BA} = -163\,(65)_{\text{stat}}\,(5)_{\text{sys}}$ mHz cm^2/V^2, respectively. The average blackbody radiation induced Stark shift of the Zeeman spectrum was measured around 300 K and found to be $-34(4)$ mHz/K and $+29(4)$ mHz/K for the ^{164}Dy and ^{162}Dy isotopes, respectively. We conclude that ac-Stark related systemat-

ics will not limit the precision of a search for variation of the fine-structure constant, using dysprosium, down to the level of $|\dot{\alpha}/\alpha| = 2.6 \times 10^{-17}$ yr^{-1} for a one-year experiment.

To my mom and dad and brother.

Contents

List of Figures

List of Tables

Acknowledgments

In the Fall of 2005 Dima Budker agreed to let me work as an undergraduate researcher in his group, despite my complete lack of experience or qualifications. In the years since he has shown no end of kindness and patience, even agreeing to let me do graduate work in his group. He has taught me how to be a scientist, and at every turn has gone out of his way to provide opportunities to further my academic career. His enthusiasm for all areas of physics and his intuition for solving complex problems is an inspiration. I look forward to many future years of productive collaboration, and thank him for taking a chance on me.

The first day of work as an undergraduate I met Arman Cingöz, then a graduate student and my 'in the lab' mentor for many years while I was both an undergraduate and gradute student. On that particular day Arman was moving electronics out of some racks. He gave me a screwdriver, and after I successfully inserted the sharp end into an appropriate screw head he breathed a sigh of relief, "OK, good. You know *something*." Thanks to his mentorship I now know a great deal more (and his expectations did eventually increase).

The results of this dissertation would not be possible without the experimental apparatus that Arman brought to life during his own dissertation work with the group. His attention to detail produced an apparatus that is likely to continue producing good science for years to come. In addition to his brilliance as a physicist, Arman taught me the value of hard work and tenacity in the face of overwhelming challenges.

Damon English was also an invaluable resource of ideas and advice over the years, particuarly in the transitional period after Arman left. There is no doubt that Damon helped me through a great many rough patches. His kindness and reliable humor has been missed since he moved on from the group.

Beyond these individuals, I also thank the entire Budker group, past and present. It is a dynamic and always changing group of people. I have met people from all corners of the globe and am grateful for the opportunity to learn their perspective on science and life. Dimitri Dounas-Frazer, in particular, is a valued friend who can always be relied upon for insight into any problem. Christian Weber was instrumental in running the experiment for the past two years and finishing the work detailed in Chapter 5 of this dissertation. Kasper Jensen and Pauli Kehayis have been great to work with this last year, and Dima is owed another thanks for allowing these collaborations, even though nitrogen-vacancy centers have absolutely nothing to do with this dissertation. I hope that many of these collaborations will continue into the future.

The administrative staff of the Physics Department at Berkeley is truly outstanding, and without them good research would be impossible. The machinists in the Main Shop have been an amazing resource and a great pleasure to work with, thanks to their expertise and eagerness to tackle difficult engineering problems (for a physicist).

Ultimately, I am most grateful for the love and support from my family and friends. You know who you are, and I thank you.

1 — The search for new physics

The Standard Model (SM) of particle physics and general theory of relativity (GR) are two theories of modern physics that have proven remarkably successful at describing most of the observable universe. Taken together they can describe both the large-scale structure of the Universe and the myriad subatomic particles and their interactions, including the most recent confirmation of the so-called Higgs boson [1, 2], first predicted nearly 50 years ago [3].

Despite the success of each theory within its respective domain, however, the movement to find a single unified theory to describe all known interactions persists. The reason is two fold. The reductionist movement to more simplicity has worked remarkably well in the unification of the electromagnetic, weak, and strong forces in the SM. Given the inherently quantum nature of these three forces and the universal coupling of gravity to energy, it seems natural that a quantum description of gravity should also exist. The second reason is that GR and the SM cannot be reconciled to describe phenomena where both gravity and quantum effects are equally important, such as the singularities associated with black holes or the epochs immediately following the Big Bang [4]. In addition to this, evidence has long been accumulating that indicates our understanding of the Universe is imperfect. The nature of dark matter [5] and dark energy [6], for instance, which together constitute roughly 95% of energy content in the Universe, is still poorly understand [7].

In this dissertation we focus our attention on experiments dedicated to phenomenological searches for previously unobserved physics. The two main results fall into the category of experiments testing two components of the Einstein equivalence principle (EEP), which states that the results of any nongravitational experiment should be independent of of where it is carried out in spacetime (local position invariance) or in what direction it is oriented or traveling (local Lorentz invariance).

The main results are presented first in Chapters 2 and 3. A discussion of systematic effects can be found in Chapter 4, with a separate discussion of ac-Stark related systematics in Ch. 5.

1.1 Varying constants

Variation of fundamental ‘constants’ was first proposed by Dirac in 1937 with the Large Numbers Hypothesis (LNH) [8], an early formulation of what is now know as a ‘hierarchy

problem' [9]. The hypothesis was founded on the premise that a unified theory of physics must be able to explain the existence of extremely large dimensionless ratios of fundamental quantities in our universe. Dirac posed this problem by considering the ratio of the electromagnetic and gravitational forces between a proton and electron in a hydrogen atom

$$\frac{e^2/a_0^2}{Gm_e m_p/a_0^2} \sim 10^{39}, \tag{1.1}$$

where e and m_e are the electron charge and mass, m_p is the proton mass, a_0 is the Bohr radius, and G is the Newtonian constant of gravitation. Similarly, the age of the universe, $\tau_u \sim 10^{18}$ s, expressed in units of a characteristic atomic time, τ_a, produces the curious result

$$\frac{\tau_u}{\tau_a} = \frac{\tau_u}{a_0/(\alpha c)} \sim 10^{39}, \tag{1.2}$$

where α is the fine-structure constant and c is the speed of light. This coincidence prompted Dirac to propose that large dimensionless ratios are not fundamental constants but rather functions of the age of the Universe, specifically that any ratio or dimensionless quantity which is approximately $(10^{39})^n$ scales with the age of the universe according to $(\tau_u)^n$. Reasoning along these lines produces a Newtonian gravitation constant that scales inversely propotional to τ_u. This would give a present day fractional variation of

$$\frac{\dot{G}}{G} \sim -10^{10}\,\mathrm{yr}^{-1}. \tag{1.3}$$

Arguments along similar lines were also made for variation of other fundamental constants, such as the number of nucleons in the Unverse, $N \sim 10^{78} \propto \tau_U^2$, which encounters the problem of requiring continuous creation of matter in the universe [10]. Ultimately, modern experiments based on laser ranging of the Earth-Moon distance have constrained present day variation of G at the level of $|\dot{G}/G| < 10^{-12}$ yr^{-1} [11]. Although Dirac's hypothesis has been effectively ruled out by these bounds, it motivated many of the early experimental searches for variation of fundamental constants.

Several modern attempts have been made to theoretically motivate variation of fundamental constants [12, 13]. One example is string theories based on Kaluza-Klein models, which introduce extra compact dimensions to the usual $3+1$ spacetime dimensions in order to unify the fundamental forces [14]. A consequence of this is a relationship between the electromagnetic coupling (fine-structure) constant, α, and G that depends on the topology and size of the extra dimensions. Any variation of the size of the extra dimensions could manifest as a variation of G and/or α [15].

Astrophysical studies

In 1999, a study of Mg I, Mg II, and Fe II absorption lines in quasar emission spectra, over a redshift range of $0.5 < z < 1.6$, began to hint at a smaller value of α in the past,

of size $\Delta\alpha/\alpha = (-1.1 \pm 0.4) \times 10^{-5}$ [16]. The data were acquired using the Keck I 10 m telescope in Hawaii and was the first application of the so-called many-multiplet (MM) method, which sought to compare different transitions within absorbing systems in order to guard against systematic errors [17, 18]. Over the next several years this group continued to improve their analysis methods and incorporate new data [19, 20], ultimately reaching the result of $\Delta\alpha = (-0.54 \pm 0.12) \times 10^{-5}$ from an analysis of 128 absorbing systems over the redshift range $0.2 < z < 3.7$ [21].

Competing groups during this time carried out a parallel study using data acquired with the European Southern Observatory (ESO) Kueyen 8.2 m telescope. An analysis of absorption lines, using the same MM method, over the redshift range $0.4 \leq z \leq 2.3$ found $\Delta\alpha/\alpha = (-0.06 \pm 0.06) \times 10^{-5}$ [22, 23], although there was significant debate over the estimation of uncertainties [24, 25]. A study of a single system absorbing system at $z = 1.15$ found $\Delta\alpha/\alpha = (0.0 \pm 0.3) \times 10^{-5}$ [26].

Within the past several years an attempt has been made to reconcile the conflicting results. A joint analysis of data, old and new, acquired from both observatories is consistent with a spatial dependence of α, described by a spatial 'dipole' of the form

$$\frac{\Delta\alpha}{\alpha} = (1.1 \pm 0.25) \times 10^{-6} r \cos\Theta, \tag{1.4}$$

where r is the distance from Earth in units of 10^9 lightyears and Θ is the angle from the direction right ascension 17.5±0.9 h, declination −58±9 degrees [27]. Such a spatial variation could manifest as a temporal variation of α in atomic clock experiments, where the magnitude is determined by the average direction and speed of the solar system with respect to this dipole. Unfortunately the steepest gradient of α points in the general direction of the galactic center, such that $\dot{\alpha}/\alpha = -(0.07 \pm 0.1)(1.4 \times 10^{-18})$, where the primary source of uncertainty arises from the direction of the dipole [28]. The sensitivity necessary to see such a small effect will not be achieved with any current technology and is many decades into the future.

The conflicting results mentioned so far are likely indicative of the significant systematic uncertainties that contribute to observational studies. The experiments must contend with not only the technical limitations of the measuring devices, such as nonlinearities of the spectrographs used in astrophysical studies, but also make significant assumptions regarding the local environments of absorbing systems up to 10 billion light years away. Any given interpretation of observations as evidence for or against variation of constants will always be subject to justifiable skepticism without the ability to perform repeatable and controlled experiments.

Laboratory studies

A number of laboratory experiments have been carried out since the first astrophysical results were published. The majority of these rely on the comparison of transition frequencies in ions, atoms, and molecules and are complementary to the development of new clock

technology. Although all atomic energies are proportional to α^2 through the overall Rydberg scaling, this dependence drops out in the comparison of any two transition frequencies. The observable dependence on fundamental constants enters through the fine-structure and hyperfine-structure corrections of order α^4. The hyperfine-structure corrections also introduce two more dimensionless fundamental constants as will be shown shortly.

The frequency of an electronic transition in an atom, that is a transition between states split by the normal Coulomb interaction, can be expressed

$$\omega_{elec} = R_\infty c \cdot A_{elec} \cdot F_{elec}(\alpha), \tag{1.5}$$

where R_∞ is the Rydberg constant, c is the speed of light, A_{elec} is a dimensionless factor dependent on the atomic structure, and $F_{elec}(\alpha)$ is a correction factor that contains relativistic and manybody effects that depend on α. The fractional variation of this frequency can then be written

$$\begin{aligned} \frac{\delta\omega_{elec}}{\omega_{elec}} &= \frac{1}{F_{elec}(\alpha)} \frac{\partial F_{elec}(\alpha)}{\partial \alpha} \delta\alpha \\ &= \left(\alpha \frac{\partial}{\partial \alpha} \ln F(\alpha) \right) \frac{\delta\alpha}{\alpha}. \end{aligned} \tag{1.6}$$

The frequency of a hyperfine transition within an electronic state can be written

$$\omega_{hfs} = R_\infty c \cdot A_{hfs} \cdot g \cdot \frac{m_e}{m_p} \cdot \alpha^2 \cdot F_{hfs}(\alpha), \tag{1.7}$$

where A_{hfs} is again a dimensionless factor independent of any fundamental constants, g is the nuclear g-factor, and m_e/m_p is the electron-proton mass ratio. The variation of this transition frequency can be expressed in a similar manner to Eq. (1.6) where

$$\frac{\delta\omega_{hfs}}{\omega_{hfs}} = \frac{\delta g}{g} + \frac{\delta(m_e/m_p)}{(m_e/m_p)} + \left(2 + \alpha \frac{\partial}{\partial \alpha} \ln F_{hfs}(\alpha) \right) \frac{\delta\alpha}{\alpha}. \tag{1.8}$$

In Ref. [29] it was shown that g and m_p can be linked to the fundamental quantities Λ_{QCD}, the mass scale of quantum chromodynamics (QCD), and the quark mass $m_q = (m_u + m_d)/2$, where $m_{u,d}$ are the masses of the up and down quarks.

For the purpose of parametrizing dependence on fundamental constants, the ratio of any two transition frequencies can be conveniently expressed

$$X \equiv \frac{\omega_1}{\omega_2} = A \cdot \alpha^{K_\alpha} \cdot \left(\frac{m_e}{m_p} \right)^{K_e} \cdot \left(\frac{m_q}{\Lambda_{QCD}} \right)^{K_q}, \tag{1.9}$$

where A is a scale factor and the $K_{\alpha,e,q}$ are sensitivity coefficients. We have chosen to maintain the dependence on m_e/m_p simply because it is traditionally reported as a constrained quantity in the literature. In the limit of small variations, the fractional change of this ratio can be written

$$\frac{\Delta X}{X} \approx \Delta \ln X = \frac{\Delta\omega_1}{\omega_1} - \frac{\Delta\omega_2}{\omega_2} = K_\alpha \frac{\Delta\alpha}{\alpha} + K_e \frac{\Delta(m_e/m_)}{(m_e/m_p)} + K_q \frac{\Delta(m_q/\Lambda_{QCD})}{(m_q/\Lambda_{QCD})}. \tag{1.10}$$

The interpretation of any frequency comparison as a bound on variation of constants is dependent on accurate calculation of the sensitivity coefficients. State of the art methods rely on a combination of configuration interaction and many-body perturbation theory methods [30]. As a rule of thumb, electronic transitions in heavy atoms are highly sensitive to variation of α due to significant relativistic corrections to energy levels, and electronic transitions in light atoms are insensitive to variation of α based on similar reasoning. The current most stringent bound of $\dot{\alpha}/\alpha = (-1.6 \pm 2.3) \times 10^{-17}$ yr^{-1} comes from a comparison of optical transitions in the heavy Hg^+ ion and relatively light Al^+ ion [31]. Hyperfine transitions within a given electronic state, consider the ground state splitting in Rb, Cs, or H, are roughly equally sensitive to all three parameters. A listing of various experiments and the appropriate sensitivity coefficients can be found in Table 2.1.

1.2 Violation of Lorentz symmetry

Violation of Lorentz symmetry in this work is analyzed within the phenomenological framework of the Lorentz-violating Standard Model Extension (SME) [32, 33]. The SME is motivated by the assumption that the Standard Model (SM) of particle physics is the low-energy limit of a a grand unified theory (GUT) that provides a quantum description of gravity. Although it has been shown that some of proposed GUTs contain mechanisms for spontaneous Lorentz symmetry [34], the SME is independent of the underlying theory.

Construction of the SME assumes that any GUT must reproduce the SM in a low energy limit. This begins with the construction of a particle Lagrangian density that contains the usual SM fields and Lorentz tensors, and adds all possible combinations of these with background coupling coefficients that serve to break Lorentz invariance. While there are infinitely many such combinations, we will focus on terms only up to first order in the covariant derivative $D^\nu \equiv \partial^\nu - qA^\nu$. In the SME, Lorentz violation (LV) must considered separately for the different particle families, but in this work we restrict our attention to Lorentz violation for electrons and its implications for atomic clock experiments. The Lagrangian density for an electron in the minimal SME can be written [33, 35]

$$\mathcal{L} = \frac{1}{2} i\bar{\psi}\Gamma_\nu \overleftrightarrow{D^\nu} \psi - \bar{\psi} M \psi, \tag{1.11}$$

where ψ is a four-component spinor, the γ^ν are Dirac gamma matrixes, and $f\overleftrightarrow{D^\nu}g \equiv fD^\nu g - (D^\nu f)g$. The $M \equiv m + a_\mu\gamma^\mu + b_\mu\gamma_5\gamma^\mu + \frac{1}{2}H_{\mu\nu}\sigma^{\mu\nu}$ and $\Gamma_\nu \equiv \gamma_\nu + c_{\mu\nu}\gamma^\mu + d_{\mu\nu}\gamma_5\gamma^\mu$ contain the Lorentz violating effects in the coefficients a_μ, b_μ, $H_{\mu\nu}$, $c_{\mu\nu}$, and $d_{\mu\nu}$. Coefficients excluded by gauge invariance and renormalizability are not included in this construction [35].

The formulation of the Lagrangian density in Eq. (1.11) allows experiments from a range of disciplines to be compared on equal footing. The full range of Lorentz-violating experimental signatures is beyond the scope of this work, and a comprehensive review of up-to-date experimental results can be found in Ref. [36]. We instead focus our attention on the massless $c_{\mu\nu}$ electron coefficient. This coefficient has the effect of changing the energy-momentum (dispersion) relation for an electron in an anisotropic manner. This leads to predictable modifications of well known effects in electrodynamics, and some of the best bounds on $c_{\mu\nu}$ come from studies of synchotron radiation and inverse Compton scattering of ultrarelativistic electrons from astrophysical sources [37, 38].

In this work we are interested in the effect of $c_{\mu\nu}$ on electrons bound in atoms. The experimental signature of the modified dispersion relationship in these systems is a shift of bound states energies that can be detected by measuring transition frequencies between states. In Ref. [35] the authors perform a series of Foldy-Woutheysen transformations [39, 40] in order to extract the modification to the non-relativistic, free-electron Hamiltonian due to LV:

$$\delta h = -mc^2 c_{00} + (c_{j0} + c_{0j}) p_j c - \left(c_{jk} + \frac{1}{2} c_{00} \delta_{jk} \right) \frac{p_j p_k}{m}, \tag{1.12}$$

where p and m are the electron momentum and mass, respectively, and c without subscripts is the speed of light. Indices are chosen such that greek indices span $\mu = 0, 1, 2, 3$, roman indices represent spacelike components $j, k = 1, 2, 3$, and summation over repeated indices is implied.

The observable Lorentz-violating effects are expected to be suppressed by some power of the characteristic GUT energy scale, assumed to be order of the Planck mass $M_p \sim 10^{18}$ GeV, relative to the SM electroweak energy scale, $m_w \sim 10^2$ GeV. This allows the Hamiltonian modification to be treated perturbatively for electrons in atomic states, where the first-order energy shift of an atomic state m is given by $\langle m|\delta h|m\rangle$. Of the three terms in Eq. (1.12), the first generates an unobservable constant shift and the second is zero because $\langle \vec{p} \rangle = 0$ for bound states. The second term might give rise to spontaneous mixing between opposite parity atomic states that could be detected with standard Stark-interference techniques [41], but such an effect is likely to be unobservable based on the existing bounds on $c_{\mu\nu}$. The remaining observable energy shift is then governed by the third term

$$\delta h = -\left(c_{jk} + \frac{1}{2} c_{00} \delta_{jk} \right) \frac{p_j p_k}{m}. \tag{1.13}$$

The quantities c_{jk}, δ_{jk}, and $p_j p_k$ are rankd-2 tensors, and Eq. (1.13) can be expressed in the irreducible spherical tensor representation [42]

$$\delta h = -C_0^{(0)} \frac{T_0^{(0)}}{2m} - \sum_{q=-2}^{2} \frac{(-1)^q}{6m} C_q^{(2)} T_{-q}^{(2)}, \tag{1.14}$$

where

$$C_0^{(0)} = c_{00} + \tfrac{2}{3}c_{jj}, \qquad C_0^{(2)} = (c_{jj} - 3c_{33})$$
$$C_{\pm1}^{(2)} = \pm 3(c_{31} \pm ic_{32}), \qquad C_{\pm2}^{(2)} = 3(c_{11} - c_{22} \pm ic_{12}),$$

and

$$T_0^{(0)} = \vec{p}^{\,2}, \qquad T_0^{(2)} = \vec{p}^{\,2} - 3p_3^2$$
$$T_{\pm1}^{(2)} = \pm p_3(p_1 \pm ip_2), \qquad T_{\pm2}^{(2)} = (p_1^2 - p_2^2)/2 \pm ip_1p_2.$$

For bound states, only the $T_0^{(0)}$ and $T_0^{(2)}$ have nonzero matrix elements (the other operators induce transitions between atomic states), so the energy shift can be written

$$\delta\epsilon_m = -C_0^{(0)}\frac{\langle m|T_0^{(0)}|m\rangle}{2m} - C_0^{(2)}\frac{\langle m|T_0^{(2)}|m\rangle}{6m}. \tag{1.15}$$

The quantity $\langle m|T_0^{(2)}|m\rangle$ is worth considering, as this is the quadrupole moment of the electron *momentum* in state m. The axis of the quadrupole moment, determined by the quantization axis chosen for an experiment, represents a prefered alignment of the electron momentum. As this axis changes with respect to a stationary coordinate system in which $C_0^{(2)}$ is constant, the energy shift of state m will undergo a corresponding change. An observable frequency shift of a transition between two atomic states, $\delta\omega_{mn} = (\delta\epsilon_m - \delta\epsilon_n)/\hbar$, therefore requires that states m and n have different electron momentum quadrupole moments. Note also that the magnitude of a non-zero $T_0^{(2)}$ operator can be expected to have a magnitude on the order of $\vec{p}^{\,2}$. The best experiments seeking to constrain $c_{\mu\nu}$ with this method will likely study electronic transitions in heavy atoms, where the electron kinetic energy scales roughly quadratically with the nuclear charge, Z.

The constraints on Lorentz violation for electrons in this thesis are complementary to studies of Lorentz violation for photons. It has been shown in Ref. [43] that a suitable coordinate redefinition can map Lorentz violating effects for photons into the $c_{\mu\nu}$ coefficient in the fermion sector. Optical cavity experiments that constrain non-birefringent anisotropies of photon propagation can then be interepreted as constraints on $c_{\mu\nu}$ for electrons with this transformation. Furthermore, optical cavity experiments that use matter-filled cavities are sensitive to $c_{\mu\nu}$ as it modifies electronic states in the material of the cavity, generating anisotropic changes in cavity length [11, 44, 45].

1.3 Dysprosium

Atomic dysprosium (Dy) is a rare-earth element with nuclear charge $Z = 66$ and seven naturally abundant, stable isotopes with mass numbers $A = 156$, 158, 160, 161, 162, 163, 164. Dysprosium has long been a system of experimental interest, beginning with proposals to study nuclear electric-dipole moments [46] in ^{161}Dy, and later attempts to measure atomic

parity nonconservation effects [41]. Recent demonstrations of the ability to laser cool [47] and magnetooptically trap [48] Dy has made it an ideal system to study strongly interacting degenerate gases [49], owing to the large ground-state magnetic moment $\mu \sim 10\mu_B$.

For the purpose of this work we focus on a coincidence of atomic energy levels in Dy that is unique within the existing spectroscopic literature. Two distinct electronic states, the even parity $4f^{10}5d6s, J = 10$ (state A) and odd parity $4f^{9}5d^{2}6s, J = 10$ (state B) states, are almost completely degenerate at an energy of $E = 19,797.96$ cm^{-1} [50]. The occcurrence of this 'accidental' degeneracy is random chance arising from the high density of excited states in Dy and large relativistic corrections to electron energies that are on the order of optical frequencies, $\sim 10^{15}$ Hz [51].

This system permits an electric dipole transition between the even parity (state A) and odd parity (state B) states, making the system nearly ideal for constraining variation of α or Lorentz violation for electrons. The large and opposite-sign relativistic corrections to A and B [51] make the energy splitting sensitive to variation of α, and the large electron-momentum quadrupole moments in these states (see Ch. 4 or Ref. [52]) make the splitting sensitive to the Lorentz violating $c_{\mu\nu}$ tensor. In addition, the small size of the energy splitting drastically reduces the measurement precision necessary to place competitive constraints on these effects. Rather than constraining the relative variation of A and B by measuring their energy above the ground state very precisely, we can directly measure the almost negligible energy difference between them at a much lower level of precision. As a reference, the best constraints on variation of α or $c_{\mu\nu}$ typically require measurement precision at the level of 10^{-17} or 10^{-16} [11, 31, 53]. The results in this work are based on measurement precision at the level of 10^{-10}.

Statistical sensitivity

Based on this statement of relative precision, it is natural to ask why we can't simply measure the Dy splitting at the level of 10^{-17} as well, place definitive constraints on the effects under discussion, and move on. There is no general principle prohibiting such a measurement precision in nearly degenerate sytems, measurements of the hyperfine splittings in Rb and Cs have achieved this level of precision, but in the specific case of dysprosium the limitation is one of practical statistics. The fundamental uncertainty associated with measuring the frequency of an atomic resonance can be estimated as the natural linewidth of the resonance, γ. This uncertainty can only be reduced by repeated measurements of the transition frequency,

$$\sigma_\omega = \frac{\gamma}{\sqrt{N}}, \tag{1.16}$$

where N is the number of measurements made. In our spectroscopy of the B to A transition we typically perform measurements on 10^9 atoms/second. State B is metastable, $\tau_B > 200\mu$s, so the natural linewidth of the transition is determined by the lifetime of state A,

$\tau_A \sim 8\mu$s [54]. We now write

$$\frac{\sigma_\omega}{2\pi} = \frac{1}{2\pi}\frac{1/\tau_A}{3\times 10^5\sqrt{T}}, \tag{1.17}$$

where T is the measurement time and the factors of 2π are included to express the result in units of real frequency. Evaluating terms we find

$$\frac{\sigma_\omega}{2\pi} = \frac{0.6}{\sqrt{T}}\,\text{Hz}. \tag{1.18}$$

For a typical measurement time of one hour, we can reasonaly expect to reach 10 mHz uncertainty, or 10^{-11} precision for a 1 GHz transition frequency. Improving this to a precision of 10^{-17} would take roughly 100 million years, a timescale on which systematic effects will likely play a significant role.

Procedure

The experimental details of the rf-spectroscopy have been exhaustively detailed in a number of previous publications [55–59] and theses [60, 61]. Discussions of the method for determining the transition frequency have been included in Appendix A and Appendix B, and a more detailed discussion of the experimental apparatus is included in Sec. 5.5. Here we include a brief overview of the experiment. A partial energy level diagram showing states of interest in Dy is shown in Fig. 1.1. The metastable state B can be populated by two laser transitions at 833-nm and 669-nm, followed by a spontaneous decay into B with 30% branching ratio 1.1. The spectroscopy is performed on a thermal beam of Dy atoms, and efficient laser excitation of the entire Doppler distribution is achieved using an adiabatic passage technique demonstrated to have near 100% efficiency [62]. Atoms in state B can then be resonantly excited to A by applying a radio-frequency electric field. The exact transition frequency depends on the isotope under consideration and can range from 3 MHz in ^{163}Dy to > 2 GHz [54]. A listing of the $B \to A$ transition frequencies for the most abundant isotopes and the relative laser tunings necessary to populate state B for each transition can be found in Table 1.1. Once atoms are in state A they return to the ground state with a natural lifetime of $\sim 8\mu$s. Multiple decay paths to the ground state exist, with the two dominant paths ending in the emission of a 626-nm or 564-nm photon. The current experiment uses the 564-nm fluorescence to probe the transition (see Appendix A).

Isotope comparisons

The degeneracy between A and B is so complete that isotope dependent shifts of energy levels can reverse the relative energies of A and B. The dependence of the sign of $\epsilon_B - \epsilon_A$ on isotope presents a powerful tool for rejection of systematic effects. The sensitivity of A and B to variation of α or $c_{\mu\nu}$ is isotope independent [55], thus the sign and magnitude of $\Delta\epsilon_A$ and $\Delta\epsilon_A$ is the same in all isotopes. The magnitude of the transition frequency

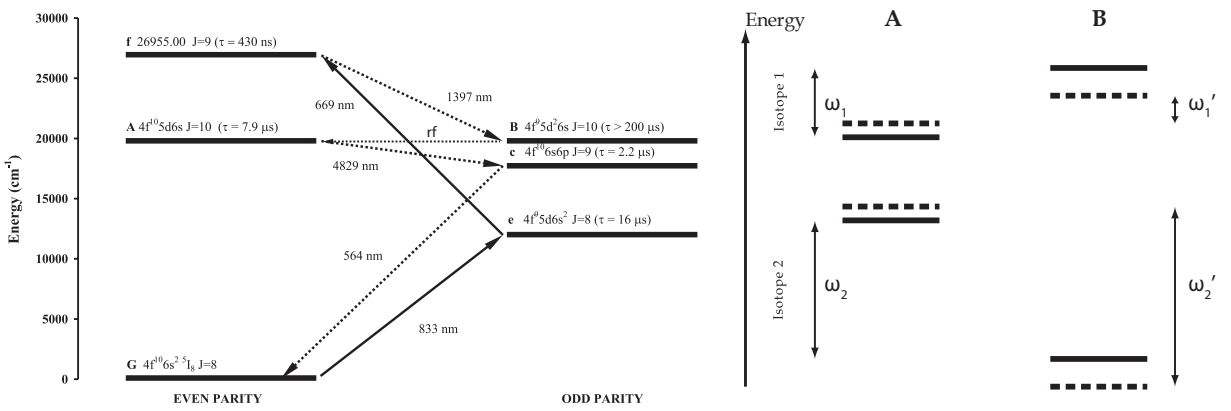

Figure 1.1: Relevant energy levels in atomic dysprosium. The expanded energy scale on the right demonstrates how the opposite sign of the energy splitting between states A and B in certain isotopes of Dy can be used to guard against systematic effects. A change in α or a non-zero $c_{\mu\nu}$ causes the magnitudes of the frequencies ω_1 and ω_2 to decrease and increase, respectively. Any observed frequency shift that does not obey the expected isotopic sign dependence can be ruled out as a systematic effect.

between A and B, however, will change with a sign determined by the sign of $\epsilon_B - \epsilon_A$. This is illustrated in Fig. 1.1. Comparing transition frequencies in different isotopes, therefore, allows systematic effects that do not shift all transition frequencies according to the expected relative sign dependence to be rejected. In the current work we compare the -234.7 MHz transition in ^{162}Dy and 753.5 MHz transition in ^{164}Dy, where the frequency is considered positive for $\epsilon_B > \epsilon_A$. Extending the work to include more isotopes will increase the fidelity of systematic rejection.

ν_{rf} (MHz)	$\|d_F\|/\|d_J\|$	Mass No. (Abund.)	F_A	F_B	883 nm detuning (MHz)	669 nm detuning (MHz)
-1328.6	1.00	160 (2%)	10.0	10.0	-2487	2242
-1856.4	0.15		7.5	8.5	-2493	2908
-1714.7	1.04		11.5	11.5	-2256	1202
-1249.7	0.99		10.5	10.5	-2486	1718
-962.3	0.15		12.5	11.5	-2256	1202
-791.5	0.94		9.5	9.5	-2549	2293
-349.2	0.89	161 (19%)	8.5	8.5	-2493	2908
-172.7	0.19		11.5	10.5	-2486	1718
68.9	0.86		7.5	7.5	-2360	3545
514.0	0.20		10.5	9.5	-2549	2293
1096.9	0.19		9.5	8.5	-2493	2908
1576.0	0.15		8.5	7.5	-2360	3545
-234.7	1.00	162 (26%)	10.0	10.0	-1200	1082
-1967.8	0.15		12.5	11.5	-1214	1620
-1581.3	0.86		7.5	7.5	-154	-1080
-1134.9	0.89		8.5	8.5	-532	-633
-609.7	0.94		9.5	9.5	-866	-47
-363.2	0.15	163 (25%)	7.5	8.5	-532	-633
3.1	0.99		10.5	10.5	-1110	698
504.6	0.19		8.5	9.5	-866	-47
713.1	1.04		11.5	11.5	-1214	1620
1531.0	1.10		12.5	12.5	-1122	2740
1543.9	0.20		9.5	10.5	-1110	698
753.5	1.00	164 (28%)	10.0	10.0	0	0

Table 1.1: Calculated E1 transition frequencies < 2 GHz using the hyperfine constants and isotope shifts from Ref. [54]. Positive frequency is chosen to mean $\epsilon_B > \epsilon_A$. Reduced matrix elements are denoted by $\|d_F\|$ and $\|d_J\| = 1.5(1) \times 10^{-2}$ ea$_0 \approx 19$ kHz/(V/cm). The last two columns indicate the frequencies of the 833-nm and 669-nm lasers necessary to optimally populate atoms into state B for each rf transition, relative to the ^{164}Dy transition frequencies. For hyperfine transitions these tunings are chosen for the strongest transitions where $\Delta F = \Delta J$.

2 — Variation of α

2.1 New limits on variation of the fine-structure constant using atomic dysprosium

We report on the spectroscopy of radio-frequency transitions between nearly-degenerate, opposite-parity excited states in atomic dysprosium (Dy). Theoretical calculations predict that these states are very sensitive to variation of the fine-structure constant, α, owing to large relativistic corrections of opposite sign for the opposite-parity levels. The near degeneracy reduces the relative precision necessary to place constraints on variation of α competitive with results obtained from the best atomic clocks in the world. Additionally, the existence of several abundant isotopes of Dy allows isotopic comparisons that suppress common-mode systematic errors. The frequencies of the 754-MHz transition in ^{164}Dy and 235-MHz transition in ^{162}Dy were measured over the span of two years. Linear variation of α is found to be $\dot{\alpha}/\alpha = (-5.8 \pm 6.9) \times 10^{-17}$ yr^{-1}, consistent with zero. The same data are used to constrain the dimensionless parameter k_α, characterizing a possible coupling of α to a changing gravitational potential. We find that $k_\alpha = (-5.5 \pm 5.2) \times 10^{-7}$, essentially consistent with zero and the best constraint to date.

This chapter is currently under review for publication in Physical Review Letters. The preprint is available at `http://arxiv.org/abs/1304.6940`

Variation of fundamental constants was first formulated by Dirac as the Large Numbers hypothesis [8, 10]. The observation that dimensionless ratios of quantities such as the age of the universe to atomic time scales and the electromagnetic to gravitational force between a proton and electron were of the same order of magnitude, $\sim 10^{40}$, led to the hypothesis that these ratios were functions of the age of the Universe. A consequence of this hypothesis is a gravitational constant, G, that scales inversely proportional to the age of the universe. Although modern experiments based on lunar ranging [63] have ruled out present-day variation of such magnitude, the variability of fundamental constants remains an active area of theoretical and experiment research. Any such variation would be a violation of the Einstein Equivalence Principle (EEP) and an indication of physics beyond General Relativity (GR) and the Standard Model (SM) of particle physics [12, 13].

Changing constants would manifest in a wide range of physical observables. The dimensionless electromagnetic-coupling constant, the fine-structure constant, α, is of particular importance due to the implications of its variation on clock-comparison experiments. Any variation of α would lead to a change in the relative frequencies of co-located clocks even in the absence of external fields. This is forbidden by an assumption of EEP. In this letter we report new constraints on variation of α with respect to time and changing gravitational potential from a comparison of radio-frequency transitions in two isotopes of atomic dysprosium (Dy) [54, 55]. These new results improve on our earlier constraints [56, 57] by almost two orders of magnitude and are competitive with existing limits from other experiments [31, 64–70].

The most stringent laboratory constraints on variation of fundamental constants come from clock-comparison experiments. We restrict our attention to clocks based on transitions in atoms and molecules. The ratio of any two such clock frequencies can be written [29]

$$X = \frac{\omega_1}{\omega_2} = A \times \alpha^{K_\alpha} \mu_e^{K_e} \mu_q^{K_q}, \tag{2.1}$$

where A is a dimensionless factor dependent on atomic structure, $\mu_e = m_e/m_p$ is the electron-proton mass ratio, and $\mu_q = m_q/\Lambda_{QCD}$ is ratio of the quark mass to QCD-mass scale. The dimensionless constants μ_e and μ_q are important for comparisons involving transitions with hyperfine structure [64, 69] or molecular transitions [71]. The change of this ratio can be written as

$$\Delta \ln X = K_\alpha \Delta \ln \alpha + K_e \Delta \ln \mu_e + K_q \Delta \ln \mu_q, \tag{2.2}$$

where the sensitivity coefficients $K_{\alpha,e,q}$ depend on the particular frequency ratio under consideration. A summary of coefficients for various comparisons can be found in Table 2.1.

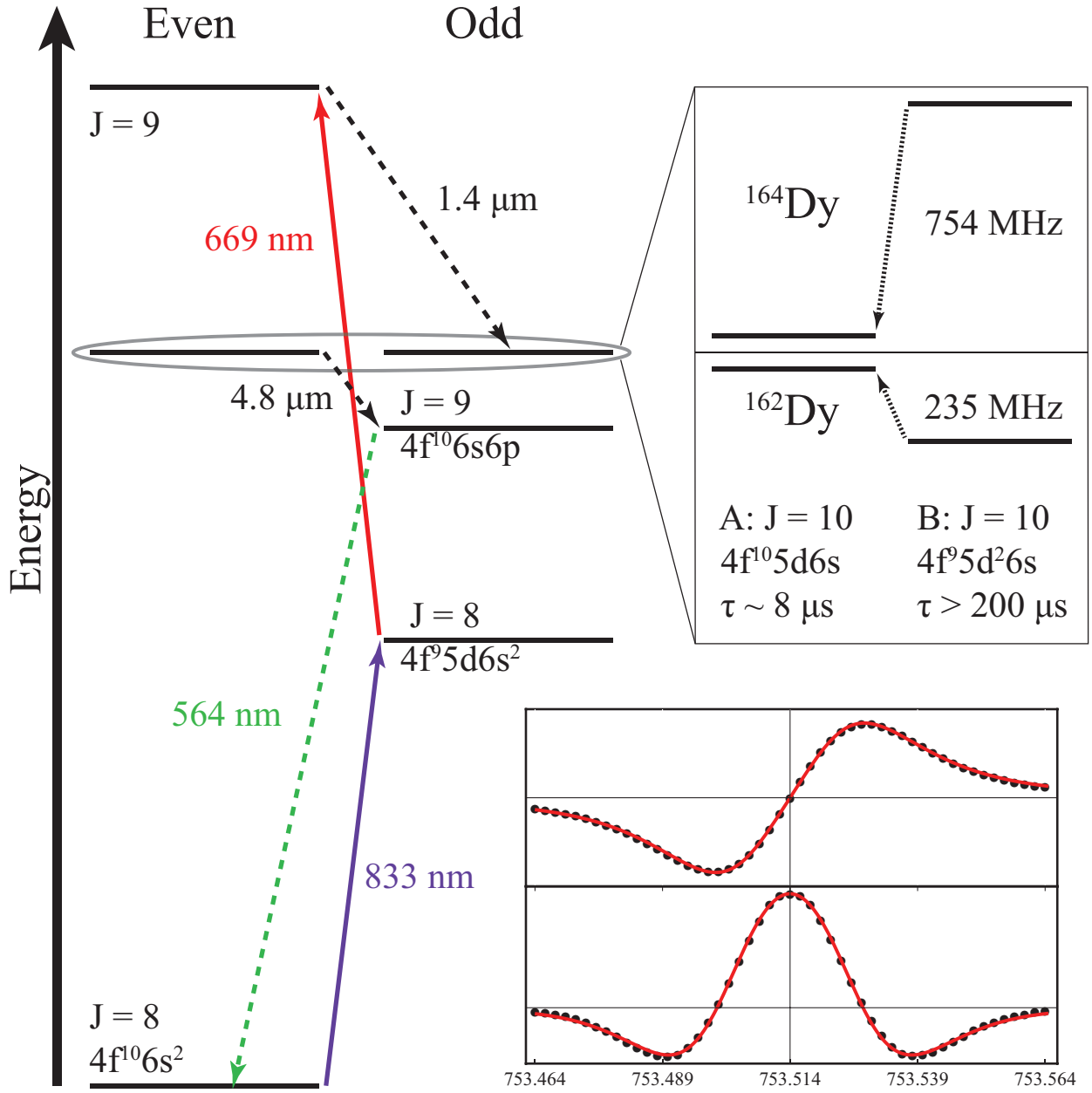

Figure 2.1: Partial energy diagram for Dy showing states of interest. Preparation of atoms is accomplished via two laser excitations and a spontaneous decay with 30% branching ratio into metastable state B. Atoms are excited from state B to A by a resonant, frequency-modulated rf electric field. State A decays with lifetime ~ 8 μs. A photomultipler tube and lock-in amplifier detect the 564-nm fluorescence. The bottom right inset shows typical lock-in signals for ^{164}Dy at the 1st and 2nd harmonics of the modulation frequency.

ratio	K_α	K_e	K_q	ref.
^{164,162}Dy/Cs	$(-2.6, +8.5) \times 10^6$	-1	-0.002	[this work]
Rb/Cs	-0.49	0	-0.021	[64]
Yb^+/Cs	-1.83	-1	-0.002	[65]
CSO/Cs	3	-1	0.1	[66]
Hg^+/Al^+	-2.95	0	0	[31]
Sr/Cs	-2.77	-1	-0.002	[67]
H(1S-2S)/Cs	-2.83	-1	-0.002	[69]

Table 2.1: Sensitivity coefficients for several clock comparisons. CSO refers to crystal-sapphire oscillator. The large sensitivity of the Dy transition frequency to variation of α is a relative enhancement due to the near degeneracy of the electronic states involved in the transition. Column references are for experimental details. Calculations of sensitivity coefficients can be found in Refs. [51, 72].

In Dy we make use of an 'accidental' degeneracy of energy levels to greatly relax the measurement precision necessary to place competitive limits on variation of α. Large relativistic corrections to electron energies in Dy create an almost complete degeneracy of opposite-parity excited states, labeled A and B by convention (Fig. 2.1). This system has been the subject of investigations spanning over two decades, including an attempt to measure parity nonconservation [41, 73]. Recently an analysis of the data from the present work has also been used to place stringent limits on violations of Lorentz symmetry and the Einstein Equivalence Principle [74].

The energy difference corresponding, $\omega_{BA} = (\epsilon_B - \epsilon_A)/\hbar$, is sensitive only to variation of α. In practice, however, any measurement must have a standard 'ruler' for comparison. The frequencies in our experiment are measured with respect to the stabilized oscillator of a cesium (Cs) beam standard, which introduces sensitivity to variation of both μ_e and μ_q. Changes in the frequency ratio $\omega_{BA}/\omega_{\rm Cs}$ can be written

$$\Delta \ln \frac{\omega_{BA}}{\omega_{\rm Cs}} = K_\alpha \frac{\Delta\alpha}{\alpha} + K_{\mu_e} \frac{\Delta\mu_e}{\mu_e} + K_{\mu_q} \frac{\Delta\mu_q}{\mu_q}. \tag{2.3}$$

As shown in Table 2.1, the Dy/Cs frequency comparison is over six orders of magnitude more sensitive to variation of α than to variation of μ_e and μ_q. This is a *relative* enhancement of sensitivity, rather than an absolute enhancement, owing to the near degeneracy of levels A and B . At our present level of measurement precision, variation of μ_e or μ_q would only be observable at levels orders of magnitude larger than stringent constraints placed by other experiments [64]. Thus our experiment is effectively sensitive only to variation of α,

$$\Delta \ln \frac{\omega_{BA}}{\omega_{\rm Cs}} = \frac{\Delta\omega_{BA}}{\omega_{BA}} - \frac{\Delta\omega_{\rm Cs}}{\omega_{\rm Cs}} \approx K_\alpha \frac{\Delta\alpha}{\alpha}. \tag{2.4}$$

Instability of the Cs reference, a > 30 yr old HP5061A, presents another source of concern for measurements spanning several years. A separate comparison between the Cs reference and a GPS stabilized Rb oscillator (Symmetricom TS2700) is performed during all data collection as a check against this. The fractional instability of the Cs reference, as compared to Rb reference, has been measured to be $< 10^{-12}$ yr^{-1}, well below our dominant measurement errors. The influence of Cs-reference instability is ignored, and the magnitude of the frequency $|\omega_{BA}|$ is assumed to vary with α according to [51]

$$\frac{\Delta|\nu_{BA}|}{2\pi} \approx \pm(2 \times 10^{15}\,\mathrm{Hz})\,\Delta\alpha/\alpha, \tag{2.5}$$

where the sign is negative for $\omega_{BA} > 0$ and positive for $\omega_{BA} < 0$. The present work is based on measurements of the $\omega_{BA}/(2\pi) \approx 753.5$ MHz and $\omega_{BA}/(2\pi) \approx -234.7$ MHz transitions in ^{164}Dy and ^{162}Dy (see Fig. 2.1). Comparing isotopes with sensitivities of opposite sign allows for the cancellation of common systematic errors that might otherwise mimic variation of α in a single isotope.

The spectroscopy is performed on a thermal beam of Dy atoms, produced in an oven heated to $\sim$ 1400 K inside a vacuum chamber with residual gas pressure of $\sim 10^{-7}$ torr. After two collimators/conductance chokes the atoms enter the interaction chamber where the residual gas pressure is $\sim 10^{-9}$ torr. The atoms undergo laser excitations at 833 nm and 669 nm, employing an adiabatic-passage technique [62], followed by a spontaneous decay at 1.4 μm with 30% branching ratio to state B. Narrow-band lasers provide high-fidelity isotope selection. Upon excitation to state B atoms then enter the interaction region, where excitation from B to A occurs via a frequency-modulated electric field. Atoms spontaneously decay from state A via two steps to the ground state. Fluorescen at 564 nm is directed by a polished-aluminum light-collection system ($\sim$ 4% overall efficiency) into a glass pipe, detected by a photomultiplier tube (PMT), and sent to a lock-in amplifier for processing. Figure 2.2 shows a simplified diagram of the experiment.

The apparatus has been designed to minize the systematic uncertainties presented in Table 2.2. In our previous result [56] the sensitivity was limited by the collisional pertubation of energy levels by background gases [75], poor suppression of Zeeman shifts owing to imperfections in laser-light polarization, and systematic shifts related to inhomogeneity of the rf field. In the new apparatus the high-vacuum system reduces collisional shifts to below the 1 mHz level. The electric-field region has been designed to ensure field homogeneity across the range of operating frequencies. Doppler shifts are suppressed by creating an rf-standing wave in the interaction region in addition to orienting the k-vector of any residual traveling wave perpendicular to the atomic-beam propagation axis. Two layers of magnetic shielding limit background magnetic fields to below 500 μG in all directions and three-axis magnetic field coils allow residual fields to be canceled out.

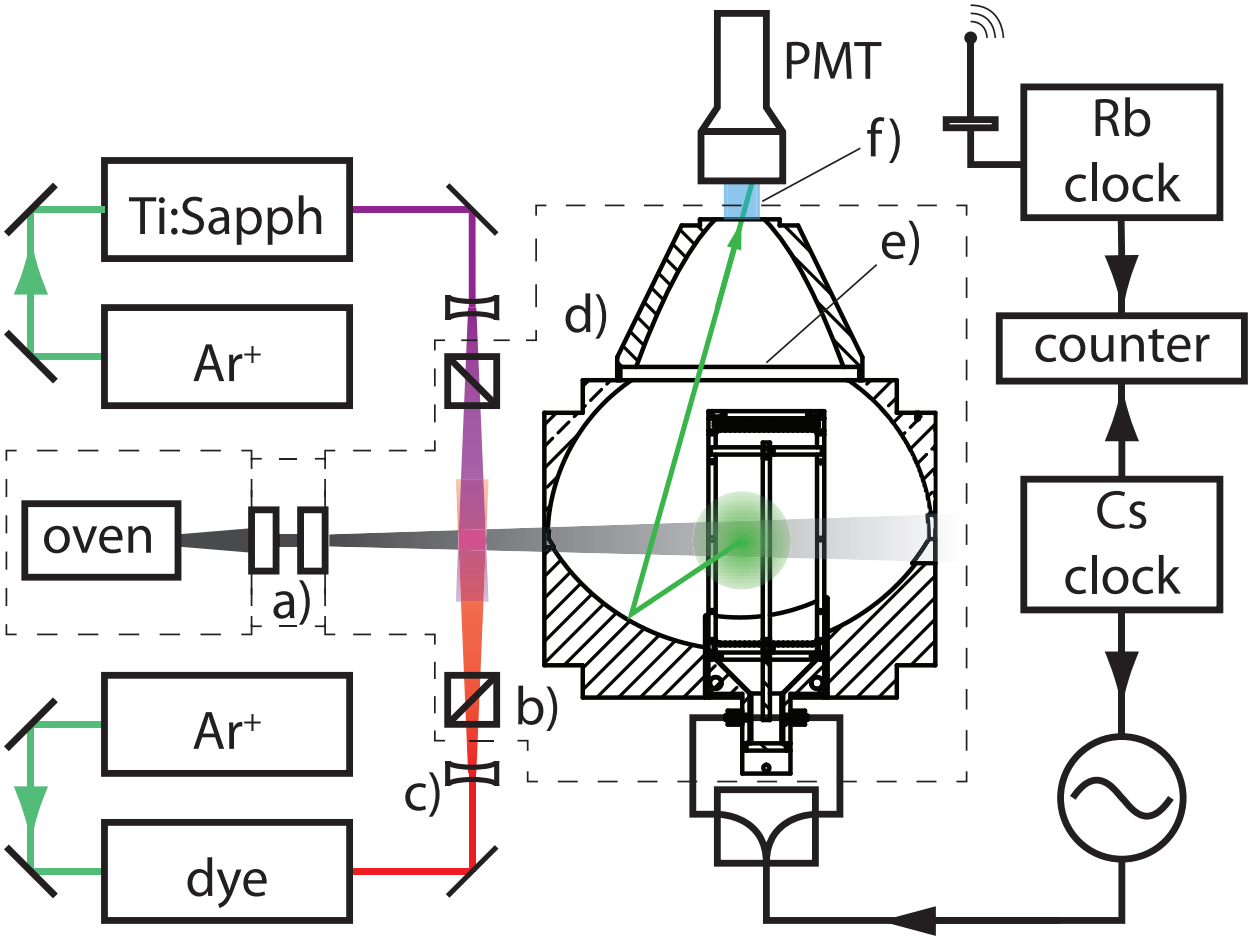

Figure 2.2: Schematic of the experimental set-up. Argon-ion lasers pump a dye laser producing 669-nm light and a Ti:sapphire laser producing 833-nm light. Components in vacuum are within the dashed boundaries. a) Skimmers collimate the atomic beam, and double as conductance chokes for differential pumping between the oven chamber and interaction chamber. b) In-vacuum linear polarizers are the last optical element for the laser light before interacting with Dy atoms. c) Lenses diverge the laser light to match the atomic beam divergence. d) Polished aluminum mirrors guide fluorescence to a photomultiplier tube. e) An interference filter wih 564-nm peak transmission suppresses stray laser and oven light. f) A glass pipe guides fluorescent light to a PMT for detection.

systematic	stability (mHz)	$\lvert\dot{\alpha}/\alpha\rvert$ $(10^{-17}\,yr^{-1})$
electronic offsets	200-470	10-23.5
BBR/temperature	66	3.3
Zeeman shift	50	2.5
ac-Stark shift	32	1.6
residual amplitude modulation	20	0.5
dc-Stark shift	< 1	< 0.04
collisional shift	< 1	< 0.04
quadrupole shift	< 1	< 0.04
clock stability	< 1	< 0.04
Total	**220 - 480**	**11 - 24**

Table 2.2: Current levels of known systematics. The total systematic uncertainty is obtained by adding in quadrature. The corresponding uncertainties for $\lvert\dot{\alpha}/\alpha\rvert$ assume two measurements separated by one year.

The dominant systematic is an electronic offset in the acquisition electronics, which may create a shift in the zero-crossing of the first-harmonic signal and apparent shift of the transition frequency. Sensitivity to electronic offsets is amplified by the relatively large transit-broadened linewidth of the transition, $\gamma \sim 2\pi \times 40\,\mathrm{kHz}$. We attempted to measure these offsets by varying the PMT gain, in order to change the useful signal size while leaving electronic noise unchanged. This idea is based on the offset compensation scheme presented in Ref. [76], but currently only constrains electronic offsets at the level of 500 nV. The importance of this effect depends on the absolute signal size and is reflected in the range of uncertainties in Table 2.2.

The ac-Stark shift in a two-level system is approximately zero for a resonant electric field, with a negligible contribution expected from what is known as the Bloch-Siegert shift [55]. Strongly coupled off-resonant levels may lead to large shifts correlated with rf-power. A measurement of the off-resonant contributions to the dynamic polarizabilities in ^{164}Dy and ^{162}Dy found $\delta\nu \simeq 70\,E^2$ mHz, where E^2 is mean-squared field value. Typical values of E^2 are 4.5 $(\mathrm{V/cm})^2$, corresponding to a stability of 3 mHz/% change in rf power. The uncertainty associated with this systematic is conservatively estimated from an assumption of 10% control over the rf power in the interaction region.

Additional Stark related systematics are the dc-Stark effect and blackbody radiation (BBR) induced Stark shifts [77]. Charged particles in the atomic beam can cause charge accumulation on the electric field plates and produce DC fields. A pair of sweep electrodes biased at 500 V is used to sweep charged particles out of the atomic beam, and the DC field is periodically measured via Zeeman-crossing spectroscopy [41, 54]. These are consistently found to be at the level of 10 mV/cm. The temperature dependence of the transition frequen-

cies has been measured near room temperature to be +29(4) mHz/K and −34(4) mHz/K for ^{164}Dy and ^{162}Dy, respectively. The isotopic dependence of the sign is consistent with BBR induced Stark shifts, but the attribution of these shifts to BBR is preliminary [78]. Currently, the 2 K temperature stability of the interaction region is used to estimate the systematic uncertainty due to this effect.

Suppression of Zeeman-effect related systematics is accomplished by performing spectroscopy with the Zeeman structure unresolved. Linear polarizers are located in vacuum and are the last optical elements for the 833-nm and 669-nm laser light, ensuring symmetric population of the $\pm M$ magnetic sublevels of state B. A magnetic field then leads to a broadening of the unresolved line, but no shift. A measured residual Zeeman shift of ~ 2.5 Hz/mG represents a suppression of ~ 1000 from the sensitivity of the $m = 10$ sublevel. The magnetic field stability along the quantization axis, chosen to coincide with the rf field, is at the level of $20\,\mu$G. We note that the magnetic field insensitive $m_B = 0 \to m_A = 0$ transition is forbidden between levels A and B where $\Delta J = 0$.

Residual amplitude modulation refers to a power imbalance of the carrier sidebands in the frequency-modulated spectrum of the electric field. Such an imbalance distorts the atomic lineshape and creates an apparent frequency shift. Poor impedance matching and termination of the rf transmission line made this a dominant systematic in early data at the 1 Hz level. Measuring the transition frequency with the in-phase and quadrature channels of the lock-in amplifier allows the size and stability of RAM to be measured directly with the atoms as discussed in Sec. 4.1. This protocol was implemented beginning May 2011. In August 2011 custom narrow-band, radio-frequency circulators (DPV CO) were installed to suppress transmission-line etalons. A frequency shift, introduced by switching between these configurations, was measured and a correction applied to earlier data.

The transition frequencies ν_{164} and ν_{162} measured over the span of two years are shown in Fig. 2.3. The reduced uncertainties beginning in May 2011 are primarily due to the characterization and eventual suppression of RAM. To constrain a linear variation of α in time a global linear least-squares fit is performed, in which the two isotopes' data are fit by independent offsets and equal magnitude slopes of opposite sign. The best-fit slope of -0.12 ± 0.14 Hz/yr corresponds to the result

$$\dot{\alpha} = (-5.8 \pm 6.9) \times 10^{-17}\,\mathrm{yr}^{-1}, \tag{2.6}$$

which is consistent with zero within 1 standard deviation. This result approaches within a factor of 3 the level obtained with the best optical clocks in the world [31], and is limited by systematic uncertainties. The contribution of statistical uncertainties is at the level of $\dot{\alpha}/\alpha \sim 1.7 \times 10^{-17}$ yr^{-1}. The data are also fit by equal slopes of the same sign, which is sensitive to common mode systematics, but not variation of α. This fit gives a slope of (0.41 ± 0.14) Hz/yr. The 3-sigma, non-zero drift at the level of ~ 0.5 Hz could be explained by a drifting electronic offset, which as a technical systematic is expected to be the same sign for both isotopes.

Our data can also be used to constrain violations of local position invariance, assuming a model where fundamental constants are influenced by light scalar fields that scale linearly with changes in the local gravitational potential [79]. We can express this as $\Delta\alpha/\alpha = k_\alpha \Delta U/c^2$, where $\Delta U/c^2$ is a change in the dimensionless gravitational potential. The ellipticity of the Earth's orbit provides semi-annual changes in the laboratory gravitational potential, $\Delta U/c^2 = \pm 1.65 \times 10^{-10}$, at the aphelion and perihelion of Earth's orbit for plus and minus, respectively. To constrain k_α the data are again fit by global linear least-squares to cosine functions with equal amplitudes but 180° phase difference. The period is equal to one solar year and zero phase is fixed at Earth's perihelion on Jan. 3, 2010. The best-fit amplitude of oscillation is found to be 0.18 ± 0.17 Hz, providing the best bound to date on the dimensionless coupling to be

$$k_\alpha = (-5.5 \pm 5.2) \times 10^{-7}, \tag{2.7}$$

providing the best constraint so far on this parameter [64]. The sensitivity is again limited by systematics. The statistical contribution to the uncertainty is at the level of $k_\alpha \sim 1.2 \times 10^{-7}$. A global fit to the two isotopes' data with 0° phase difference, sensitive to common mode systematics, has an amplitude of -0.17 ± 0.17 Hz. The data and best fits are shown in Figure 2.3

We have presented updated constraints on variation of α that represent almost two orders of magnitude improvement over previous results, with the present level of sensitivity still limited by systematic effects. While more stringent control of these systematics, particularly electronic offsets, presents a clear avenue to achieving the ultimate practical statistical limit of 10^{-18} calculated in [55], recent astrophysical evidence [27] for spatial variation of α suggests an observable variation of α in the laboratory at the level of 10^{-19} [28]. A new generation of experiments based on the spectroscopy of optical nuclear transitions [80] or optical transitions in highly-charged ions [81] will be necessary to observe this effect.

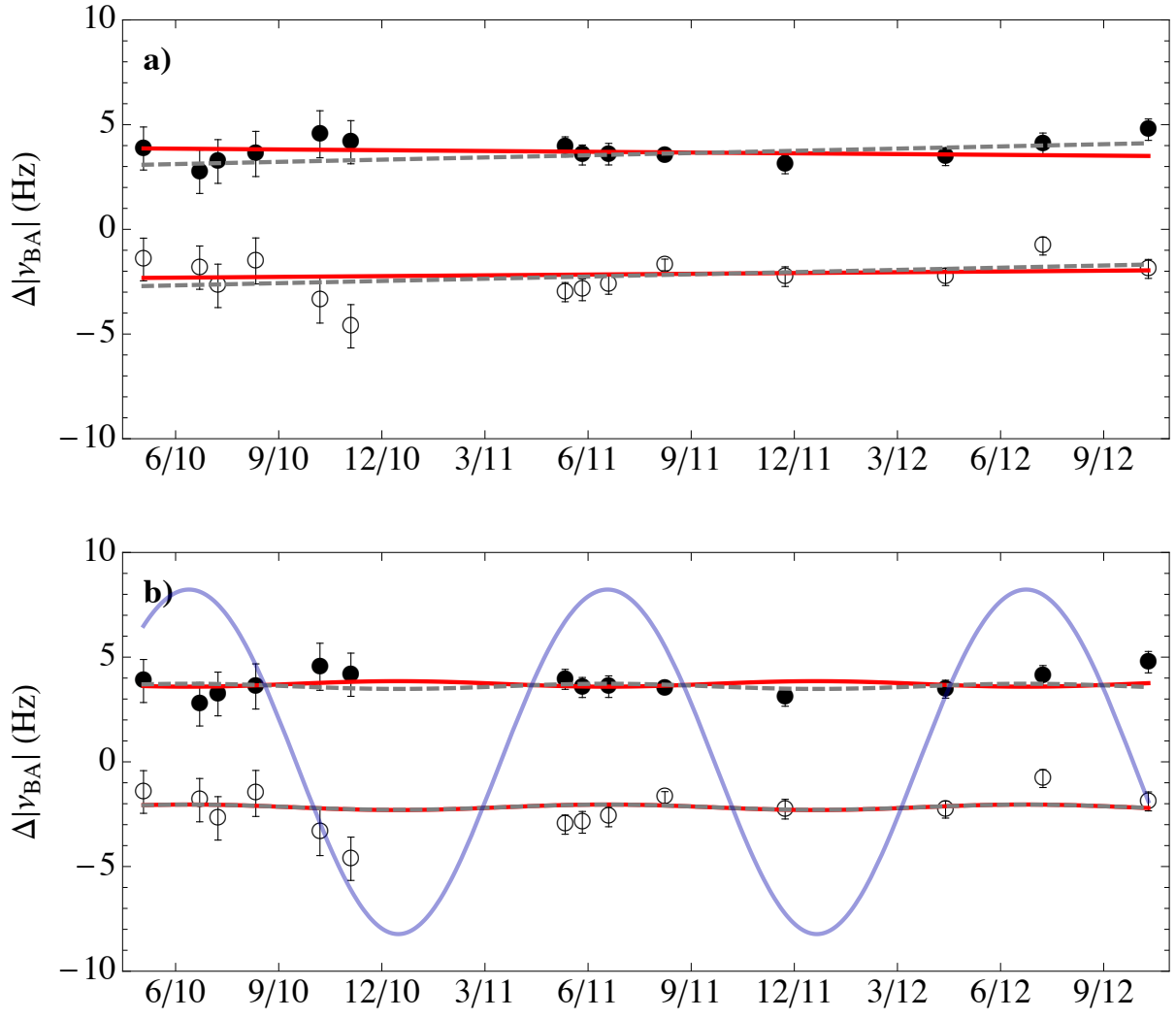

Figure 2.3: Changes in the transition frequencies for ^{162}Dy (filled circles) and ^{164}Dy (empty circles) over the span of two years. The frequencies for ^{162}Dy and ^{164}Dy are displayed with respect to 234,661,102 Hz and 753,513,708 Hz, respectively. a) The data are fit by linear functions with equal magnitude slopes of opposite sign (solid) and same sign (dashed). b) The data are fit by cosine functions with equal amplitudes but 180° phase difference (solid) and 0° phase difference (dashed). The variation of the dimensionless gravitational potential, scaled in relative units by 5×10^{10}, is shown by the light solid line.

3 — Test of Lorentz symmetry

3.1 Limits on violations of Lorentz symmetry and the Einstein equivalence principle using radio-frequency spectroscopy of atomic dysprosium

We report a joint test of local Lorentz invariance and the Einstein Equivalence Principle for electrons, using long-term measurements of the transition frequency between two nearly degenerate states of atomic dysprosium. We present many-body calculations which demonstrate that the energy splitting of these states is particularly sensitive to violations of both special and general relativity. We limit Lorentz violation for electrons at the level of 10^{-17}, matching or improving the best laboratory and astrophysical limits by up to a factor of 10, and gravitational redshift anomalies for electrons to the level of 10^{-8}. With some enhancements, our experiment may be sensitive to Lorentz violation at the level of 9×10^{-20}.

This chapter is currently under review for publication in Physical Review Letters. The preprint is available at `http://arxiv.org/abs/1303.2747`

Local Lorentz invariance (LLI) and the Einstein equivalence principle (EEP) are fundamental to both the standard model and general relativity [82]. Nevertheless, these symmetries may be violated at experimentally accessible energy scales due to spontaneous symmetry breaking, or some other mechanism of an as yet unknown unified theory of physics at the Planck energy scale [34, 83]. This has motivated the development of many experimental tests of both LLI and EEP [84, 85], and of a phenomenological framework, known as the standard model extension (SME), within which the results of these tests can be quantitatively compared with one another [32]. This widely used [36] framework augments the standard model Lagrangian with every possible combination of standard model fields that are not term-by-term invariant under Lorentz transformations, while preserving the overall Lorentz invariance of the total action, and maintaining gauge invariance and energy-momentum conservation [32]. Violations of LLI, which themselves constitute violations of EEP [82, 85], have also been shown to violate other tenets of general relativity, such as the universality of free fall, and local position invariance [86].

In this letter, we show, using many-body calculations, that the energies of the nearly degenerate $4f^{10}5d6s$ and $4f^{9}5d^{2}6s$ states of dysprosium (Dy) [18, 87–89] are extremely sensitive to physics that breaks LLI and the EEP in the dynamics of electrons. We report the results of an analysis of a modest amount of Dy spectroscopy data acquired over two years that significantly improves upon the best laboratory [11], accelerator [90], and even some astrophysical [37] limits on a specific class of LLI and EEP violating physics for electrons. We show that Dy spectroscopy also offers substantial promise as a gravitational redshift test [91], constraining electron-related gravitational redshift anomalies at the level of 10^{-8} [52].

The EEP and LLI require that spacetime, while it may be curved, is locally flat, and Lorentzian [82]. This means that the relative frequencies of any set of clocks at relative rest and located at the same point in (or within a sufficiently small, approximately flat volume of) spacetime be independent of a) where that point is located in a gravitational potential (also known as local position invariance), or b) the velocity of their rest frame relative to any other reference frame (LLI). In the SME, violation of EEP and LLI for electrons can be described as a modification of the electrons' dispersion relation, which in turn leads to variations in the energies of bound electronic states as a function of velocity and position in an external gravitational potential [35, 86].

We focus on the symmetric, traceless $c_{\mu\nu}$ tensor in the electron sector of the SME, and work in a coordinate system scaled such that the speed of light is a constant c in all frames. In the SME, the $c_{\mu\nu}$ tensor modifies the kinetic term in the electronic QED Lagrangian to become [33]

$$\mathcal{L} = \tfrac{1}{2} i\bar{\psi}\left(\gamma_\nu + c_{\mu\nu}\gamma^\mu\right) \overleftrightarrow{D^\nu}\, \psi - \bar{\psi} m \psi, \tag{3.1}$$

where m is the electron mass, ψ is a four-component Dirac spinor, γ^ν are the Dirac gamma matrixes, and $f\overleftrightarrow{D^\nu}g \equiv fD^\nu g - (D^\nu f)g$, with $D^\nu \equiv \partial^\nu - qA^\nu$. The $c_{\mu\nu}$ tensor is frame-dependent [33, 35, 92, 93], and is uniquely specified by its value in a standard reference frame. We use the Sun-centered, celestial equatorial frame (SCCEF) for this purpose, indicated by

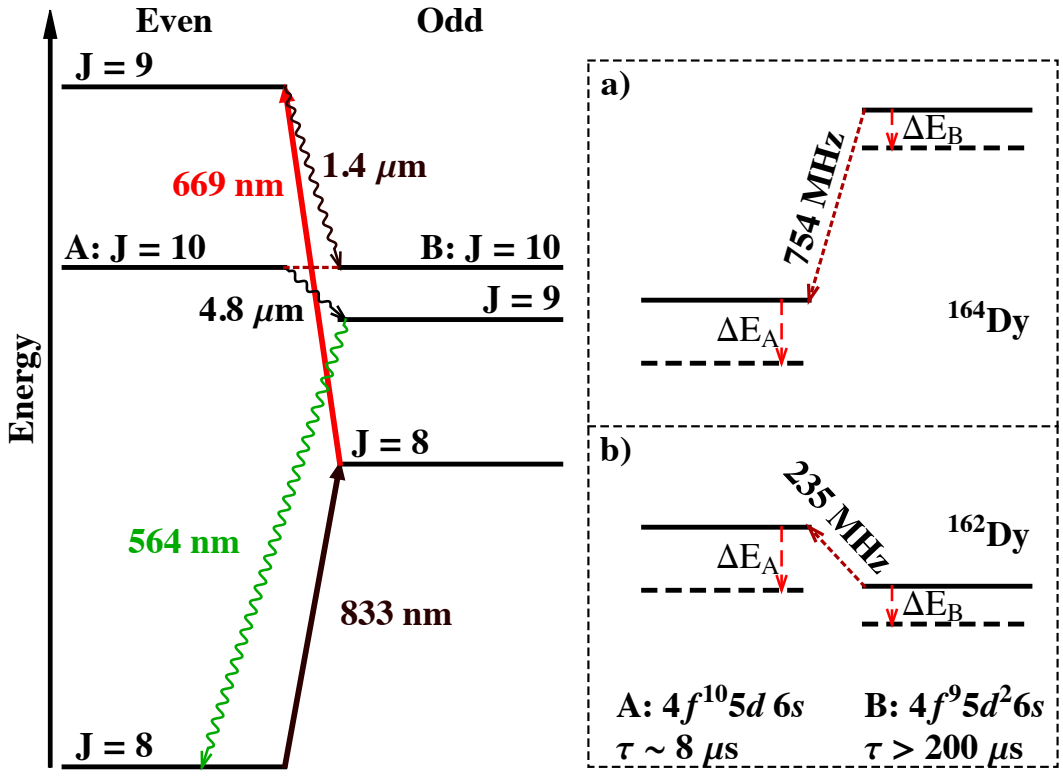

Figure 3.1: Energy levels of Dysprosium. Atoms are optically pumped (solid lines) to a state which decays (wavy lines) into the metastable state B. A linearly polarized rf field drives the $B \to A$ transition, which is detected via fluorescence at 564nm. Insets a) and b) show the magnified diagram for ^{164}Dy and ^{162}Dy, respectively. Lorentz-symmetry violation shifts the rf resonance by $\delta\omega_{\rm rf} = (\Delta E_B - \Delta E_A)/\hbar$. Measured frequencies are always positive, so the sign of the observed shift is determined by the sign of the level splitting.

the coordinate indexes (T, X, Y, Z), for ease of comparison with other results [36]. The component indexes for laboratory frame coordinates are given as $(0, 1, 2, 3)$, where $t = x_0/c$ is the time coordinate. Roman indexes are used to indicate the spatial components of $c_{\mu\nu}$, and are capitalized to indicate the SCCEF frame. The $c_{\mu\nu}$ tensor has six parity-even components: c_{TT}, plus the five c_{JK}'s; and three parity-odd components: c_{TJ}, which introduce direction and frame dependent anisotropies in the electrons' energy-momentum, or dispersion relation [33]. This shifts the energies of bound electronic states as a function of the states' orientation and alignment in absolute space, breaking both LLI and rotational symmetry [35].

In general relativity, global Lorentz invariance is broken by the curvature of space-time. In terms of the global coordinate system, this curvature influences the motion of freely falling particles by modifying their dispersion relations. General relativity preserves local Lorentz invariance because gravity modifies all particles' dispersion relation in the same way –at any

point in space time, it is always possible to define coordinates such that gravity's modifications to particles' dispersion relations drop out. The additional effect of the $c_{\mu\nu}$ coefficients, however, makes it impossible to completely remove gravity from the local equations of motion, leading to locally observable gravitational-potential dependent shifts in the energies of bound electronic states, or anomalous gravitational redshift phenomena [52, 86]. This energy shift is proportional to the electron's kinetic energy [35].

Dysprosium, an atom with 66 protons and a partially filled f-shell, is well suited to measuring the electron $c_{\mu\nu}$ coefficients. It possesses two near-degenerate, low-lying excited states with significant quadrupole moments, and opposite parity: $4f^{10}5d6s\,J=10$ (state A) and $4f^{9}5d^{2}6s\,J=10$ (state B), which differ by a transposition of an electron from the $4f$ to the $5d$ orbital. The energy difference between these states can be measured directly by driving an electric-dipole transition (Fig. 3.1) with a radio-frequency (rf) field, and should be particularly sensitive to anomalies proportional to the electrons' kinetic energy, since the $4f$ orbital lies partly within the radius of filled s, p, and d shells that screen the nuclear charge from the larger $5d$ orbital. The same properties of Dy that make measurements of the $B \to A$ transition particularly sensitive to variations in the fine structure constant, α [55, 56, 94], also make them highly sensitive to violations of LLI and EEP.

In terms of spherical-tensor operators, Eq. (3.1) produces a shift δh in the effective Hamiltonian for a bound electron with momentum $\vec{p}$ given by [35, 40, 86]

$$\delta h = -\left(C_0^{(0)} - \frac{2U}{3c^2}c_{00}\right)\frac{\mathbf{p}^2}{2m} - \sum_{q=-2}^{2}\frac{(-1)^q}{6m}C_q^{(2)}T_{-q}^{(2)}, \tag{3.2}$$

where we have included the leading order $(2U/3c^2)c_{00}$ gravitational redshift anomaly [86], and

$$\begin{aligned} C_0^{(0)} &= c_{00} + \tfrac{2}{3}c_{jj}, & C_0^{(2)} &= (c_{jj} - 3c_{33}) \\ C_{\pm1}^{(2)} &= \pm 3(c_{31} \pm ic_{32}), & C_{\pm2}^{(2)} &= 3(c_{11} - c_{22} \pm ic_{12}), \end{aligned}$$

are written in terms of the laboratory-frame values of the $c_{\mu\nu}$ tensor, with summation implied over like indexes. Note that $C_0^{(2)}$ is also known as c_q in the literature [35]. The spherical tensor components of the squared momentum are written as $T_0^{(2)} = \vec{p}^{\,2} - 3p_3^2$, $T_{\pm1}^{(2)} = \pm p_3(p_1 \pm ip_2)$, and $T_{\pm2}^{(2)} = (p_1^2 - p_2^2)/2 \pm ip_1p_2$. The energy shift for a state $|J, M\rangle$ of an atom due to the perturbation (3.2) is the expectation value of the corresponding N electron operator. Since only tensors with $q = 0$ contribute to energy shifts of bound states, we need only calculate matrix elements for the $\vec{p}^{\,2}$ and $T_0^{(2)} = \vec{p}^{\,2} - 3p_3^2$ operators.

To calculate these matrix elements, we use a version of the configuration interaction method optimized for atoms with many electrons in open shells. This method has been used to calculate energy levels, transition amplitudes, dynamic polarizabilities, "magic" frequencies in optical traps, and the effects of α variation and parity violation in Dy and other atoms [30, 51]. Calculated values of the reduced matrix elements for the A and B states of Dy

	States	
	A	B
leading config.	$4f^{10}5d6s$	$4f^{9}5d^{2}6s$
Term	$^{3}[10]$	$^{7}\mathrm{H}^{o}$
J	10	10
	Energies (cm^{-1})	
Expt. [50]	19798	19798
Calc. [73]	19786	19770
	Matrix Element (atomic units)	
$\langle J \parallel c\gamma^{0}(\gamma^{j}p_{j} - 3\gamma^{3}p_{3}) \parallel J\rangle$	69.48	49.73
$\langle J \parallel \mathbf{p}^{2} - 3p_{3}^{2} \parallel J\rangle$	69.84	49.89
$\langle JM\|\mathbf{p}^{2}\|JM\rangle$	437	422

Table 3.1: Matrix elements of the relevant operators of Lorentz violation for states A and B of ^{163}Dy in units of the Hartree energy $E_h = (6.5 \times 10^{15}\ \mathrm{Hz})h$.

are presented in Table 3.1. To check our results, we repeat the matrix element calculation using the fully relativistic form of the Hamiltonian [40]. The corresponding operators are $c\gamma^{0}\gamma^{j}p_{j}$ and $T_{0}^{(2)} = c\gamma^{0}(\gamma^{j}p_{j} - 3\gamma^{3}p_{3})$, respectively. We find good agreement between both calculations, consistent with our initial approximation.

All frequency measurements are made with reference to a standard Cs reference oscillator. If LLI is violated, it is possible that the electron $c_{\mu\nu}$ coefficients may also affect the frequency of our reference. The symmetries of the $6s^{1}$ state and the clock transition largely suppress quadrupole shifts in the hyperfine frequency of the Cs reference, and the fractional shift of the reference due to the anomalous redshift contributed by the $c_{\mu\nu}$ terms is expected to be $\approx -\frac{4}{3}c_{TT}$ [52]. For our purposes, however, violations of LLI and anomalous redshifts of the Cs hyperfine reference frequency can be neglected. The quadrupole term is strongly suppressed due to the symmetries of the $6s^{1}$ state [35], and the scalar shift is expected to be $\sim (10\ \mathrm{GHz})c_{\mu\nu}$ [52], while as Table 3.1 shows, the splitting between the A and B states of Dy will be $\sim (100\ \mathrm{THz})c_{\mu\nu}$ or greater.

Dysprosium metal is heated in an oven to ~ 1400 K to produce an effusive atomic beam. The Dy atoms are optically pumped into the metastable state B via two consecutive laser excitations with 833 nm and 669 nm light followed by a spontaneous decay. The atoms are resonantly excited from state B to A via an rf electric field, whose linear polarization defines the atoms' quantization axis. The polarization of the excitation laser is chosen to create a symmetric population among the $\pm M$ magnetic sublevels of state B along this quantization axis. The A state relaxes to the ground state in a cascade decay, emitting 564 nm light in the process. The transition frequency is determined by measuring the intensity of the 564 nm fluorescence (with a photomultiplier) as a function of radio frequency. A more detailed

description of the experimental procedure and apparatus can be found in Refs. [56, 58].

We measure the average frequency shift of all populated magnetic sublevels, driven by a linearly polarized rf electric field. Each state's energy shift varies with the projection of its total angular momentum according to:

$$\delta E = -\frac{1}{2}\left(C_0^{(0)} - \frac{2U}{3c^2}c_{00}\right)\langle JM|\mathbf{p}^2|JM\rangle - \frac{1}{6}C_0^{(2)}\frac{\langle J\,M\,2\,0|J\,M\rangle}{\sqrt{2J+1}}\langle J \parallel T_0^{(2)} \parallel J\rangle, \qquad (3.3)$$

where J is the atom's total angular momentum and $\langle J\,M\,2\,0|J\,M\rangle$ is a Clebsch-Gordan coefficient. The actual population distribution among the magnetic sublevels is measured by resolving the Zeeman structure of the two states and measuring the peak amplitude of each transition. These amplitudes are used as weights in an average over the shift for each $|JM\rangle$ state in Eq. (3.3) to determine the average shift of the unresolved line. Using the rf-field polarization to define the quantization axis, the average shift in the $B \to A$ transition frequency $\omega_{\rm rf}$ for ^{162}Dy and ^{164}Dy is given by

$$\frac{\delta\omega_{\rm rf}}{2\pi} = \mp\big(10^{14}\,\text{Hz}\big)\left[500\left(C_0^{(0)} - \frac{2U_\odot}{3c^2}c_{00}\right) + 9.1C_0^{(2)}\right], \qquad (3.4)$$

where $\omega_{\rm rf}$ is defined to be positive, producing a negative (positive) shift for ^{162}Dy (^{164}Dy), and $U_\odot = -M_\odot G/r_{\rm lab}$ is the Sun's gravitational potential. The overall sign of the first term is determined by the sign of the splitting between state A and B, and that of the second term is by the populations of the magnetic-sublevels. This sign flip between the two isotopes aids in the rejection of common-mode systematic backgrounds.

The value of $C_0^{(0)}$ and $C_0^{(2)}$ in the laboratory-frame is a function of the value of $c_{\mu\nu}$ in the SCCEF, as well as the orientation and velocity of the lab, and so any anomalous $\delta\omega_{\rm rf}$ measured in the lab must vary in time [35]. The precise relation between $C_0^{(0)}$ and $C_0^{(2)}$ and the SCCEF value of $c_{\mu\nu}$ can be found in Sec. 3.2. In the laboratory frame, moving with the Earth's orbital velocity $c\beta_\oplus$ relative to the SCCEF, c_{TT} makes a small contribution to $C_0^{(2)}$, scaled by a factor of $\beta_\oplus^2 \approx 1\times10^{-8}$. Over the course of a year, the gravitational potential of the laboratory due to the Sun modulates sinusoidally with amplitude $\Delta U_\odot/c^2 = 1.7\times10^{-10}$, yielding a measurement of c_{TT} via the scalar component of Eq. (3.3).

Using repeated measurements of $\delta\omega_{\rm rf}$ taken over a span of nearly two years, we obtain constraints on eight of the nine elements of $c_{\mu\nu}$ in the SCCEF. The analysis is performed in two parts. The c_{JK} coefficients are constrained using data collected over the course of 12 hours beginning on Oct. 19, 2012. For each isotope the mean value of 20 successive frequency measurements (~ 10 seconds) is assigned an error bar according to the standard error of the mean for that bin. The resulting data are fit with Eq. (3.4), including an independent, constant frequency offset for each isotope, after a transformation to the SCCEF coordinate system has been made. The short duration of this data set allows us to neglect the slow (1 yr^{-1} and 2 yr^{-1}) variations induced by the c_{TT} and c_{TJ} terms. These terms are neglected in this fit, as they are suppressed by at least one factor of $\beta_\oplus \sim 10^{-4}$, and are already sufficiently bounded by astrophysics [37] that their effect on our measurements of c_{JK} is roughly 100 times less than our statistical sensitivity.

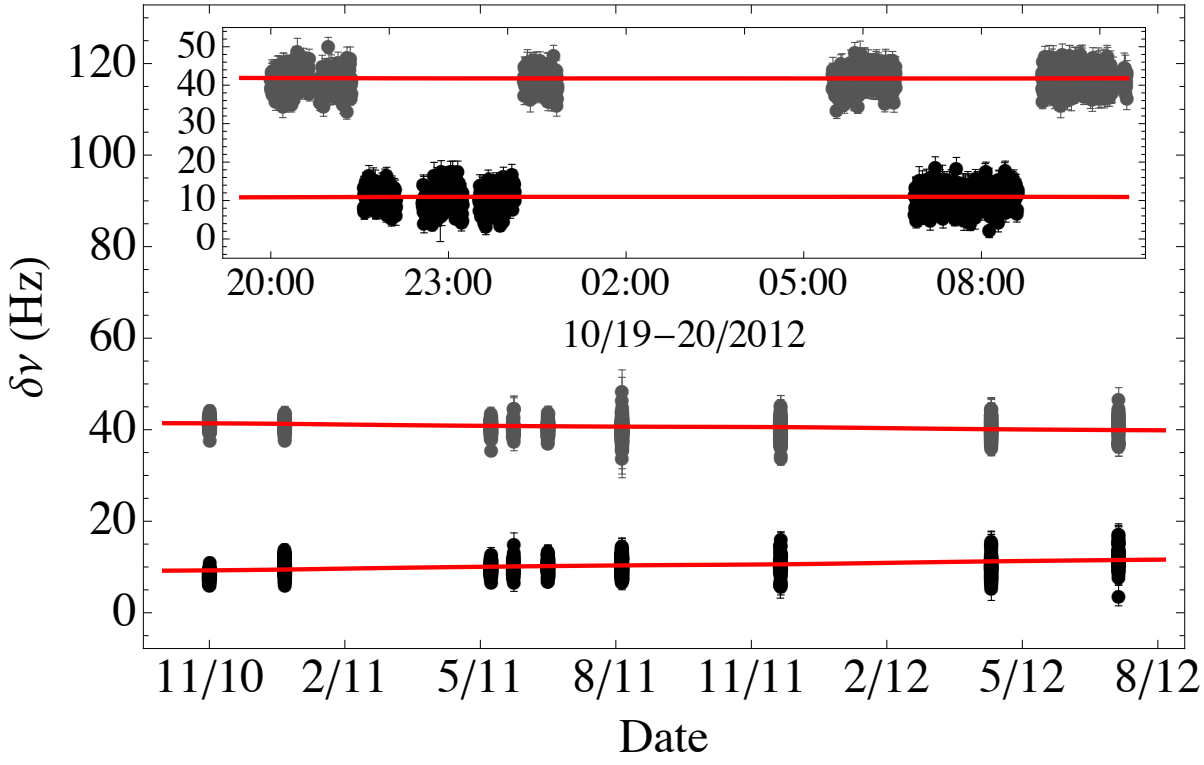

Figure 3.2: Full record of frequency measurements for ^{162}Dy (upper data set) and ^{164}Dy (lower data set). Frequencies are plotted relative to 234 661 065 Hz for ^{162}Dy and 753 513 695 Hz for ^{164}Dy. Error bars are obtained by binning measurements into sets of 20 and calculating the standard error of the mean for each set. The solid line indicates the least-squares fit. Inset, is an expanded view of the most recent measurements beginning on Oct. 19, 2012, with time given in Pacific Standard Time (Coordinated Universal Time minus 8 hours).

The c_{TJ} and c_{TT} coefficients are constrained using data collected between November 2010 and July 2012. The data are binned and assigned error bars as previously described. Since the above analysis of the 12 hour data set provides tight constraints on c_{JK} coefficients, the second fit includes only the c_{TJ} and c_{TT} coefficients. The fit routine is the same as before, adding an independent linear slope for each isotope to account for long-term systematic drifts. The resulting fit includes a large signal for the combination $c_{T(Y-Z)} \equiv c_{TY} \sin\eta - c_{TZ} \cos\eta = (-3.8 \pm .5) \times 10^{-12}$, where η is the Earth's axial tilt. As such a signal is inconsistent with existing limits on $c_{T(Y-Z)}$ [37, 90], we suspect the presence of uncontrolled systematic shifts in $\delta\omega_{\rm rf}$ with characteristic modulation frequencies near 1 day^{-1} and 2 day^{-1}, and amplitude 300 mHz. These systematics may be due in part to, *e.g.* , magnetic field fluctuations ($\sim$ 50 mHz), blackbody shifts due to changes in the temperature of the spectroscopy chamber ($\sim$ 60 mHz) [78], and changes in electronic offsets ($\sim$ 140 mHz). Daily fluctuations in these

Combination	Limits		
	new	existing	
$0.10\,c_{X-Y} - 0.99\,c_{XZ}$	-8.9 ± 11	-33 ± 19	$\times 10^{-17}$
$0.99\,c_{X-Y} + 0.10\,c_{XZ}$	3.8 ± 5.6	-8.6 ± 62	$\times 10^{-17}$
$0.94\,c_{XY} - 0.35\,c_{YZ}$	-0.4 ± 2.8	43 ± 19	$\times 10^{-17}$
$0.35\,c_{XY} + 0.94\,c_{YZ}$	3.2 ± 7.0	5.3 ± 23	$\times 10^{-17}$
$0.98\,c_{T(Y+Z)} - 0.18\,c_{TX}$	$-1.0 \pm 18(3.3)$	0.3 ± 1.8	$\times 10^{-15}$
$0.18\,c_{T(Y+Z)} + 0.98\,c_{TX}$	$5.6 \pm 7.7(2.4)$	-1.5 ± 5.4	$\times 10^{-15}$
$c_{T(Y-Z)}$	$-21 \pm 19(2)$	$.011 \pm .028$	$\times 10^{-13}$
c_{TT}	$-8.8 \pm 5.1(4.0)$	$10^{-6}(2 \pm 2)$	$\times 10^{-9}$
c_{TT} (gravitational)	$-14 \pm 28(9)$	4600 ± 4600	$\times 10^{-9}$

Table 3.2: Constraints on combinations of electron $c_{\mu\nu}$-coefficients from spectroscopy of the radio frequency transitions in ^{162}Dy and ^{164}Dy. We use the shorthand notation $c_{X-Y} \equiv c_{XX} - c_{YY}$, $c_{T(Y+Z)} \equiv c_{TY}\cos\eta + c_{TZ}\sin\eta$, and $c_{T(Y-Z)} \equiv c_{TY}\sin\eta - c_{TZ}\cos\eta$, where the angle $\eta = 23.4^\circ$ is the angle between the Earth's spin and orbital axes. Constraints above the horizontal divider are obtained from one day's worth of data, while those below the line are obtained from analysis of over two years of data, see text. Some error bars for the latter set of constraints are adjusted for systematic error. Statistical error bars are indicated in parenthesis where this occurs. Past bounds on c_{JK}, c_{TJ}, and c_{TT} are from analysis of non-gravitational experiments or observations [11], [37], and [90], respectively, while purely gravitational limits on c_{TT} are taken from [52].

systematic shifts have less effect on our bounds on c_{TX} and $c_{T(Y+Z)} \equiv c_{TY}\cos\eta + c_{TZ}\sin\eta$, as these are primarily sensitive to the yearly modulation signal produced by the larger scalar component of Eq. (3.4) (see Table 3.4). Nevertheless, the least squares error bars assume that systematic noise is uncorrelated, and overestimate the precision of our experiment in the presence of correlated noise. To estimate the size of the systematics we repeat the least-squares analysis using a modified Lorentz violating model that does not reverse sign for ^{162}Dy relative to ^{164}Dy. This model is insensitive to any real Lorentz violations, but is sensitive to common mode systematics errors. The mean values from this fit are used to estimate systematic uncertainties for each parameter, while the statistical errors are estimated from the original fit.

We have also analyzed our results as a test of the gravitational redshift for electrons in the Sun's gravitational potential by fitting the long term data to terms proportional to the gravitational potential, neglecting frame-dependent effects. We obtain a purely gravitational limit on the electron's c_{TT} coefficient of $-14 \pm 7 \times 10^{-9}$.

The data and fits are shown in Fig. 3.2. The fit results are displayed in Table 3.2 with uncertainties quoted for 68% confidence limits. The reduced chi-squared, $\bar{\chi}^2$, for the short and long time-scale fits are 1.2 and 1.8, respectively. The larger $\bar{\chi}^2$ for the long-term fits is likely due to uncontrolled systematics that have not been accounted for in our

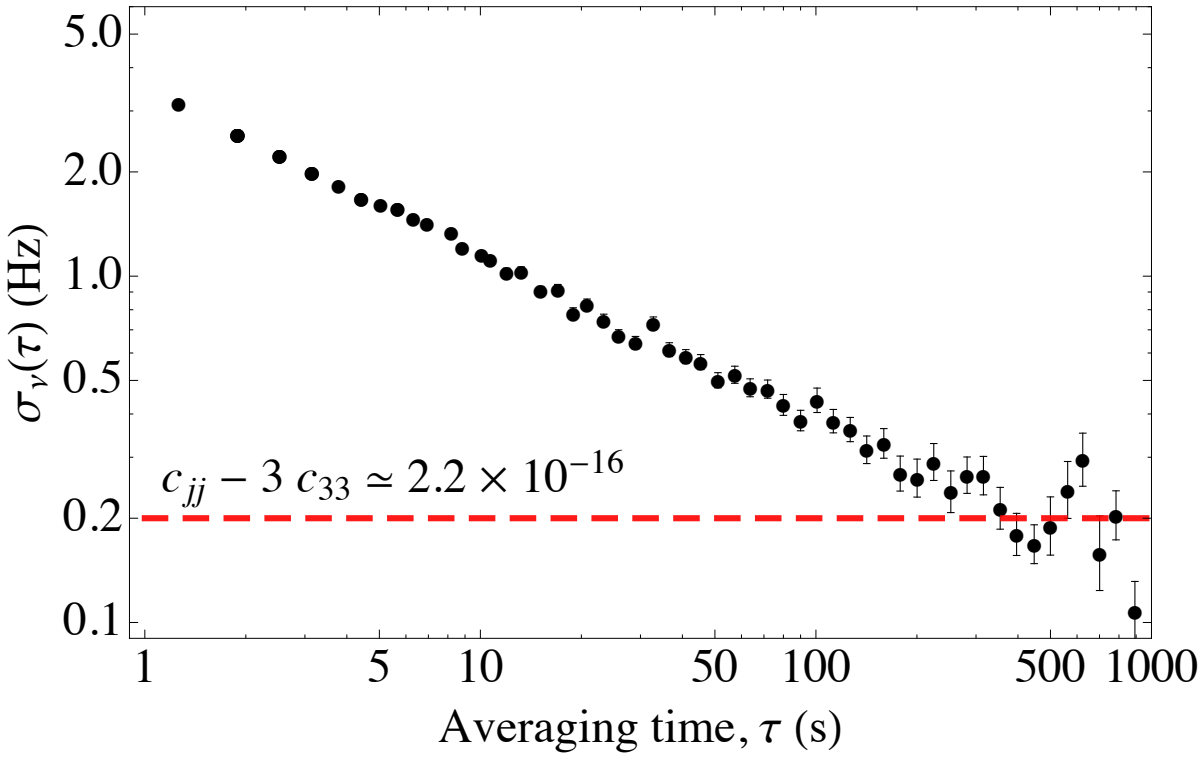

Figure 3.3: Allan deviation from a two hour measurement of the ^{164}Dy transition frequency (7:00 to 9:00 on the Fig. 3.2 inset).

purely statistical estimation of error bars. To provide conservative estimates on parameter uncertainties we have performed an overall scaling of the error bars in both fits to provide $\bar{\chi}^2 = 1$.

We have tightened the experimental limits on four of the six parity-even components of the $c_{\mu\nu}$ tensor by factors ranging from 2 to 10 [11, 36]. We also report limits on two combinations of the parity-odd c_{TJ} that are on par with the best astrophysical constraints [36, 37]. As a gravitational redshift test in the Solar potential, our experiment constrains electron-related anomalies in the gravitational redshift at the level of 10^{-8}.

With optimization, our experiment could yield significantly improved constraints. As shown in Fig. 3.3, our experiment is statistically sensitive to the laboratory-frame observable $C_0^{(2)} = c_{jj} - 3c_{33}$ at the level of 2.2×10^{-16} after only 400 seconds of averaging.

Despite this, our present experiment must wait a full day for the Earth to rotate the laboratory in the fixed reference frame, making it susceptible to systematics that vary over the course of a day. This could be addressed by active rotation of the entire apparatus, or by rotating the polarization of the rf electric field, making it possible to reach statistically limited sensitivities to $C_0^{(2)}$ at the level of 1.5×10^{-17} in one day, and 7.8×10^{-19} in one year.

Further improvement could be obtained by optically pumping the atoms to the $M = \pm 10$ sublevels, increasing the experiment's sensitivity to $C_0^{(2)}$ by a factor of ~ 4.5. Another factor of two could potentially be gained by increasing the interaction time of the atoms in the rf field, as the measured linewidth of 40 kHz is twice the natural 20 kHz linewidth of state A. An optimized experiment may thus reach sensitivities at the order of 8.7×10^{-20} using data collected over one year. This would be three orders of magnitude better than the presently reported limits on c_{JK}, two orders of magnitude better than the best sensitivities attainable by existing optical resonator tests [53, 95], and could prove more sensitive than astrophysical tests [37, 38, 96]. Still narrower linewidths may also be possible in spectroscopic measurements of the Zeeman and hyperfine structure of the ground state of trapped Dy [48], other rare-earth elements, and of the long-lived states of rare-earth ions in doped materials.

Optical transition energies in trapped ion or neutral atom clocks may also be sensitive to electrons' $c_{\mu\nu}$, as might measurements of transitions between electronic and ro-vibrational states of some molecules. The latter might also provide access to analogous proton and neutron anomalies. The sensitivity of each system depends on the scalar and quadrupole moments of the momentum of the states involved, the derivation of which will be the subject of future work.

3.2 Frame Dependence of $\delta\omega_{\rm rf}$

The laboratory frame components of the $c_{\mu\nu}$ tensor are found in terms of the sun-centered equatorial frame (SCCEF) components by requiring that the Lagrangian of Eq. (3.1) be invariant under the observer Lorentz transformation between frames. This condition leads to

$$c_{\mu\nu} = c_{MN}\Lambda_\mu^M\Lambda_\nu^N, \tag{3.5}$$

where c_{MN} is the c tensor defined in the SCCEF. In the SCCEF the Z axis points along the Earth's rotation axis, the $X-Y$ plane is the Earth's equatorial plane, and the X axis points in the direction of the Sun from Earth at the vernal equinox. The Lorentz transformation Λ_μ^M is a rotation, dependent on experimental geometry and the rotation of the Earth, to align the laboratory defined axes with these SCCEF axes followed by a boost, determined mainly by the Earth's orbital velocity, to the rest frame of the Sun. Our laboratory frame is defined such that z is parallel to the quantization axis defined by the polarization of the rf field. Thus z points $\theta = 15^\circ$ north of east, x points $\theta = 15^\circ$ east of south, and y points vertically down. The rotation from the SCCEF to the laboratory frame is given by

$$R = \begin{pmatrix} \cos\chi\cos\theta\cos\omega T_\oplus - \sin\theta\sin\omega T_\oplus & \sin\theta\cos\omega T_\oplus + \cos\chi\cos\theta\sin\omega T_\oplus & -\sin\chi\cos\theta \\ -\sin\chi\cos\omega T_\oplus & -\sin\chi\sin\omega T_\oplus & -\cos\chi \\ -\cos\chi\sin\theta\cos\omega T_\oplus - \cos\theta\sin\omega T_\oplus & \cos\theta\cos\omega T_\oplus - \cos\chi\sin\theta\sin\omega T_\oplus & \sin\chi\sin\theta \end{pmatrix}, \tag{3.6}$$

where $\chi = 52.1^\circ$ is the colatitude of our laboratory, ω is the angular frequency of the Earth's rotation in the SCCEF (*i.e.*$2\pi\times$ an inverse sidereal day), and $T_\oplus$ is measured from the first time that East, as measured in the laboratory, and the SCCEF X-axis coincides after a vernal equinox. The boost of the laboratory in the SCCEF frame is given by [36]

$$\vec{\beta} = \begin{pmatrix} \beta_\oplus \sin\Omega T - \beta_L \sin\chi \sin\omega T \\ -\beta_\oplus \cos\eta \cos\Omega T + \beta_L \sin\chi \cos\omega T \\ -\beta_\oplus \sin\eta \cos\Omega T \end{pmatrix}, \tag{3.7}$$

where $\eta = 23.4^\circ$ is the angle between the ecliptic plane and the Earth's equatorial plane, $\beta_\oplus = 2\pi(1\text{ a.u.})/c(1\text{ yr}) \simeq 10^{-4}$ is the boost from the Earth's orbital velocity, $\beta_L = R_\oplus\omega \simeq 1.5\times10^{-6}$ is the boost from the rotational velocity of a point on the Earth's equator, $2\pi/\Omega$ is a sidereal year, and T is the time since the epoch, chosen to be the vernal equinox in the year 2000 [36]. The boost $\beta_L \sin\chi$, though included in our fits, is too small to make a significant contribution to our fits, and will henceforth be dropped from this discussion.

Since the transformation between frames is time-dependent, constant values of c_{MN} in the SCCEF give rise to time varying frequency shifts in the laboratory value of $c_{\mu\nu}$, and thus to time variations in $\delta\omega_{\rm rf}$, via Eq. 3.4. Since c_{MN} also gives rise to an anomalous gravitational redshift, there is an additional contribution proportional to c_{TT}, such that $\delta\omega_{\rm rf} \approx \mp(5\times10^{16}$ Hz$) \times 2\Delta U/(3c^2)\cos(\Omega T - \phi_\odot)$, as given in Eq. (3.4), where $\Delta U \sim 1.7\times10^{-10}c^2$ is the amplitude of the Earth's yearly modulation in the solar gravitational potential due to the eccentricity of the Earth's orbit, and $\phi_\odot$ is such that $\cos(\Omega T - \phi_\odot)$ is minimized at perihelion ($\sim$Jan 3).

The c_{JK} coefficients contribute leading order energy shifts at much shorter time scales (daily) than the c_{TJ} and c_{TT} coefficients (yearly). As such, the c_{JK} coefficients are constrained using a single long data set acquired over the course of one day to minimize the influence of systematic effects acting on long time scales. To fit the c_{JK} terms, we assume that the parity-odd c_{TJ} coefficients are as constrained by astrophysical observations [37], and that the contribution of the c_{TT} term to the daily modulation of $\delta\omega_{\rm rf}$ is negligible. Although we retain all terms up to $O(\beta_\oplus^2)$ in our fit function, the dominant terms that are relevant to our fit are

$$\delta\omega_{\rm rf} = A + \sum_j \left(S_j \sin\omega_j T + C_j \cos\omega_j T\right), \tag{3.8}$$

where A is an independent offset parameter for each isotope, and the relevant frequencies ω_j, and quadratures S_j and C_j which contain the relevant components of c_{JK}, are summarized in Table 3.3. Since our experiment alternates between measuring $\delta\omega_{\rm rf}$ for ^{162}Dy and ^{164}Dy, we do not directly compare $\delta\omega_{\rm rf}$ for the two isotopes. We therefore perform a simultaneous fit of the separate functions (3.8) for each isotope, subject to the constraint that the values of c_{JK} must be the same for both.

The c_{TJ} and c_{TT} coefficients are constrained using data acquired at irregular intervals over two years. To fit the c_{TJ} and c_{TT} terms, we set c_{JK} to zero, and drop terms proportional to $\beta_\oplus^2$ that do not multiply c_{TT}, since existing bounds on $c_{X+Y} \equiv c_{XX} + c_{YY}$ are sufficient to ensure

ω_j	S_j	C_j
$\omega_\oplus$	$3\mathcal{Q}\left(c_{XZ}\sin\chi\sin 2\theta + c_{YZ}\sin 2\chi\sin^2\theta\right)$	$3\mathcal{Q}\left(c_{XZ}\sin 2\chi\sin^2\theta - c_{YZ}\sin\chi\sin 2\theta\right)$
$2\omega_\oplus$	$-\frac{3}{2}\mathcal{Q}\Big[c_{X-Y}\cos\chi\sin 2\theta - \frac{1}{2}c_{XY}\left(1+3\cos 2\theta - 2\cos 2\chi\sin^2\theta\right)\Big]$	$3\mathcal{Q}\Big[c_{XY}\cos\chi\sin 2\theta + \frac{1}{8}c_{X-Y}\left(1+3\cos 2\theta - 2\cos 2\chi\sin^2\theta\right)\Big]$
2Ω	$-\frac{5}{3}\mathcal{S}\beta_\oplus^2\left(c_{XX}\cos\eta + c_{YY}\sin\eta\right)$	$-\frac{5}{6}\mathcal{S}\beta_\oplus^2\left(c_{XX} - c_{YY}\cos^2\eta - c_{ZZ}\sin^2\eta - c_{YZ}\sin 2\eta\right)$

Table 3.3: Dominant time-varying terms in the fit for the c_{JK} coefficients. The frequencies $\omega_\oplus$ and Ω are the sidereal-day and yearly frequencies, respectively. The colatitude of the experiment is given by $\chi \sim 52.1°$, $\theta \sim 15°$ is the angle the quantization axis is rotated towards the South from West, and $\eta \sim 23.4°$ is the angle between the ecliptic and the Earth's equatorial plane. The orbital boost is $\beta_\oplus \sim 10^{-4}$. The constants $\mathcal{S} \sim \mp 5 \times 10^{16}$ Hz and $\mathcal{Q} \sim \mp 9.1 \times 10^{14}$ Hz are the scalar and quadrupole shifts, respectively, from Eq. (3.4). For ease of comparison with Table 3.2, we have defined $c_{X-Y} \equiv c_{XX} - c_{YY}$ and $c_{X+Y} \equiv c_{XX} + c_{YY}$. Additional terms of $O(\mathcal{Q}\beta_\oplus^2)$ have been suppressed, although they are included in our fits.

its doubly boost-suppressed contribution to $\delta\omega_{\rm rf}$ is negligible at our level of precision [36]. The fit function is

$$\delta\omega_{\rm rf} = A + MT + \sum_j \left(S_j \sin\omega_j T + C_j \cos\omega_j T\right), \tag{3.9}$$

where as before, A is an isotope-dependent offset, and the MT term is applied to remove any linear drifts. The relevant frequencies ω_j, and quadratures S_j and C_j, which contain the relevant components of c_{TJ} and c_{TT}, are summarized in Table 3.4. We perform a joint fit on the ^{162}Dy and ^{164}Dy data as before, and note an apparently large signal for $c_{T(Y-Z)} \approx (38 \pm 5) \times 10^{-13}$, roughly 7.6 times the statistical error bar. As such a result would be inconsistent with other experiments [36], we suspect it may be due to modulated systematic errors that we cannot fully distinguish from our model function with the existing dataset. To estimate these errors, we fit the same data to a modified fit function that does not change sign for the two Dy isotopes, thus maximizing our sensitivity to any common-mode systematics, and replace our original statistical error bars on each coefficient with their magnitudes in the fit to the modified function, if they are greater. If our original signal for $c_{T(Y-Z)}$ were not due to systematics, and thus truly due to Lorentz symmetry violation, we would expect to obtain a small value for $c_{T(Y-Z)}$ in the fit to the modified function. Instead, we observe that the mean value of $c_{T(Y-Z)}$ without isotopic sign reversal is nearly as large as it is for the fit to the Lorentz-violating model, and thus conclude that this is not evidence for violation of LLI. On the other hand, our estimates of the systematic error in our fits to c_{TX} and $c_{T(Y+Z)}$ is comparatively quite low. This is consistent with the hypothesis that our systematic background modulates with a period of one or half a day, and averages out over longer times, since our sensitivity to c_{TX} and $c_{T(Y+Z)}$ comes primarily from the once-yearly modulated scalar term in Eq. (3.4), while $c_{T(Y-Z)}$ is equally sensitive to both yearly and daily modulations proportional to the quadrupole term (see Table 3.4).

In both cases, the uncorrelated combinations of coefficients reported in Table 3.2 were found by diagonalizing the covariance matrix from the least-squares fit to Eqs. (3.8) and (3.9).

ω_j	S_j	C_j
Ω	$\frac{10}{3}\mathcal{S}\beta_\oplus c_{TX} + \frac{2\Delta U}{3c^2}\mathcal{S}c_{TT}\sin\phi_\odot$	$-\frac{10}{3}\mathcal{S}\beta_\oplus\left(c_{TY}\cos\eta + c_{TZ}\sin\eta\right) + \frac{2\Delta U}{3c^2}\mathcal{S}c_{TT}\cos\phi_\odot$
2Ω	-	$\frac{3}{16}\mathcal{Q}\beta_\oplus^2 c_{TT}\sin^2\eta\left(1+3\cos 2\theta+6\cos 2\chi\sin^2\theta\right)$
$\omega_\oplus - 2\Omega$	$\frac{3}{8}\mathcal{Q}\beta_\oplus^2 c_{TT}\left(2\sin\eta+\sin 2\eta\right)\sin 2\chi\sin^2\theta$	$-\frac{3}{8}\mathcal{Q}\beta_\oplus^2 c_{TT}\left(2\sin\eta+\sin 2\eta\right)\sin\chi\sin 2\theta$
$\omega_\oplus - \Omega$	$-\frac{3}{2}\mathcal{Q}\beta_\oplus c_{TX}\sin\eta\sin\chi\sin 2\theta$	$\frac{3}{2}\mathcal{Q}\beta_\oplus\left[c_{TY}\sin\eta + c_{TZ}(\cos\eta+1)\right]\sin\chi\sin 2\theta$
$\omega_\oplus$	$\frac{3}{4}\mathcal{Q}\beta_\oplus^2 c_{TT}\sin 2\eta\sin 2\chi\sin^2\theta$	$-\frac{3}{4}\mathcal{Q}\beta_\oplus^2 c_{TT}\sin 2\eta\sin\chi\sin 2\theta$
$\omega_\oplus + \Omega$	$-\frac{3}{2}\mathcal{Q}\beta_\oplus c_{TX}\sin\eta\sin\chi\sin 2\theta$	$\frac{3}{2}\mathcal{Q}\beta_\oplus\left[c_{TY}\sin\eta + c_{TZ}(\cos\eta-1)\right]\sin\chi\sin 2\theta$
$\omega_\oplus + 2\Omega$	$-\frac{3}{8}\mathcal{Q}\beta_\oplus^2 c_{TT}\left(2\sin\eta-\sin 2\eta\right)\sin 2\chi\sin^2\theta$	$\frac{3}{8}\mathcal{Q}\beta_\oplus^2 c_{TT}\left(2\sin\eta-\sin 2\eta\right)\sin\chi\sin 2\theta$
$2\omega_\oplus - 2\Omega$	$\frac{3}{2}\mathcal{Q}\beta_\oplus^2 c_{TT}\cos^4\frac{\eta}{2}\cos\chi\sin 2\theta$	$-\frac{3}{8}\mathcal{Q}\beta_\oplus^2 c_{TT}\cos^4\frac{\eta}{2}\left(1+3\cos 2\theta-2\cos 2\chi\sin^2\theta\right)$
$2\omega_\oplus - \Omega$	$-3\mathcal{Q}\beta_\oplus\cos^2\frac{\eta}{2}\Big[c_{TY}\cos\chi\sin 2\theta$ $+\frac{1}{4}c_{TX}\left(1+3\cos 2\theta-2\cos 2\chi\sin^2\theta\right)\Big]$	$-3\mathcal{Q}\beta_\oplus\cos^2\frac{\eta}{2}\Big[c_{TX}\cos\chi\sin 2\theta$ $-\frac{1}{4}c_{TY}\left(1+3\cos 2\theta-2\cos 2\chi\sin^2\theta\right)\Big]$
$2\omega_\oplus$	$-\frac{3}{2}\mathcal{Q}\beta_\oplus^2 c_{TT}\sin^2\eta\cos\chi\sin 2\theta$	$\frac{3}{16}\mathcal{Q}\beta_\oplus^2 c_{TT}\sin^2\eta\left(1+3\cos 2\theta-2\cos 2\chi\sin^2\theta\right)$
$2\omega_\oplus + \Omega$	$3\mathcal{Q}\beta_\oplus\sin^2\frac{\eta}{2}\Big[c_{TY}\cos\chi\sin 2\theta$ $+\frac{1}{4}c_{TX}\left(1+3\cos 2\theta-2\cos 2\chi\sin^2\theta\right)\Big]$	$3\mathcal{Q}\beta_\oplus\sin^2\frac{\eta}{2}\Big[c_{TX}\cos\chi\sin 2\theta$ $-\frac{1}{4}c_{TY}\left(1+3\cos 2\theta-2\cos 2\chi\sin^2\theta\right)\Big]$
$2\omega_\oplus + 2\Omega$	$\frac{3}{2}\mathcal{Q}\beta_\oplus^2 c_{TT}\sin^4\frac{\eta}{2}\cos\chi\sin 2\theta$	$-\frac{3}{8}\mathcal{Q}\beta_\oplus^2 c_{TT}\sin^4\frac{\eta}{2}\left(1+3\cos 2\theta-2\cos 2\chi\sin^2\theta\right)$

Table 3.4: Dominant time-varying terms in the fit for the c_{TJ} and c_{TT} coefficients. The frequencies $\omega_\oplus$ and Ω and the sidereal-day and yearly frequencies, respectively. The colatitude of the experiment is given by $\chi \sim 52.1°$, $\theta \sim 15°$ is the angle the quantization axis is rotated towards the South from West, and $\eta \sim 23.4°$ is the angle between the ecliptic and the Earth's equatorial plane. The orbital boost is $\beta_\oplus \sim 10^{-4}$. The constants $\mathcal{S} \sim \mp 5\times 10^{16}$ Hz and $\mathcal{Q} \sim \mp 9.1\times 10^{14}$ Hz are the scalar and quadrupole shifts, respectively, from Eq. (3.4). Additional terms of $O(\mathcal{Q}\beta_\oplus)$ proportional to c_{TJ} have been suppressed, although they are included in our fits. The gravitational terms appear at $\sin\Omega T$ and $\cos\Omega T$ due to a phase offset $\phi_\odot = 10.4°$ between the oscillation of the boost vector (measured from the vernal equinox) and the oscillation of the Earth in the Solar gravitational potential (with perihelion on Jan. 3rd). The amplitude of the Earth's modulation in the Solar gravitational potential is $\Delta U/c^2 \approx 1.65\times 10^{-10}$.

4 — Systematics

Systematics are imperfections in the experimental apparatus that give rise to measured transition frequencies that are different from some 'true' values. These effects can be divided into two categories: stable systematics that do not vary in time and unstable systematics that may vary in some non-random fashion. Note that the distinction between systematic and random statistical errors is often one of semantics. Statistical errors are assumed to be any quantity that varies rapidly relative to a characteristic measurement time and randomly so as to average to zero over repeated measurements. We concern ourselves with unstable systematics that might mimic variation of α or a non-zero $c_{\mu\nu}$.

The following discussion of systematics is relevant primarily to the variation of α results and the values presented in Table 2.2. In that analysis the data collected over the course of a day are averaged down to a single frequency measurement. The systematics discussed here are assumed to vary over the long time periods between days on which data have been collected. The instability of the systematics is assessed and used as a systematic uncertainty for each day of data. This is assigned by adding in quadrature to the statistical error bar for each day.

The constraint on $c_{\mu\nu}$ relies on the ability to resolve signals modulated at relatively high frequencies and the data must be kept close to its original form of many frequency measurements spread over the course of hours at a time. Systematic uncertainties cannot be properly added to the data in this form without a better model for the temporal behavior of the systematic effects.

4.1 Residual amplitude modulation

Residual amplitude modulation (RAM) of the frequency-modulated electric field used to probe the $B \to A$ transition frequency can be described by writing the electric field as

$$E(t) = E_0 \left[1 + \epsilon \cos\left(\Omega T + \phi_{AM}\right)\right] \cos\left(\omega t + m \sin \Omega t\right), \tag{4.1}$$

where ω and Ω are the carrier and modulation frequencies, m is the modulation index, ϵ characterizes the size of the RAM, and ϕ_{AM} is an arbitrary phase that is generally assumed to be 0. As shown in Fig. 4.1, RAM of this form creates an asymmetry in the electric field

sideband amplitudes, leading to a distortion of the resonant lineshape and shift of the first-harmonic zero crossing. The derivation of an analytic formula for lock-in detected, frequency- and amplitude-modulated lineshapes can be found in Appendix C. Summing Eq. (C.20) over only the $k = 0, \pm 1$ terms, the frequency shift of the first-harmonic zero crossing due to RAM is found to be

$$\frac{\delta\omega}{2\pi} \approx \epsilon \left(\frac{8m\Omega}{\gamma^2 + 4\Omega^2} + \frac{4m\Omega\cos(\phi)}{\gamma(2\Omega\sin(\phi) - \gamma\cos(\phi))} \right)^{-1}, \tag{4.2}$$

where ϕ is the reference phase of the lock-in amplifier. For a modulation frequency $\Omega/(2\pi) =$ 10 kHz, modulation index $m = 1$, transition linewidth $\gamma/(2\pi) = 40$ kHz, and ϕ set to maximize the first-harmonic slope at zero crossing, the shift is predicted to be $\delta\omega = 4.1 \times 10^4\,\epsilon$ Hz. Reaching the proposed statistical limit of $\delta\omega/(2\pi) = 10$ mHz therefore requires minimizing and stabilizing RAM at the level of $\epsilon \leq 2.5 \times 10^{-7}$. In the following sections we discuss the origins of RAM, a method for measuring the parameter ϵ, and a technique to eliminate sensitivity to RAM.

A more accurate analytic formula for the RAM induced shift was obtained by summing Eq. (C.20) over $k = 0, ..., \pm 5$, which finds that $\delta\omega/(2\pi) = 4.4 \times 10^4\,\epsilon$ Hz. Equation (4.2) is then a good estimation for the shift at the 7% level, however all results discussed in this section are understood to use the more accurate formula.

Effective RAM

Residual amplitude modulation is assumed to have two origins: intrinsic RAM due to imperfect frequency modulation of the electric field, and effective RAM due to resonances (etalons) in the radio-frequency transmission line. In this section we attempt to show that intrinsic RAM occuring at the modulation frequency is equivalent to effective RAM.

We assume that transmission line etalons are much broader than the atomic resonance and can be described by a linear frequency dependence of the transmitted power

$$P(\omega)/P_0 = \frac{\beta}{2\pi}(\omega - \omega_0) + 1, \tag{4.3}$$

where P_0 is the electric field power at the unshifted atomic transition frequency ω_0. The factor of $1/(2\pi)$ is included so that β characterizes the fractional change in power per unit frequency rather than angular frequency.

In order to relate β to the RAM parameter ϵ, we consider a modulated electric field with carrier frequency set to ω_0. The power contained in a discrete frequency component of the electric field at $\omega_0 + k\Omega$ is

$$P_k = \left(J_k(m) + \frac{\epsilon}{2}(J_{k-1}(m) + J_{k+1}(m)) \right)^2, \tag{4.4}$$

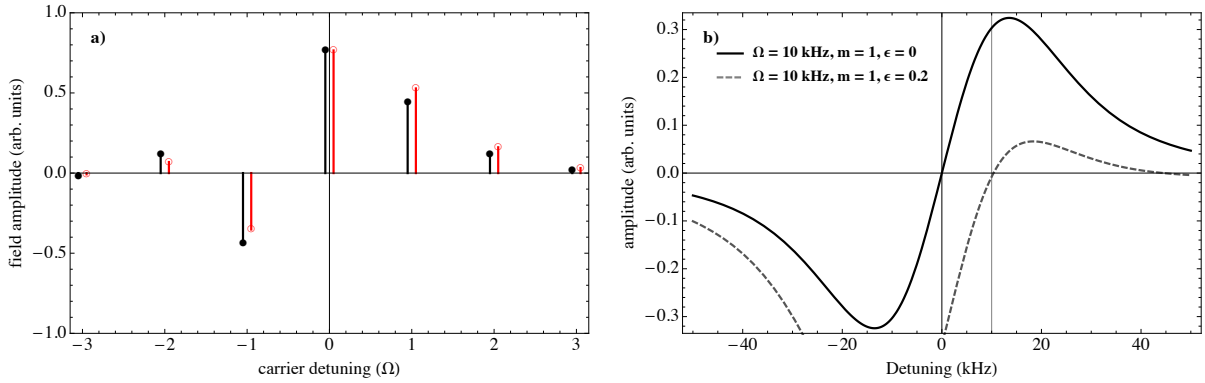

Figure 4.1: **a)** Amplitude of the discrete frequency components of the modulated electric field. Filled circles show the spectrum for pure frequency modulation with modulation index $m = 1$. Empty circles show the same spectrum with the addition of RAM with paramter $\epsilon = 0.2$.
b) Calculated first-harmonic lineshapes with the same modulation parameters. The lock-in phase has been chosen to maximize the slope of the zero-crossing. For $\epsilon = 0.2$ the zero crossing of the dispersive line shape has shifted by ~ 10 kHz.

where $J_k(m)$ is a Bessel function of the first kind and $k = 0, \pm 1, \pm 2... \rightarrow \pm\infty$. It is convenient to set $\omega_0 = 0$. The ratio of powers in the $\pm k$ sidebands can then be written

$$\frac{P_{+k}}{P_{-k}} = \frac{P(+k\Omega)}{P(-k\Omega)}. \tag{4.5}$$

The ratio P_{+k}/P_{-k} is the ratio of powers in the $\pm k$ sidebands of a frequency modulated signal with intrinsic RAM, characterized by ϵ, that is passed through a perfect transmission line. The ratio $P(+k\Omega)/P(-k\Omega)$ is the ratio of powers in the $\pm k$ sidebands of a frequency modulated signal without RAM that is passed through transmission line with a linear frequency dependence of the power characterized by β. Equation (4.5) gives the expression

$$\left(\frac{J_k(m) + \frac{\epsilon}{2}[J_{k-1}(m) + J_{k+1}(m)]}{J_{-k}(m) + \frac{\epsilon}{2}[J_{-k-1}(m) + J_{-k+1}(m)]}\right)^2 = \frac{\beta k\Omega/(2\pi) + 1}{1 - \beta k\Omega/(2\pi)}. \tag{4.6}$$

We us the relationship $J_{-k}(m) = (-1)^k J_{+k}(m)$ and assume that $\epsilon \ll 1$ and $\beta k\Omega \ll 1$. Rearranging and ignoring terms $O(\epsilon^2)$ we find that

$$\epsilon \approx \frac{J_k(m)}{J_{k-1}(m) + J_{k+1}(m)} \frac{\beta}{2\pi} k\Omega = \frac{m}{4\pi}\beta\Omega. \tag{4.7}$$

This allows us to relate a frequency dependent power characterized by β to an effective RAM characterized by ϵ.

Conceptual model

We now consider a simple model that allows us to estimate the shift due to transmission line resonances. The atomic lineshape is assumed to be Lorentzian with amplitude that scales linearly with electric-field intensity,

$$S(\omega) = \frac{P(\omega)}{P_0}\frac{\gamma^2/4}{\omega^2+\gamma^2/4}, \tag{4.8}$$

where we have set the resonant frequency $\omega_0 = 0$ for convenience. Using Eq. (4.3) to describe the transmission line we have

$$S(\omega) = \frac{\gamma^2}{4}\frac{\beta\omega/(2\pi)+1}{\omega^2+\gamma^2/4}. \tag{4.9}$$

The first-harmonic detected lineshape in frequency-modulated spectroscopy can be approximated by the first derivative of the underlying lineshape, although the reference phase dependence is lost. The transition frequency is assumed to be where the first-harmonic lineshape equals zero, so to approximate the frequency shift generated by β we set the derivative of Eq. (4.9) equal to 0 at frequency $\delta\omega$,

$$\left.\frac{dS(\omega)}{d\omega}\right|_{\delta\omega} = \frac{\gamma^2}{4}\left(\frac{\beta/(2\pi)}{\delta\omega^2+\gamma^2/4} - \frac{2\delta\omega(\beta\delta\omega/(2\pi)+1)}{(\delta\omega^2+\gamma^2/4)^2}\right) = 0. \tag{4.10}$$

The solution for $\delta\omega$ is the quadratic equation $\beta/(2\pi)\delta\omega^2 + 2\delta\omega - \beta/(2\pi)\gamma^2/4 = 0$ with two solutions

$$\delta\omega_\pm = \frac{-1 \pm \sqrt{1+(\beta/(2\pi))^2\gamma^2/4}}{\beta/(2\pi)}. \tag{4.11}$$

The $\delta\omega_-$ solution is a non-physical solution corresponding to a local minimum where the power, $P(\delta\omega_-)$, is less than zero. This is a consequence of assuming the coupled power always scales linearly with frequency. Taking $\delta\omega_+$ to be the measured resonance frequency and assuming $(\beta/(2\pi))^2\gamma^2/4 \ll 1$ we obtain the expected shift,

$$\delta\omega \approx \frac{1}{16\pi}\beta\gamma^2. \tag{4.12}$$

This is written in terms of the RAM parameter ϵ by solving Eq. (4.7) for β, which yields

$$\delta\omega \approx \frac{1}{4}\frac{1}{m\Omega}\epsilon\gamma^2. \tag{4.13}$$

When $m = 1$, $\Omega/(2\pi) = 10$ kHz, and $\gamma/(2\pi) = 40$ kHz we find the shift $\delta\omega/(2\pi) \approx 40\epsilon$ kHz, in excellent agreement with result of Eq. (4.2), from a much more sophisticated derivation.

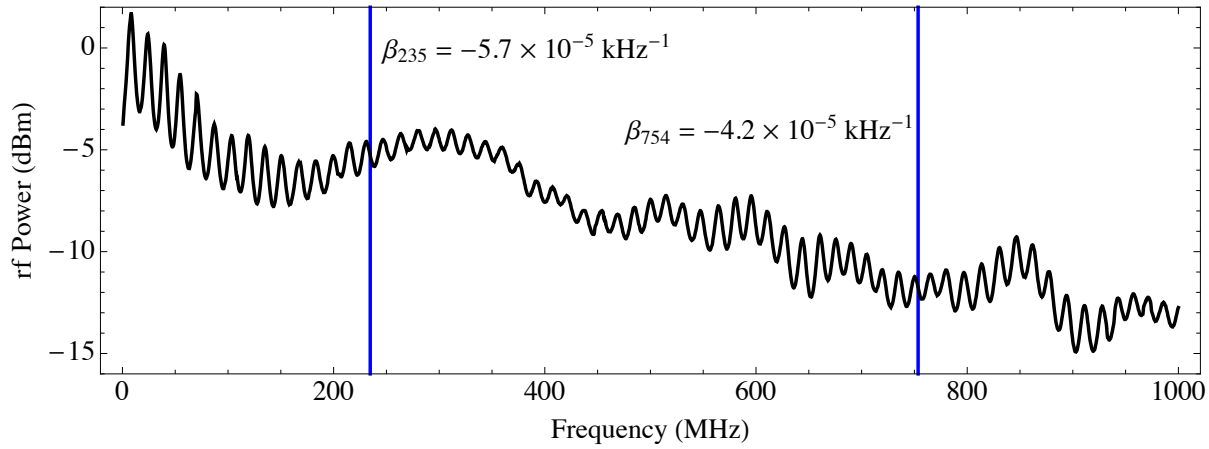

Figure 4.2: Frequency dependence of the rf power incident on the SMA vacuum feed-throughs. Vertical lines denote the position of the ^{162}Dy, 235 MHz and ^{164}Dy, 754 MHz transitions. The complex structure suggests the existence of multiple transmission line etalons with different free-spectral ranges.

Measurement of RAM

Characterizing and eliminating the systematic uncertainty due to RAM first requires the ability to measure it. In Ref. [61] a radio-frequency mixer was used to directly measure the quantity $|E(t)|^2$. For a purely frequency-modulated field this quantity contains a DC component and rapidly oscillating terms around 2ω. In the presence of non-zero ϵ, however, low-frequency terms at Ω and 2Ω appear with predictable relative amplitudes based on Eq. (4.1). The amplitude of these components was found to be consistent with $\epsilon \sim 10^{-4}$, corresponding to frequency shifts of ~ 4 Hz. The accuracy of the measurement, however, was uncertain due to possible imperfections in the mixing circuit.

To confirm these values, we attempted to characterize the frequency dependence of the rf transmission line. The frequency of an rf synthesizer was scanned from $1 - 1000$ MHz at constant amplitude. The power incident on the electric-field vacuum feedthrough was measured with a calibrated directional coupler and spectrum analyzer. The results of this scan are shown in Fig. 4.2. The β parameters obtained from the local slopes around 235 MHz and 754 MHz are consistent with $\epsilon \sim -2.5 \times 10^{-4}$ for $m = 1$ and $\Omega/(2\pi) = 10$ kHz. These values are consistent with the values in [61].

The first policy implemented to reduce the effect of RAM was a redesign of the rf transmission line. The dominant fringe structure in Fig. 4.2 has a free-spectral range of ~ 16 MHz, similar in size to the ~ 20 MHz free-spectral range expected of the nearly 5 meter long coaxial cables separating the rf generator, rf amplifier, and vacuum chamber (assuming PTFE insulation). On August 24, 2011 all cable lengths were shortened to less than 1 meter, and narrow band radio-frequency circulators were installed to terminate reflections and sup-

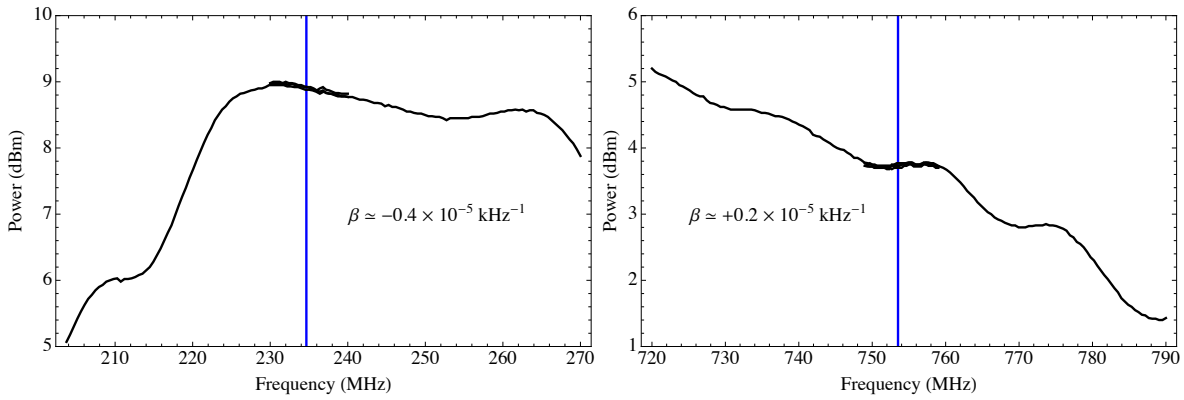

Figure 4.3: Frequency dependence of the rf power incident on the vacuum feed-throughs for the ^{162}Dy, 235 MHz (left) and ^{164}Dy, 754 MHz (right) transitions.

press etalons in the transmission line. The transmission line frequency dependence around 235 MHz and 754 MHz, with the appropriate circulators installed, is shown in Fig. 4.3. The local slopes were reduced by nearly two orders of magnitude, corresponding to $\epsilon \approx -8 \times 10^{-7}$ and $\epsilon \approx 4 \times 10^{-7}$ near 235 MHz and 754 MHz, respectively.

A direct method of characterizing residual amplitude modulation of the electric field makes use of the phase dependent frequency shift in Eq. (4.2). Varying the detection phase of the lock-in amplifier allows a direct measurement of ϵ using the atoms as a probe. Figure 4.4 demonstrates this phase dependence of measured transition frequencies before and after redesign of the transmission line. Fitting Eq. (4.2) to these data via least-squares permits a direct measurement of ϵ.

Equation (4.2) also suggests a phase, $\tan\phi = \gamma/(2\Omega)$, where the sensitivity to RAM goes to zero. The least-squares fits in Fig. 4.4 establish this RAM insensitive reference phase for the lock-in amplifier, $\phi = 60.7(5)^\circ$. Standard data taking protocol since installation of the rf circulators and transmission line has been to acquire data at this phase.

While the presence of RAM can generate an apparent frequency shift, the *instability* of RAM is relevant for assessing systematic uncertainties in the long term measurement of Dy transition frequencies. The value of ϵ has been regularly measured with this procedure since 2011-05-29. The summary of these measurements is shown in Fig. 4.5, where the installation of the new transmission line is apparent by the sudden reduction in ϵ. The instability of RAM, σ_ϵ, is taken to be half of the interval containing 68% of measurements.

Before the new transmission line was installed the RAM sensitivity was $\delta\omega/(2\pi) \approx 4.4 \times 10^4 \epsilon$ Hz. The systematic uncertainty is therefore ~ 0.5 Hz for the three instances where RAM was measured with this transmission line. For all measurements before 2011-05-29, that used the same transmission line, a conservative systematic uncertainty of 1 Hz is applied to reflect the lack of knowledge regarding RAM.

The installation of the new rf transmission line and adoption of operating at the RAM

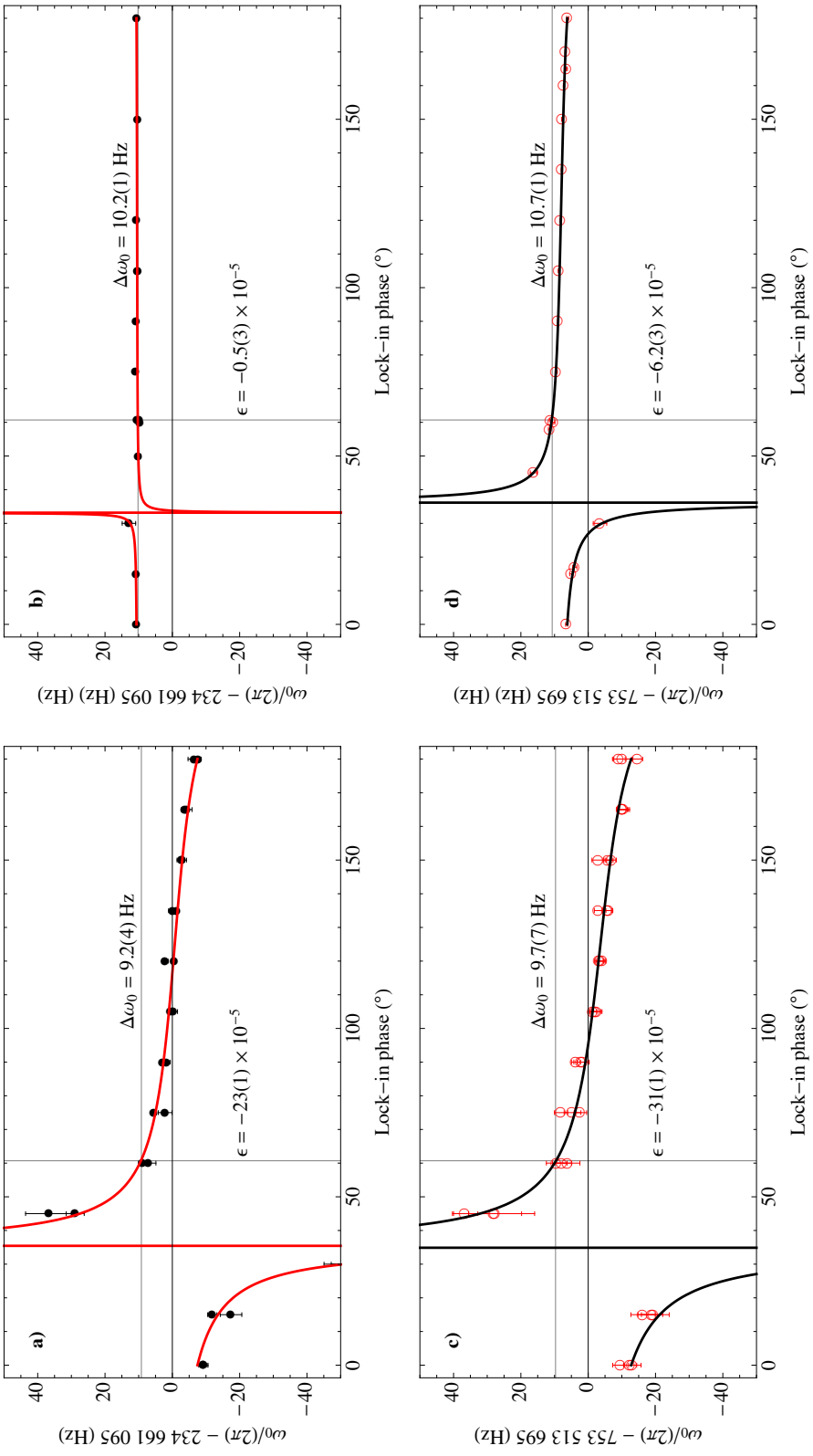

Figure 4.4: Phase dependence of measured transition frequencies. a) & b) Phase dependence of the ^{162}Dy transition frequency before and after modification of the transmission line, respectively. c) & d) Phase dependence of the ^{164}Dy transition frequency before and after modification of the transmission line, respectively. Solid lines correspond to nonlinear least-squares fits of Eq. (4.2) to the data. The intersection of light gray lines indicates the RAM insensitive transition frequency and lock-in phase.

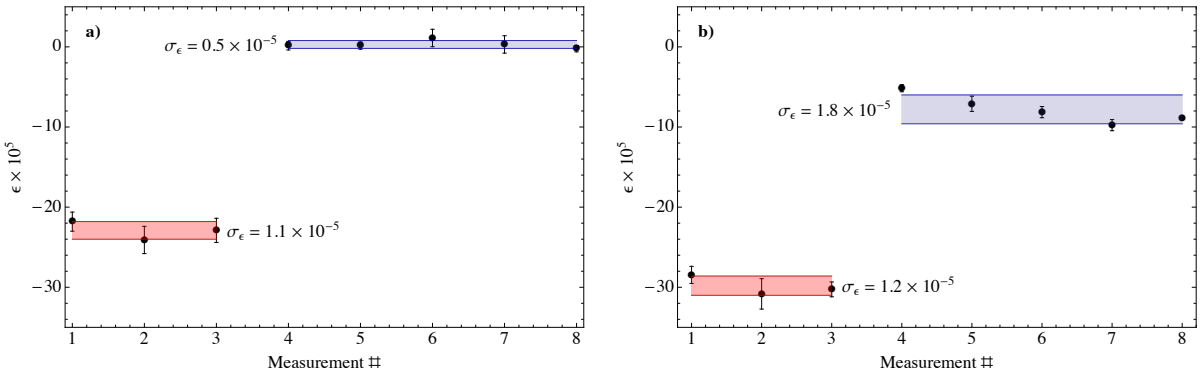

Figure 4.5: Summary of RAM measurements at the a) 235 MHz, ^{162}Dy transition and b) 754 MHz, ^{164}Dy transition. The shaded interval contains $\sim 68\%$ of all measurements.

insensitive lock-in phase $\phi = 60.7(5)^\circ$ creates a discrete frequency shift between pre and post measurements. On 2011-08-24 the frequency shift between configurations was measured for ^{164}Dy and ^{162}Dy to be 15.15 Hz and 12.4 Hz, respectively. This correction has then been applied to all measurements made prior to installation of the new transmission line.

Although the new configuration is nominally insensitive to RAM, a deviation from the RAM insensitive phase can give rise to systematic shifts, estimated to be

$$\frac{\delta\omega}{2\pi} \approx 2 \times 10^3 \epsilon \delta\phi \,\mathrm{Hz}, \tag{4.14}$$

for $m = 1$, $\Omega/(2\pi) = 10$ kHz, $\gamma/(2\pi) = 40$ kHz, and $\delta\phi$ is given in degrees. We assume that the phase uncertainty is $\delta\phi \approx 0.5^\circ$, and use the assessed RAM instabilities indicated in Fig. 4.5. The contribution of RAM to long term systematic uncertainties is thus 18 mHz and 5 mHz for ^{164}Dy and ^{162}Dy, respectively.

Further improvements

The phasing procedure discusses so far comes at the expense of statistical sensitivity. With the modulation parameters presently used, $m = 1$ and $\Omega/(2\pi) = 10$ kHz, the RAM insensitive phase decreases statistical sensitivity by more than a factor of two (see App. A, Fig. A.2). This can only be regained by acquiring data for nearly four times as long due to the scaling of statistical sensitivity as $1/\sqrt{T}$. These modulation parameters, however, were chosen somewhat arbitrarily as approximately the optimal modulation parameters for the natural 20 kHz linewidth of the rf transition, rather than the 40 kHz power and transit-broadened linewidth in the apparatus. It is possible that different modulation parameters can provide reduced sensitivity to RAM without losing statistical sensitivity.

The analytic expression for the first-harmonic lineshape found in App. C has been used to predict the relative statistical sensitivity for modulation parameters assuming statistical

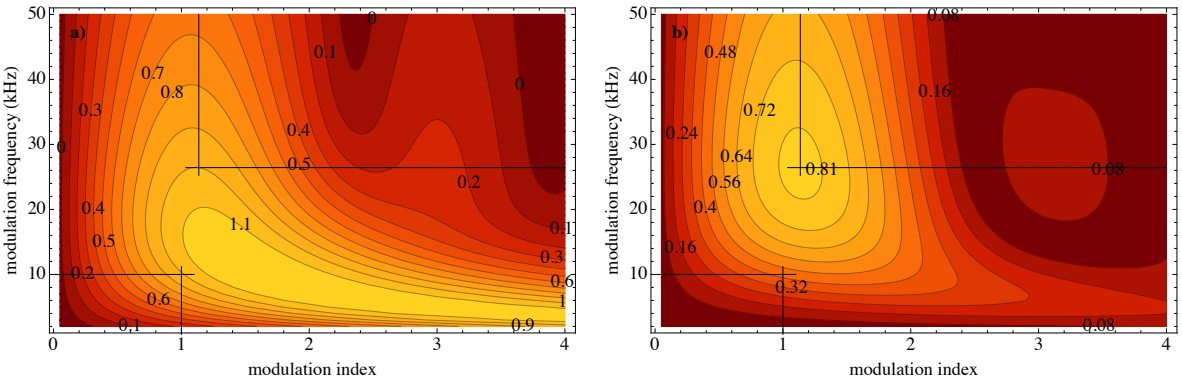

Figure 4.6: Contour lines show the projected statistical sensitivity relative to that at presently used modulation parameters for **a)** lock-in phase chosen for maximum statistical sensitivity and **b)** lock-in phase chosen to eliminate sensitivty to RAM. The intersecting gridlines indicate the present modulation parameters and the best choice of RAM insensitive modulation parameters.

sensitivity is directly proportional to the slope of the first-harmonic signal near resonance. Contour maps in modulation-parameter space of the statistical sensitivity relative to the maximum statistical sensitivity at $m = 1$, $\Omega/(2\pi) = 10$ kHz are shown in Fig. 4.6. The modulation parameters $m = 1.14$ and $\Omega/(2\pi) = 26.4$ kHz are projected to be the best choice at a RAM insensitive phase, where the statistical sensitivity drops to $\sim 83\%$ of the sensitivity at present. The maps also predict that modulation parameters $m = 1.65$ and $\Omega/(2\pi) = 10$ kHz could increase the maximum statistical sensitivity to 120% of its current value. Future work will focus on confirming these predictions.

4.2 Electronic offsets

As discussed in Appendix A, the transition frequency is measured by assuming the ratio of first- and second-harmonic lineshapes is described by a linear function

$$R(\omega) = \frac{L^1(\omega)}{L^2(\omega)} = \frac{\mathcal{M}}{2\pi}(\omega - \omega_0), \tag{4.15}$$

where the transition frequency is assumed to be $\omega = \omega_0$, where $R(\omega_0) = L^1(\omega_0) = 0$. The phase dependence of the function $L^n(\omega)$ will be ignored for now. Systematic offsets of the lock-in signals can generate a frequency shifts of zero crossing and apparent shift of the transition frequency. We will define u_1 and u_2 as the offsets of the first- and second-harmonic signals and write

$$\frac{L^1(\omega)+u_1}{L^2(\omega)+u_2} = \frac{\mathcal{M}}{2\pi}(\omega-\omega_0')$$
$$\frac{L^1(\omega)}{L^2(\omega)+u_2} + \frac{u_1}{L^2(\omega)+u_2} = \frac{\mathcal{M}}{2\pi}(\omega-\omega_0'), \tag{4.16}$$

where the zero crossing has shifted by an amount $\omega_0' - \omega_0$. If we assume that the offsets $u_{1,2}$ are small, such that $|u_{1,2}| \ll L^2(\omega)$, we can write

$$\frac{L^1(\omega)}{L^2(\omega)} - \frac{L^1(\omega)}{L^2(\omega)}\frac{u_2}{L^2(\omega)} + \frac{u_1}{L^2(\omega)} - \frac{u_1}{L^2(\omega)}\frac{u_2}{L^2(\omega)} \approx \frac{\mathcal{M}}{2\pi}(\omega-\omega_0'). \tag{4.17}$$

Taking the difference of Eq. (4.15) and Eq. (4.17) leaves us with the expression

$$\frac{L^1(\omega)}{L^2(\omega)}\frac{u_2}{L^2(\omega)} - \frac{u_1}{L^2(\omega)} + \frac{u_1}{L^2(\omega)}\frac{u_2}{L^2(\omega)} \approx \frac{\mathcal{M}}{2\pi}(\omega_0'-\omega_0). \tag{4.18}$$

Near resonance $L^1(\omega)/L^2(\omega) \approx 0$. This allows us to drop all terms containing u_2 in Eq. (4.18), and after reorganizing terms we find that

$$\frac{\delta\omega}{2\pi} \approx -\frac{u_1}{\mathcal{M}L^2(\omega)}. \tag{4.19}$$

Typical values for the inverse slope are $\mathcal{M}^{-1} \sim 2000$ Hz for the optimal lock-in phase, and $\mathcal{M}^{-1} \sim -4500$ Hz for the RAM insensitive lock-in phase, while typical values for the second-harmonic amplitude are $L^2(\omega) = 5$ mV near resonance. The sensitivity to electronic offsets of the first-harmonic signal is therefore

$$\frac{\delta\omega}{2\pi u_1} \sim \begin{cases} 400\,\text{Hz/mV} & \text{optimal phase} \\ -900\,\text{Hz/mV} & \text{RAM insensitive phase} \end{cases} \tag{4.20}$$

Reaching the goal sensitivity of 10 mHz therefore requires stabilizing electronic offsets at the level of 25 nV, or 10 nV in order to take advantage of the previously discussed RAM insensitive phase.

A preliminary measurement of electronic offsets, shown in Fig. 4.7, acquires the first-harmonic lock-in signals in the absence of the atomic signal. Mean values for the in-phase and quadrature channels are -240(9) nV and -560(9) nV, respectively. The magnitude of the first harmonic signal, ~ 600 nV, could generate an apparent shift as large as 540 mHz, although the exact size of this shift may depend on the amplitude of the atomic signal, per Eq. 4.19.

Given the high sensitivity to electronic offsets, a reliable estimate of their size and stability is crucial for characterizing the measurement error of the experiment. The previous method allows a precise measurement of electronic offsets, but does not contain information about the electronic offsets present during actual frequency measurements.

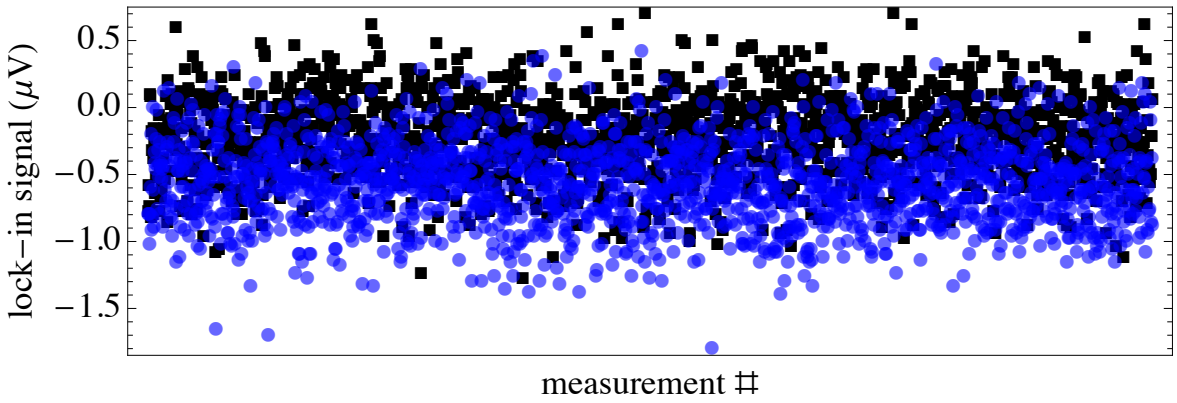

Figure 4.7: Lock-in noise measurement in the absence of atomic signals. Filled squares (circles) show the in-phase (quadrature) detection channels.

A new method was inspired by the work presented in Ref. [76], and the basic principle is demonstrated in Fig. 4.8 a). The signal size is made to vary in such a way that the electronic offsets are left unchanged. In the presence of an electronic offset, such a change will cause the apparent transition frequency to shift, allowing the offset to be measured.

Care must be taken that changing the signal size is not done at the expense of introducing other systematic shifts. As of now, the gain of the PMT is varied by changing the detector supply voltage. The slope of the first- to second-harmonic ratio, $\mathcal{M}$, the second harmonic amplitude, $L^2(\omega)$, and the transition frequency are measured for each gain setting. The transition frequency is then plotted against the quantity $(-\mathcal{M}L^2(\omega))^{-1}$, which allows the offset u_1 to be determined from the slope (see in Fig. 4.8).

The slopes for both ^{164}Dy and ^{162}Dy are consistent with one another and with zero. The electronic offset can reasonably be expected to be isotope independent, so the mean offset is $u_1 \approx 260 \pm 380$ nV. A conservative estimate of 500 nV is used to estimate systematic uncertainties for previously collected data. The uncertainties are assigned based on the second-harmonic amplitudes and inverse slopes, $\mathcal{M}^{-1}$, for each set of data.

The method presented is intended as proof of principle for allowing informed estimates of systematic uncertainties. Future work will include the calibration of electronic offsets as standard protocol, and will aim for greater precision. It should also be noted that an electronic offset that is independent of lock-in phase could negatively influence the RAM phasing procedure discussed earlier. This has not yet been investigated but is a priority for future work.

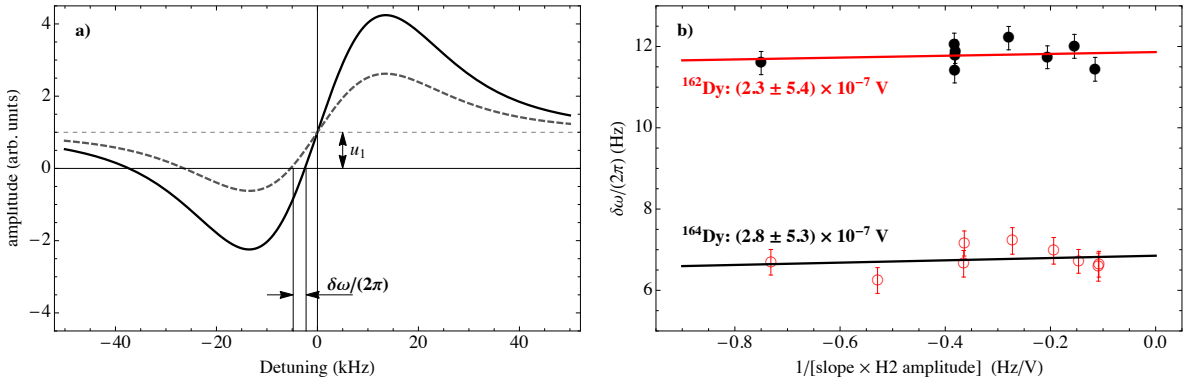

Figure 4.8: a) Varying the signal amplitude while leaving the offset u_1 unchanged creates an apparent frequency shift, allowing the offset to be estimated. b) transition frequencies for ^{164}Dy (empty circles) and ^{162}Dy are plotted against the quantity $(-\mathcal{M}L^2(\omega))^{-1}$ as explained in the main text. The slopes are consistent with zero offset at the 68% confidence level.

4.3 Zeeman shifts

Stabilizing the transition frequency in Dy is complicated by the large electronic angular momentum, which gives rise to an extraordinarily high sensitivity to stray magnetic fields. The frequency shift of an individual Zeeman transition is given by

$$\delta\nu = (g_A M_A - g_B M_B)\mu_B B,$$

where $g_{A,B}$ and $m_{A,B}$ denote the g-factors and magnetic quantum numbers of states A and B, $\mu_B \approx 1.4$ kHz/mG is the Bohr magneton, and B is the magnetic field applied along the quantization axis. If we choose the quantization axis such that our rf-electric field is linearly polarized we are restricted to $\Delta M = 0$ transitions, thus $M = M_A = M_B$. Using the g-factors from Ref. [50], the sensitivity to magnetic fields becomes

$$\frac{\delta\omega}{2\pi B} \approx M\,220\,\text{Hz/mG}. \tag{4.21}$$

Because the transition is $\Delta J = 0$ we are forbidden from operating on the the magnetic-field insensitive $M = 0 \to 0$ transition. Equation (4.21) can be averaged according to Eq. (B.4) using the normalized weights, a_M, in Table B.1. The magnetic field sensitivity of the unresolved line from this average is

$$\frac{\delta\bar{\omega}}{2\pi B} = -15(13)\,\text{Hz/mG}, \tag{4.22}$$

where $\delta\bar{\omega}/(2\pi)$ is the average shift of unresolved Zeeman transitions. This agrees with experimentally measured shifts of the unresolved line on the order of 2 Hz/mG.

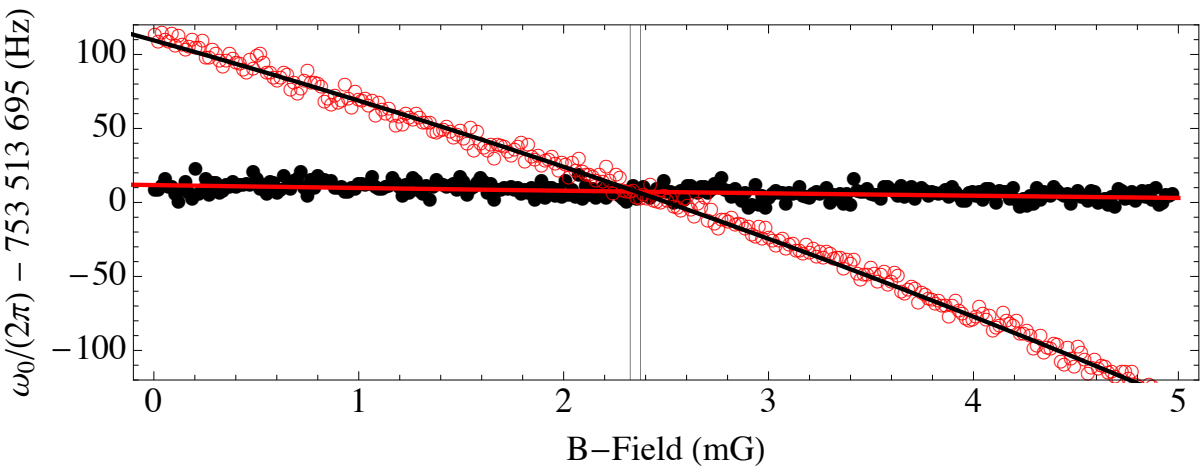

Figure 4.9: Magnetic field dependence of the Zeeman unresolved, ^{164}Dy transition. Filled and empty circles correspond to scans with and without a $\lambda/4$ plate, respectively, in the 669-nm beam path. Both sets of data are fit with quadratic functions, shown as solid lines, for the purpose of finding the crossing field. The residual shift at the crossing point, without the $\lambda/4$ plate, is $-1.7(2)$ Hz/mG.

The magnetic field along the quantization axis is canceled during each experiment with a Helmholtz coil surrounding the interaction region. The population of atoms in state B magnetic sublevels, and the sensitivity of the unresolved line to magnetic fields, can be modified by changing the polarization of the 669-nm excitation light. A vacuum feedthru allows a $\lambda/4$ plate to be inserted after the last linear polarizer in the 669-nm light beam path. The current through the Helmholtz coil is scanned (with a conversion of ~ 0.95 mG/mA) with and without the $\lambda/4$ plate while measuring the transition frequency. The magnetic field is canceled when these frequencies agree. An example scan is shown in Fig. 4.9.

The magnetic field along the quantization axis can be reliably canceled with a precision of 25 μG, the scatter of successive measurements of the crossing field. The residual magnetic field sensitivity with all linearly polarized laser excitation light is ~ 2 Hz/mG, consistent with the estimate based on population measurements. The total magnetic field induced uncertainty for each measurement is therefore assigned to be 50 mHz.

4.4 Collisional Shifts

Collisions between Dy atoms in the atomic beam and trace background gases in the vacuum chamber can lead to perturbations of the radio-frequency energy splittings between the nearly degenerate. Shifts as a function of partial pressure for various gases were measured in 2005 [75], with results re-tabulated for convenience in Table 4.1.

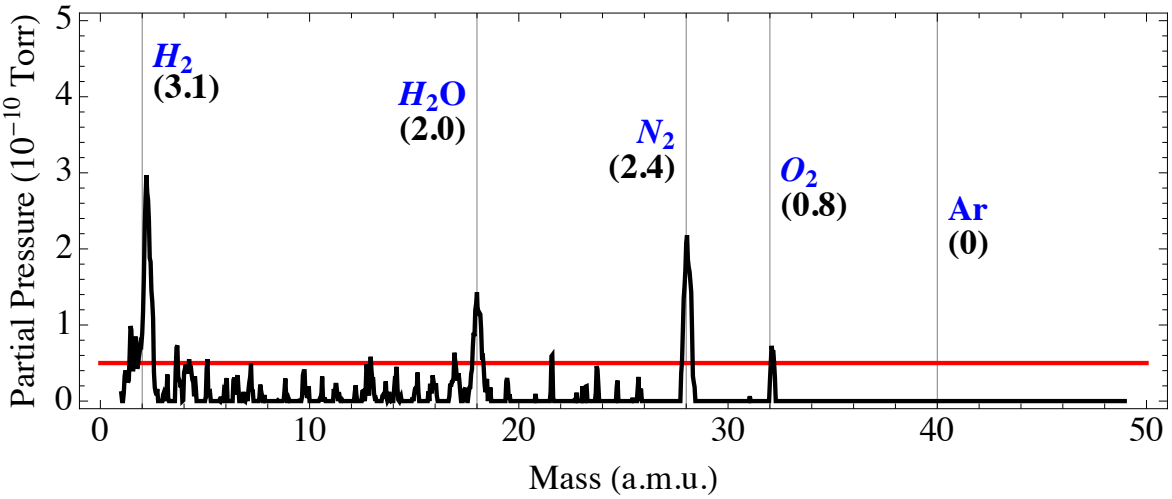

Figure 4.10: A scan of trace gases in the main interaction chamber, with the pressure given in units of 10^{-10} Torr. The horizontal line indicates the specified noise level of the RGA. The measured collisional shifts documented in Table 4.1, indicate a total shift of ~ 0.6 mHz. Collisional shifts for H_2O have not been measured, but are expected to be similar in magnitude to others.

The pressure in the main chamber is monitored with two sensors. During periods of downtime the pressure is monitored with a glass enclosed Bayard-Alpert ionization gauge from MDC Vacuum Products, with a specified lower vacuum limit of 2×10^{-10} Torr. Typical readings are $3.5(5) \times 10^{-9}$ Torr. During an experiment the ion-gauge controller has been found to contribute unwanted electronic noise to the data acquisition, so the pressure is monitored with a Stanford Research Systems RGA200 residual gas analyzer. This RGA can identify trace gases up to 200 a.m.u., with a minimum detectable partial pressure of 5×10^{-11} Torr. A typical scan of trace gases is shown in Figure 4.10. The total expected shift at these partial pressures is ~ 0.6 mHz, negligible in comparison to other effects.

Shift rates	H_2	N_2	O_2	He	Ne	Ar	Kr	Xe
(Hz/μTorr)	-0.02(2)	-1.71(3)	-1.97(25)	1.25(2)	-0.01(2)	-2.21(5)	-2.78(5)	-2.74(4)

Table 4.1: Pressure shift rates for ^{162}Dy, where the transition frequency is $\sim$234.7 MHz. The magnitude of the shift rates are approximately the same for other isotopes of Dy, whereas the sign of the shift depends on the sign of the splitting between levels A and B. This feature makes pressure shifts $\dot{\alpha}$-mimicking systematics.

5 — The ac-Stark effect

5.1 Measurement of dynamic polarizabilities in dysprosium

We report measurements of the differential polarizability between the nearly degenerate, opposite parity states in atomic dysprosium at 19797.96 cm^{-1}. The differential scalar and tensor polarizabilities due to additional states were measured for the $|M| = 7, \ldots, 10$ sublevels in ^{164}Dy and ^{162}Dy and determined to be $\overline{\boldsymbol{\alpha}}^{(0)}_{BA} = 180\,(45)_{\mathrm{stat}}\,(8)_{\mathrm{sys}}$ mHz $\mathrm{cm}^2/\mathrm{V}^2$ and $\overline{\boldsymbol{\alpha}}^{(2)}_{BA} = -163\,(65)_{\mathrm{stat}}\,(5)_{\mathrm{sys}}$ mHz $\mathrm{cm}^2/\mathrm{V}^2$, respectively. The average blackbody radiation induced Stark shift of the Zeeman spectrum was measured around 300 K and found to be $-34(4)$ mHz/K and $+29(4)$ mHz/K for the ^{164}Dy and ^{162}Dy isotopes, respectively. We conclude that ac-Stark related systematics will not limit the precision of a search for variation of the fine-structure constant, using dysprosium, down to the level of $|\dot{\alpha}/\alpha| = 2.6 \times 10^{-17}$ yr^{-1} for a one-year experiment.

This chapter is currently being prepared for submission to Physical Review A, by C.T.M. Weber, N. Leefer, and D. Budker.

5.2 Dynamic polarizabilities

The response of an atom to an external electric field is described by the linear electric polarizability. Specifically, the ac-Stark shift of an electronic energy level $|m\rangle$ due to an oscillating electric field with root mean square (rms) value E is given by [97]

$$\Delta W_m/h = -\frac{1}{2}\boldsymbol{\alpha}_m E^2, \tag{5.1}$$

where $\boldsymbol{\alpha}_m$ is the electric-dipole polarizability[1] of level m. Note that a bold $\boldsymbol{\alpha}$ will refer to polarizabilities and should not be confused with the fundamental constant, α. The polarizability of an atomic state $|m\rangle$ can be written in the form [97–99]

$$\boldsymbol{\alpha}_m = \boldsymbol{\alpha}_m^{(0)}(F) + i\boldsymbol{\alpha}_m^{(1)}(F)\frac{M}{F}(\boldsymbol{\epsilon}\times\boldsymbol{\epsilon}^*)\cdot\hat{\mathbf{z}} + \boldsymbol{\alpha}_m^{(2)}(F)\frac{3M^2 - F(F+1)}{F(2F-1)}\frac{3|\boldsymbol{\epsilon}\cdot\hat{\mathbf{z}}|^2 - 1}{2}, \tag{5.2}$$

where $\boldsymbol{\epsilon}$ is the polarization vector of the electric field, F is the total electronic angular momentum of state $|m\rangle$, M is the projection of angular momentum along the chosen quantization axis, $\hat{\mathbf{z}}$, and the quantities $\boldsymbol{\alpha}^{(0)}(F)$, $\boldsymbol{\alpha}^{(1)}(F)$, and $\boldsymbol{\alpha}^{(2)}(F)$ are, respectively, the *scalar*, *vector*, and *tensor* polarizabilities of state $|m\rangle$. These three quantities allow us to characterize ac-Stark shifts in a form independent of the experimental geometry or magnetic sublevel.

The differential ac-Stark shift of the $B \to A$ transition frequency is

$$\Delta\nu_{BA} = \frac{\Delta\omega_{BA}}{2\pi} = \left(\Delta W_B - \Delta W_A\right)/h = -\frac{1}{2}(\boldsymbol{\alpha}_B - \boldsymbol{\alpha}_A)E^2. \tag{5.3}$$

The even-mass-number isotopes of Dy have zero nuclear spin, and their total angular momentum is $F = 10$ for both states A and B. The odd-mass-number isotopes, ^{163}Dy and ^{161}Dy, have nuclear spin $I = 5/2$ with the corresponding range of total angular momenta $F = 15/2, 17/2, \ldots, 25/2$ for A and B. In the case of a linearly polarized electric field, where $\boldsymbol{\epsilon}\times\boldsymbol{\epsilon}^* = 0$ and only transitions with $M_A = M_B = M$ are allowed, we can write

$$\Delta\nu_{BA} = -\frac{1}{2}\left(\boldsymbol{\alpha}_B^{(0)} - \boldsymbol{\alpha}_A^{(0)}\right)E^2 - \frac{1}{2}\left(\boldsymbol{\alpha}_B^{(2)} - \boldsymbol{\alpha}_A^{(2)}\right)\frac{3M^2 - F(F+1)}{F(2F-1)}E^2. \tag{5.4}$$

The radio-frequency (rf) spectroscopy of levels A and B is performed with an electric field that is nearly resonant with the $B \to A$ transition. We will assume that the energy splitting between states A and B is much smaller than the energy splitting between this nearly degenerate pair of states and all other states. With this assumption we distinguish between two contributions to the differential polarizabilities in Eq. (5.4): the *resonant* electric-dipole interaction between states A and B and the *off-resonant* electric-dipole interaction of states A and B with all other states.

[1]Note that there are different conventions used in the literature for the polarizability. In this work we use the rms-electric field to maintain consistency with the definition of dc polarizabilities.

The resonant contribution to the differential polarizability is frequency odd with respect to detuning from resonance, and for a perfectly resonant electric field it is a negligible contribution to ac-Stark shifts, neglecting the Bloch-Siegert shift [55], which is related to the 'counter-rotating' frequency component of the oscillating electric field [42].

The off-resonant contribution to the differential polarizability, however, will be approximately constant in this frequency regime and can lead to systematic errors in the rf spectroscopy of transitions between A and B. We make this distinction explicit by writing Eq. (5.4) as

$$\Delta\nu_{BA} = \|d_{BA}\|^2 \frac{|\langle FM10|FM\rangle|^2}{2F+1} f\left(\nu_{BA},\nu\right) E^2 - \frac{1}{2}\left(\overline{\boldsymbol{\alpha}}^{(0)}_{BA} + \overline{\boldsymbol{\alpha}}^{(2)}_{BA}\frac{3M^2-F(F+1)}{F(2F-1)}\right)E^2, \quad (5.5)$$

where $\overline{\boldsymbol{\alpha}}^{(0)}_{BA}$ and $\overline{\boldsymbol{\alpha}}^{(2)}_{BA}$ are the differential scalar and tensor polarizabilities that include only the off-resonant contributions, $\|d_{BA}\|$ is the reduced dipole matrix element between states A and B, and

$$f\left(\nu_{BA},\nu\right) = \mathrm{Re}\left[\frac{1}{\nu_{BA}-\nu-i\frac{\Gamma_{AB}}{2\cdot 2\pi}} + \frac{1}{\nu_{BA}+\nu+i\frac{\Gamma_{AB}}{2\cdot 2\pi}}\right] \quad (5.6)$$

contains the dependence of the resonant differential polarizability on the electric field frequency, ν. The quantity Γ_{BA} is determined by the radiative lifetimes of states A and B as well as transit effects; in our setup it is empirically determined to ≈ 45 kHz.

To facilitate further discussion we introduce the compact notation

$$\begin{aligned} d^2_{BA} &:= \|d_{BA}\|^2 \frac{|\langle FM10|FM\rangle|^2}{2F+1}, \\ \overline{\boldsymbol{\alpha}}_{BA} &:= \overline{\boldsymbol{\alpha}}^{(0)}_{BA} + \overline{\boldsymbol{\alpha}}^{(2)}_{BA}\frac{3M^2-F(F+1)}{F(2F-1)}. \end{aligned} \quad (5.7)$$

This allows us to rewrite Eq. (5.5) as

$$\Delta\nu_{BA} = d^2_{BA} f\left(\nu_{BA},\nu\right) E^2 - \frac{1}{2}\overline{\boldsymbol{\alpha}}_{BA} E^2, \quad (5.8)$$

where the dependence on M is implicit, and where d_{BA} is the dipole matrix element, and $\overline{\boldsymbol{\alpha}}_{BA}$ is the total differential polarizability for only the off-resonant contributions.

The reduced dipole matrix element was previously measured in Ref. [54]. We repeat measurements of $\|d_{BA}\|$ to calibrate the electric field amplitude in our experiment. This calibration is used to determine the total off-resonant differential polarizabilities of states A and B from ac-Stark shifts of the transition frequency. The off-resonant scalar and tensor differential polarizabilities are distinguished by repeating this measurement for several individual Zeeman transitions.

5.3 Measurements

Zeeman structure of the transition

To determine $\overline{\boldsymbol{\alpha}}_{BA}$ unambiguously we apply a magnetic field of sufficient strength to fully resolve the Zeeman structure of the transition. This enables us to measure Stark shifts of individual Zeeman transition between states A and B. The quantization axis is chosen to coincide with the linear polarizations of the applied electric field, such that only $M_B = M_A$, $\Delta M = 0$ transitions are observed. The change in the transition frequency due to the magnetic field is given by

$$\nu_Z(M) = M \cdot \mu_B/h \cdot g_{BA} \cdot B \approx M \cdot 240\ [\mathrm{Hz/mG}] \cdot B[\mathrm{mG}],$$

where $\nu_Z(M)$ is the differential Zeeman shift of the magnetic sublevel M in the transition $B \to A$, μ_B is the Bohr magneton, $g_{BA} = g_\mathrm{B} - g_\mathrm{A} = 0.157$ is the difference in g-factors for the states A and B [50], and B the field strength of the applied magnetic field.

Suppressing magnetic-field instabilities

Over the course of a typical measurement (≈ 20 min) at constant temperature the magnetic field drifts by ≈ 0.03 mG, leading to drifts of ≈ 60 Hz for the measured transition frequency between the $M = 10$ sublevels. As states A and B have the same total angular momentum F, the magnetic field insensitive $M_\mathrm{B} = 0 \to M_\mathrm{A} = 0$ transition is forbidden [42]. We choose to suppress the magnetic field related uncertainties by measuring the transition frequencies of the $+M$ and $-M$ sublevels nearly simultaneously.

The frequency $\nu_{BA}(M)$ for the $B \to A$ transition between sublevels M under the influence of a magnetic and an electric field is given by:

$$\nu_{BA}(M) = \nu_{BA} + \nu_Z(M) - \frac{1}{2}\overline{\boldsymbol{\alpha}}_{AB}E^2 + d_{BA}^2 f\left[\nu_{BA} + \nu_Z(M), \nu\right] E^2. \tag{5.9}$$

Under our assumption that the separation between states A and B is much smaller than their separation from any other states, $\overline{\boldsymbol{\alpha}}_{AB}$ should also be magnetic field insensitive.

The Zeeman shift $\nu_Z(M)$ changes sign with respect to the sign of M, while the Stark shift does not, thus our measured quantity is the magnetic field insensitive average of the $\pm M$ Zeeman transitions:

$$\begin{aligned}\bar{\nu}_{BA} &= \frac{1}{2}\left[\nu_{BA}(+M) + \nu_{BA}(-M)\right] \\ &= \nu_{BA} - \frac{1}{2}\overline{\boldsymbol{\alpha}}_{BA}E^2 + \\ &\quad \frac{1}{2}d_{BA}^2\big\{f\left[\nu_{BA} - \nu_Z(M), \nu\right] + f\left[\nu_{BA} + \nu_Z(M), \nu\right]\big\}E^2.\end{aligned} \tag{5.10}$$

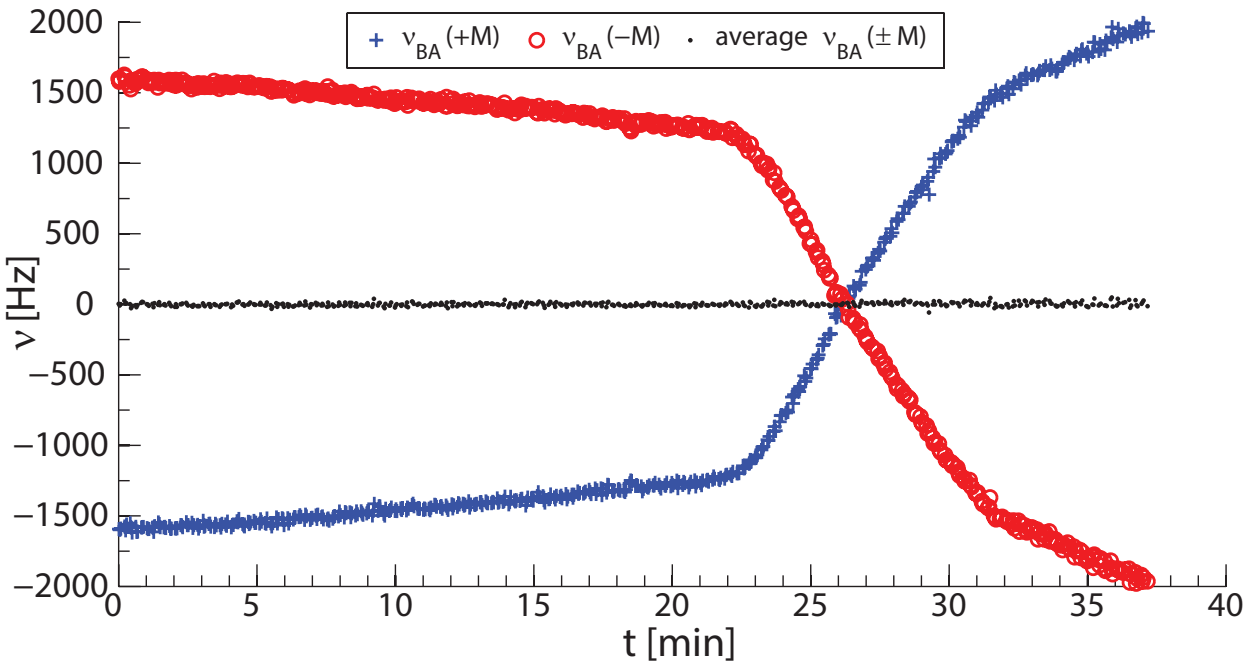

Figure 5.1: Frequency of the $M = +10$, $M = -10$ and the $M = \pm 10$ average Zeeman transition, offset for presentation. Over the course of this measurement the individual Zeeman transitions changed by ≈ 3500 Hz while the $\pm M$ average changed by ≈ 8 Hz, demonstrating a suppression of ≈ 450 in this case. The actual separation between the $M = +10$ and $M = -10$ transition is $\approx 3 \times 10^6$ Hz. These data were taken while the interaction region was cooled toward liquid nitrogen temperatures. The relatively large drift in magnetic field of > 1 mG is believed to be due to thermoelectric currents induced by temperature gradients between dissimilar metals.

Two effects may make the cancellation of magnetic fields imperfect. The $-M$ and $+M$ transitions are measured sequentially, ≈ 1 s apart from each other. In a magnetic field drifting at rate $\dot{B}$ [mG/s] the average $\pm M$ frequency will have a systematic shift of $(1/2) \cdot 220 \cdot M\dot{B}\Delta t$ Hz, where Δt is the measurement interval in seconds.

Second, the Zeeman shift in the two-state term cancels incompletely due to the form of $f(\nu_{BA}, \nu)$, Eq. (5.6). This impairment is negligible in practice as long as the difference between the Zeeman shifted transition frequencies, $\nu_{BA}(\pm M)$, and the electric field frequency ν is much larger in magnitude than the change in the Zeeman shift due to varying magnetic fields (typically) $|\nu_{BA}(\pm M) - \nu| \geq 10^6$ Hz vs $\delta\nu_z(M) < 4 \times 10^4$ Hz).

We find empirically that changes of the Zeeman shifts are suppressed by nearly three orders of magnitude. An example of the cancellation can be seen in Fig. 5.1.

5.4 Measurement Procedure

The transition frequencies are measured by scanning the frequency of a frequency-modulated electric field, the 'probe' field, near resonance. We perform lock-in detection of the 564-nm fluorescence light emitted by Dy atoms during the final decay step of level A to the ground state with a photomultiplier tube and lock-in amplifier. Near resonance, the lock-in signals at the first and second harmonic of the 10-kHz modulation frequency are approximated by a linear function that crosses zero on resonance, and a constant function, respectively. The quantity from which we determine the resonance frequency is the ratio of these signals, as it is insensitive to changes in signal size that may arise from fluctuations in the density of excited state atoms. For small detunings this ratio is given by

$$R(\nu) = \mathcal{M}\left(\nu - \nu_{BA}\right), \tag{5.11}$$

where ν is the probe-field frequency and $\mathcal{M}$ is the empirically determined slope (Fig 5.2).

We measure R repeatedly for three probe-field frequencies at intervals of 200 Hz near the expected transition for each Zeeman transition (Fig. 5.2). The slope $\mathcal{M}$ is determined from the linear least squares fit to the mean signal ratios. With the slope S, each measurement of R is converted into a transition frequency via the relation

$$\omega_{BA} = \omega_{\mathrm{rf}} - \frac{R(\omega_{\mathrm{rf}})}{\mathcal{M}}. \tag{5.12}$$

5.5 Experimental Setup

The rf spectroscopy is performed with the atomic-beam apparatus depicted in Fig. 5.3. A thermal beam of Dy atoms is emitted by an effusive oven, operated at ≈1400 K. Two vacuum chokes are used to facilitate a pressure differential from 10^{-7} to 10^{-9} torr between the oven and interaction regions. Excitation of atomic states is performed with 833-nm and 669-nm light with an adiabatic-passage population technique that uses diverging laser beams matched to the transverse divergence of the atomic-beam [62]. The 669-nm light is generated by a Coherent CR-699 dye laser using dicyanomethylene (DCM) dye and pumped by a Coherent Innova-300 argon-ion laser. Two sources have been used to generate the 833-nm light. One source is a custom built master-oscillator power-amplifier system, consisting of a Littrow-configuration extended-cavity diode laser (ECDL) whose output is amplified with a tapered amplifier (TA). The other source is a Coherent CR-899 Ti:Sapphire laser pumped by a Coherent Innova-400 argon-ion laser; typical powers are 150 mW (669 nm) and 250 mW (833 nm).

The laser and rf interaction regions are surrounded by two layers of magnetic shielding that suppress external fields to below 0.5 mG. Three pairs of coils within the shielded volume provide additional control over magnetic fields in all directions.

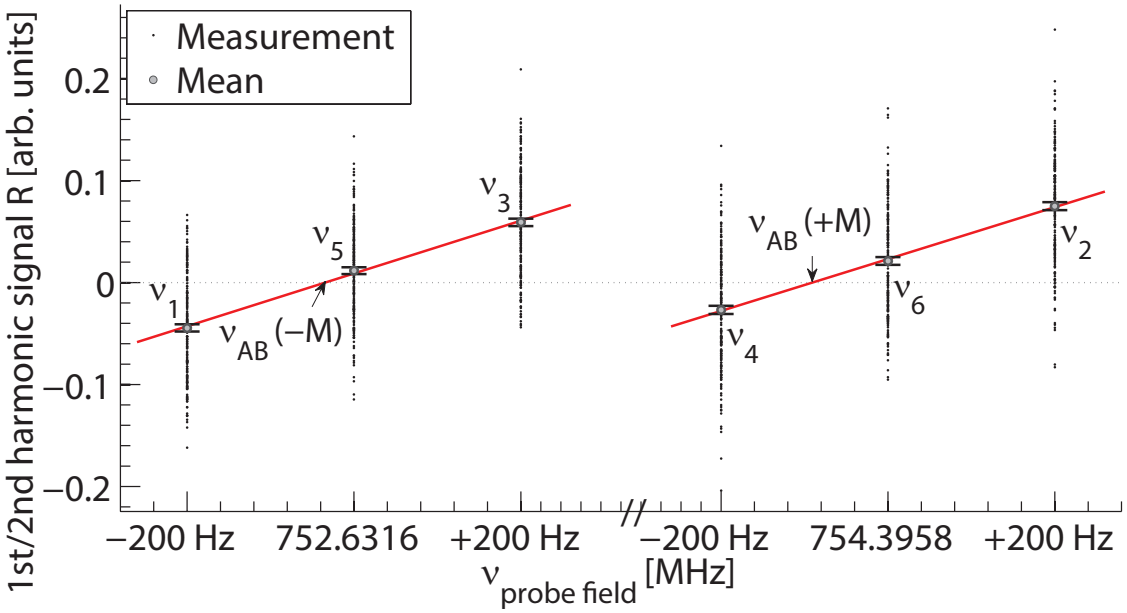

Figure 5.2: The Zeeman structure of the $B \rightarrow A$ transition is resolved with a 550-mG field. We measure the ratio R of the 564-nm fluorescence signals at the 1st and 2nd harmonic to the frequency modulated probe field in the order $i = 1, \cdots, 6$ at the frequencies ν_i, to approximate simultaneous measurement of the $\nu_{BA}(-M)$ and $\nu_{BA}(+M)$.

Two rf-electric fields, a 'probe' and a 'Stark' field, are provided by two signal generators with separate amplifiers (Fig. 5.4). These amplified rf fields are combined and fed to the interaction region, incorporating a rectangular electrode that is surrounded on all sides by a grounded box. This nested rectangular configuration supports a transverse electromagnetic mode and provides a homogeneous field up to 1 GHz. The 'surfaces' of the electrodes and box are defined by a series of parallel gold-plated 0.002-in Be-Cu wires stretched across gold-plated copper frames at 2-mm intervals. This electrode design is effectively transparent to atoms and photons, while effectively solid for the wavelength range we operate in (> 30 cm). A partial view of the electrode frames, without wires, can be seen in Fig. 5.3.

Atoms that are excited from B to A decay back to the ground state, with a lifetime of ≈ 8 μs, via several channels. In one of these channels the final step includes the emission of a 564-nm photon. Three concave mirrors made from polished aluminum focus these 564-nm photons into a Pyrex lightpipe, which guides the light into a photomultiplier tube (PMT). The PMT signal is processed with a digital lock-in amplifier.

The magnetic field coils, rf electrodes, and light-collection mirrors constitute a single assembly. This assembly is clamped to two copper rods inside the vacuum chamber. The copper rods pass to the exterior of the vacuum setup, thermally and electrically isolated from the chamber by ceramic feedthroughs. These copper 'cold fingers' allow the rf electrodes and surrounding light-collection mirrors to be heated or cooled without introducing heating

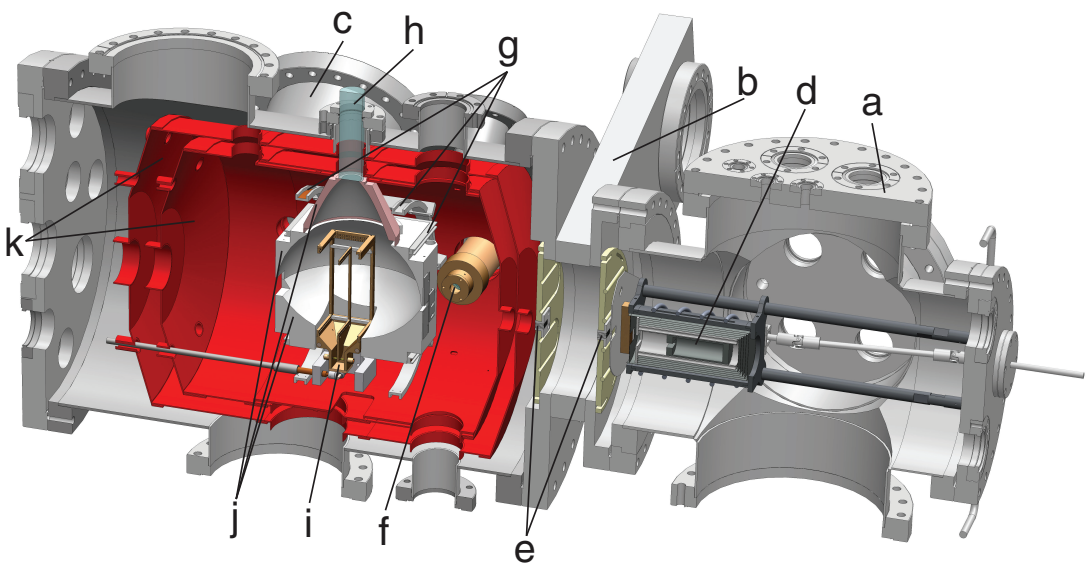

Figure 5.3: Section view of the atomic beam apparatus.
a) oven chamber; b) gate valve; c) interaction-region chamber; d) Dy oven; e) vacuum chokes; f) laser access/in-vacuum polarizer; g) magnetic coils; h) lightpipe; i) rf electrodes; j) light-collection mirrors; k) two-layer magnetic shielding

elements or cryogens into the vacuum environment. The temperatures of the light-collection assembly, oven, and vacuum chamber are continuously monitored with thermocouples.

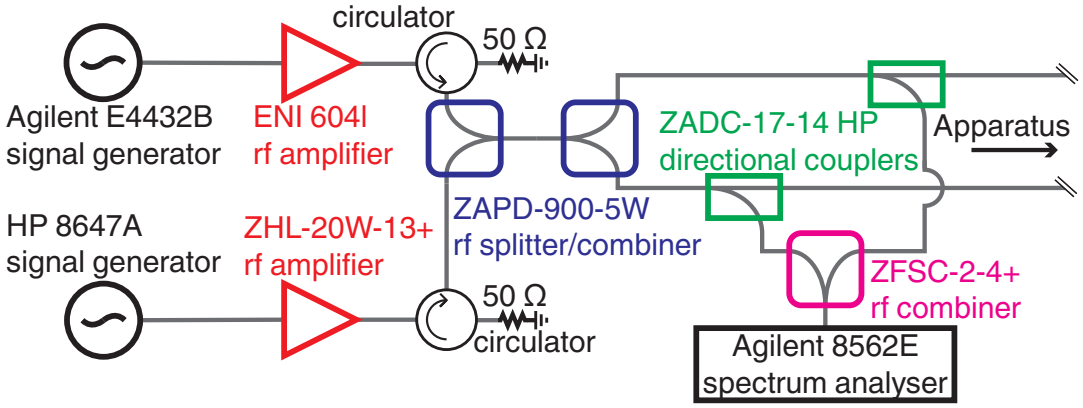

Figure 5.4: Radio-frequency setup for the measurement of ac-Stark shifts.

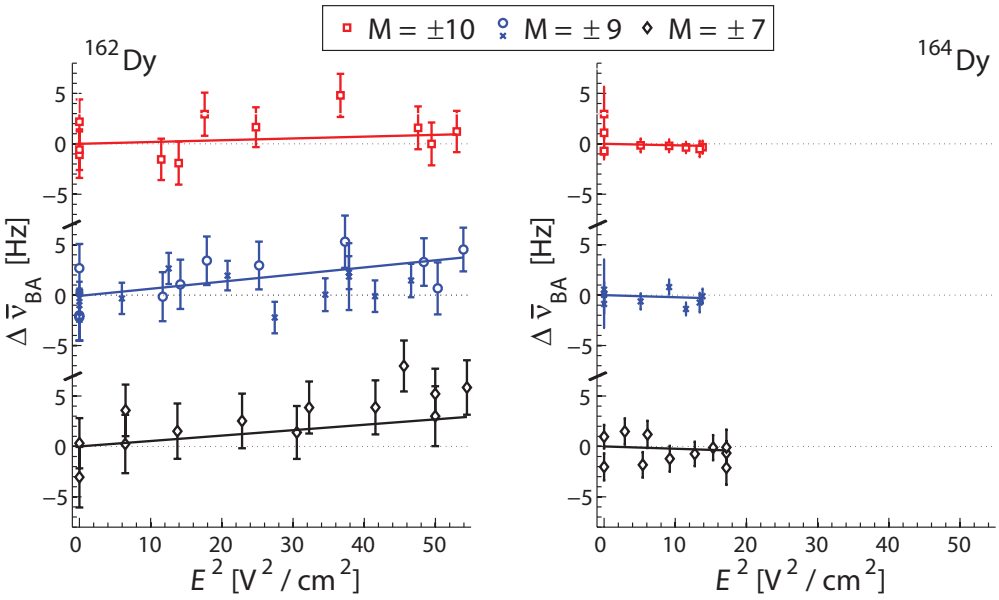

Figure 5.5: The mean ac-Stark shift of the $\pm M$ transitions in ^{162}Dy and ^{164}Dy, as a function of squared electric-field strength E^2. Lines of best fit are obtained from least-squares fit of Eq. (5.14) to the data. Measurements for different Zeeman transitions are offset from each other for display purposes.

5.6 Results - ac-Stark shift

We determine the differential off-resonant polarizability, $\overline{\boldsymbol{\alpha}}_{AB}$, from the average ac-Stark shift of the $\pm M$ transition frequencies,$\bar{\nu}_{\mathrm{BA}}$, by applying a second, unmodulated oscillatory electric field, ν_S, referred to as the 'Stark field.' We measure the Stark shifts as both a function of Stark-field amplitude (Fig. 5.5) and Stark-field frequency (Fig. 5.6).

For measurements as a function of Stark-field amplitude, the shift of the difference in $\pm M$ transition frequencies is used to calibrate the electric field according to

$$\begin{aligned}\Delta\left[\nu_{BA}(+M)-\nu_{BA}(-M)\right] =& d_{BA}^2\big\{f\left[\nu_{BA}+\nu_Z(M),\nu_S\right]- \\ & f\left[\nu_{BA}-\nu_Z(M),\nu_S\right]\big\}E^2,\end{aligned} \tag{5.13}$$

where in calculating d_{BA} we use $\|d_{BA}\|^2 \cong 19.2^2$ V^2/cm^2 [54], and the Zeeman transition frequencies, $\nu_{BA} \pm \nu_Z(M)$, are known from measurements at $E^2 = 0$. Typical mean-squared Stark-field amplitudes range from 0 to 15 V^2/cm^2 for ^{164}Dy and 0 to 50 V^2/cm^2 for ^{162}Dy. The large difference in maximum value is hypothesized to be due to a substantial frequency dependence of the impedance mismatch between the rf transmission line and the electric field plates. The shift of $\bar{\nu}_{BA}$ is given by

$$\Delta\bar{\nu}_{BA} = \left(\frac{d_{BA}^2}{2}\left\{f\left[\nu_{BA}-\nu_Z(M),\nu_S\right]+f\left[\nu_{BA}+\nu_Z(M),\nu_S\right]\right\}-\frac{\overline{\boldsymbol{\alpha}}_{AB}}{2}\right)E^2. \tag{5.14}$$

The frequency of the Stark field is chosen such that the two-state shift cancels in the average shift of $\bar{\nu}_{BA}$ (neglecting the Bloch-Siegert shift discussed below). This occurs at the frequency $\nu_S = \bar{\nu}_{BA}|_{E=0}$ (around ≈ 753.5 MHz, see Fig. 5.6). The remaining shift is given only by the differential off-resonant polarizability and the Bloch-Siegert shift, which is on the order of $\lesssim 30$ mHz and accounted for in the analysis. These data and the resulting least-squares fits to Eq. (5.14) are shown in Fig. 5.5.

An error in setting the Stark-field frequency would systematically alter the measured total differential polarizability through imperfect cancellation of the two-state shift. We minimize the deviation of the Stark-field frequency by referencing the probe-field and Stark-field generators to a Cs frequency standard. This ensures a deviation from the expected frequency that is less than 2 Hz, reducing the systematic uncertainty in the total differential polarizability to < 0.2 mHz cm^2/V^2. This is negligible compared to the statistical uncertainty, which is on the order of 100 mHz cm^2/V^2.

For the measurements as a function of Stark-field frequency, we again make use of the fact that the shift of the average $\pm M$ transition frequencies is given by Eq. (5.14). The differential off-resonant polarizability, $\overline{\boldsymbol{\alpha}}_{AB}$, and the mean-squared Stark field amplitude, E^2, are free parameters of the least-square fits of Eq. (5.14) to measured shifts of the $M = 7$, 8, and 9 transitions in ^{164}Dy, as shown in Fig. 5.6.

The total differential off-resonant polarizabilities are determined for the $M = 7$, 8, 9, and 10 transitions in ^{164}Dy and ^{162}Dy, as shown in Fig. 5.5 and Fig. 5.6, and fit via least-squares

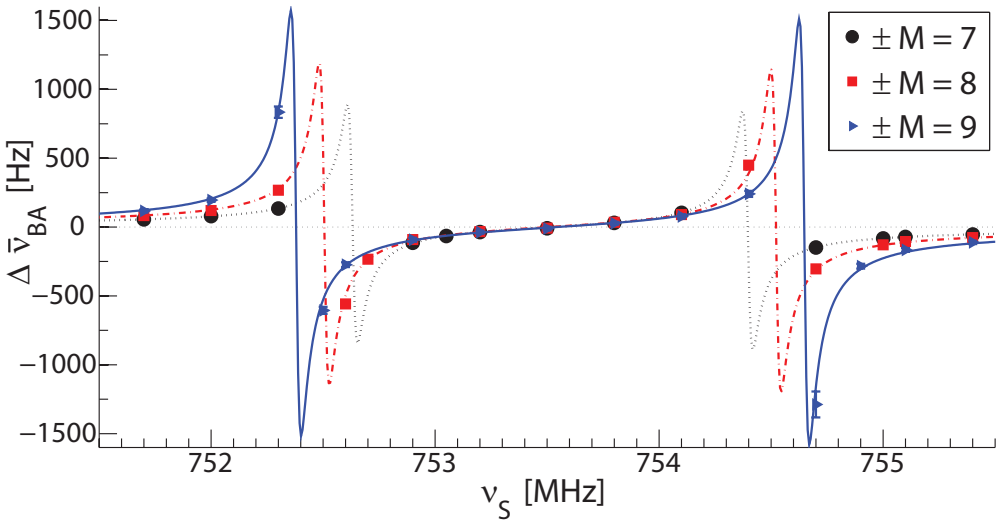

Figure 5.6: Average ac-Stark shift of the $\pm M$ sublevels, as a function of the Stark-field frequency ν_S. The zero crossings at the centers of the dispersive resonances indicate the approximate location of the individual Zeeman transition frequencies. The mean-squared amplitude of the Stark field was ≈ 9 V^2/cm^2.

according to the relationship

$$\overline{\boldsymbol{\alpha}}_{BA} = \overline{\boldsymbol{\alpha}}^{(0)}_{BA} + \overline{\boldsymbol{\alpha}}^{(2)}_{BA} \frac{3M^2 - F(F+1)}{F(2F-1)}. \tag{5.15}$$

The differential scalar and tensor off-resonant polarizabilities are found to be

$$\begin{aligned} \overline{\boldsymbol{\alpha}}^{(0)}_{BA} &= \quad 180\ (45)_{\text{stat}}\,(8)_{\text{sys}}\ \text{mHz cm}^2/\text{V}^2, \\ \overline{\boldsymbol{\alpha}}^{(2)}_{BA} &= -163\ (65)_{\text{stat}}\,(5)_{\text{sys}}\ \text{mHz cm}^2/\text{V}^2. \end{aligned} \tag{5.16}$$

Assuming that the differential polarizability arises due to the electric-dipole interaction of state A or B with only one other state, the ratio $\overline{\boldsymbol{\alpha}}^{(2)}_{BA}/\overline{\boldsymbol{\alpha}}^{(0)}_{BA} = -0.9(4)$ is consistent with a total angular momentum of $J = 9$ or $J = 11$ for the partner state [99]. The closest documented state is the odd-parity, $4f^9 5d^2 6s\, J = 9$ state at 19,558 cm^{-1} [50]. The energy of this state relative to the energy of state A (19,797 cm^{-1}) is consistent with the sign of the scalar polarizability. The magnitude of the scalar polarizability would require a reduced dipole-matrix element between this state and state A of $\|d\| = 6.9(0.9)\ \text{ea}_0$.

We also cannot rule out the existence of close lying states not listed in the spectroscopic databases. Studying Raman transitions within the Zeeman manifold of either state A or B would allow their individual contributions to the differential polarizability to be determined and will provide more information about the off-resonant states.

If the off-resonant differential polarizabilities are due to the interaction with states that are far removed, like the one at 19,558 cm^{-1}, the polarizabilities presented in Eq. (5.16) are valid into the DC frequency range. Using the value for $\|d_{BA}\|$ from Ref. [54] the two-state DC differential polarizabilities are given by [97]:

$$\begin{aligned} \boldsymbol{\alpha}^{(0)}_{BA} - \overline{\boldsymbol{\alpha}}^{(0)}_{BA} &= \begin{cases} 31\ (4)\ \text{mHz}\frac{\text{cm}^2}{\text{V}^2} & {}^{164}\text{Dy} \\ 100\ (14)\ \text{mHz}\frac{\text{cm}^2}{\text{V}^2} & {}^{162}\text{Dy} \end{cases}, \\ \boldsymbol{\alpha}^{(2)}_{BA} - \overline{\boldsymbol{\alpha}}^{(2)}_{BA} &= \begin{cases} 172\ (24)\ \text{mHz}\frac{\text{cm}^2}{\text{V}^2} & {}^{162}\text{Dy} \\ 54\ (8)\ \text{mHz}\frac{\text{cm}^2}{\text{V}^2} & {}^{164}\text{Dy} \end{cases}. \end{aligned} \tag{5.17}$$

In this case the off-resonant polarizabilities add a significant contribution to the total two-state DC polarizabilities of states A and B.

5.7 Blackbody radiation

The electric field of blackbody radiation (BBR) from the environment can cause ac-Stark shifts of atomic energy levels [100]. The mean-squared electric-field amplitude, in a frequency interval $d\nu$, of blackbody radiation in a vacuum surrounded by an enclosure of uniform temperature T is given by Planck's law as [101]

$$E^2_{\text{BBR}}(T,\nu)d\nu = 32\pi^2 \frac{h\nu^3}{c^3} \frac{300^2}{e^{\frac{h\nu}{kT}} - 1} d\nu \quad \text{V}^2/\text{cm}^2, \tag{5.18}$$

where k is the Boltzmann constant, c is the speed of light, T is the absolute temperature in Kelvin, and all the quantities on the right-hand side are assumed to be in the centimeter-gram-second (cgs) units; the factor of 300 converts the expression to units of $\mathrm{V}^2/\mathrm{cm}^2$.

Blackbody radiation is unpolarized and isotropic with no preferred axis. The ac-Stark shift of the $B \to A$ transition is therefore given by the differential scalar polarizability and the integral over all frequencies ν,

$$\Delta\nu_{BA}(T) = -\frac{1}{2}\int_0^\infty E^2_{\mathrm{BBR}}(T,\nu)\left(\boldsymbol{\alpha}^{(0)}_B - \boldsymbol{\alpha}^{(0)}_A\right)d\nu. \tag{5.19}$$

We again differentiate between the BBR related shift due to the interaction between A and B and the contribution from off-resonant states by writing

$$\Delta\nu_{BA}(T) = \int_0^\infty E^2_{\mathrm{BBR}}(T,\nu)\left[d^2_{BA} f\left(\nu_{BA},\nu\right) - \frac{1}{2}\overline{\boldsymbol{\alpha}}^{(0)}_{BA}\right]d\nu. \tag{5.20}$$

The separation between states A and B is small compared to characteristic frequencies of BBR at 300 K. From the value for the dipole matrix element presented in Ref. [54], we can calculate the BBR radiation shift due to d^2_{BA} around 300 K to be

$$\frac{d}{dT}\int_0^\infty E^2_{\mathrm{BBR}}(T,\nu) d^2_{BA} f\left(\nu_{BA},\nu\right)d\nu|_{T=300\mathrm{K}} < 10^{-10}\frac{\mathrm{Hz}}{K}, \tag{5.21}$$

which is negligibly small. The dense level structure of Dy, however, makes it probable that energy levels with strong electric-dipole coupling to state A or B exist within the thermal radiation spectrum, leading to a non-negligible BBR induced ac-Stark shift. It is important to note that the value for $\overline{\boldsymbol{\alpha}}^{(0)}_{BA}$ reported earlier in this paper is valid only for the range of frequencies where $\nu < 1$ GHz. The value of $\overline{\boldsymbol{\alpha}}^{(0)}_{BA}$ in Eq. (5.20) is a frequency dependent quantity [97] with unknown behavior in the range of BBR frequencies ($\geq$ THz).

We measure the transition frequency, ν_{BA}, as a function of temperature of the interaction region, consisting of the light-collection mirrors and electric field plates as shown in Fig. 5.3. These measurements were performed at two settings of the magnetic field: with a ≈ 650 mG magnetic field to resolve the Zeeman transitions (Fig 5.8), and at zero magnetic field with the Zeeman structure unresolved (Fig 5.7). These measurements should produce the same measured shifts due to the absence of vector or tensor terms in Eq. (5.19).

The functional dependence of BBR induced shifts on temperature is generally unknown due to the temperature dependence of the BBR spectrum and the frequency dependence of $\overline{\boldsymbol{\alpha}}^{(0)}_{BA}$. A common assumption, however, is that the energy splitting between A or B and other states is much larger than the characteristic energy of the BBR spectrum. In this approximation, the off-resonant scalar polarizability in Eq. (5.20) is the same as that measured in Sec. 5.6 and we can write

$$\Delta\nu_{BA} = -\frac{1}{2}\overline{\boldsymbol{\alpha}}^{(0)}_{BA}\left(\frac{T}{300\ \mathrm{K}}\right)^4 8.32^2\,\mathrm{V}^2/\mathrm{cm}^2. \tag{5.22}$$

Here 8.32 $\mathrm{V}^2/\mathrm{cm}^2$ is the rms value of room temperature BBR.

5.8 Results - Blackbody radiation shifts

The transition frequency ν_{BA} for ^{164}Dy and ^{162}Dy was measured for environment temperatures ranging from 120 K and 350 K.

At zero magnetic field, with unresolved Zeeman structure, the temperature was only varied from 300 to 360 K. Results are shown in Fig. 5.7, and the measured slopes are:

$$\left.\frac{d}{dT}\nu_{BA}\right|_{300\text{K}} = \begin{cases} -34(4)\ \text{mHz/K} & ^{164}\text{Dy} \\ +29(4)\ \text{mHz/K} & ^{162}\text{Dy}. \end{cases} \tag{5.23}$$

The signs of the measured frequency shifts are expected to be opposite for these two isotopes due to the different sign of the energy splitting between A and B. The temperature range is too small to verify a T^4 dependence. Performing a linear expansion of Eq. (5.22) around 300 K we find that the linear slopes correspond to differential scalar polarizabilities:

$$\overline{\boldsymbol{\alpha}}^{(0)}_{BA} = \begin{cases} 74\,(9)\ \text{mHz cm}^2/\text{V}^2 & ^{164}\text{Dy} \\ 63\,(9)\ \text{mHz cm}^2/\text{V}^2 & ^{162}\text{Dy} \end{cases} \tag{5.24}$$

These values are on the same order as the polarizabilities measured at radio frequencies; however, these are not expected to be the same due to the possibility of many more atomic states

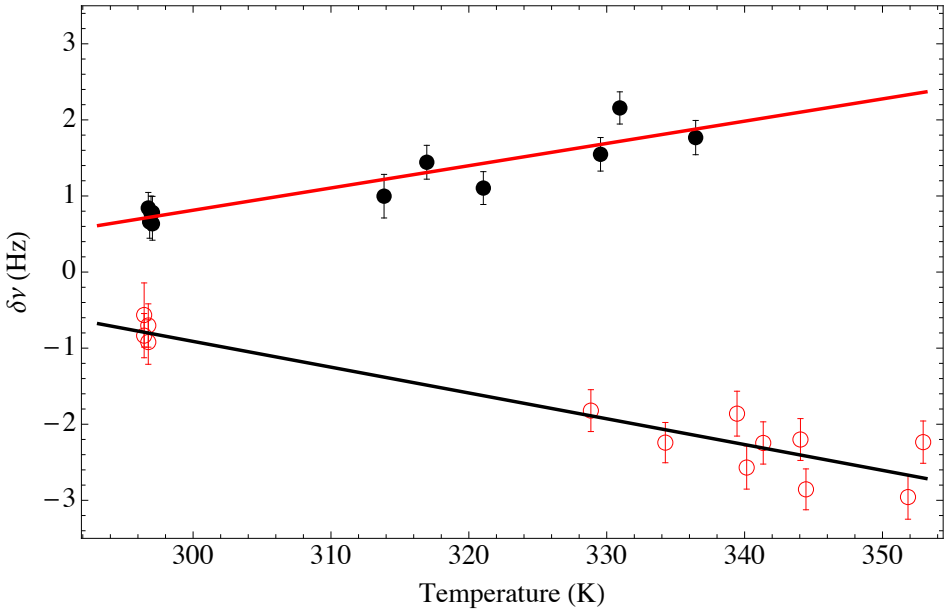

Figure 5.7: Frequency shifts of the unresolved ^{162}Dy (filled circles) and ^{164}Dy (empty circles) $B \to A$ transitions as a function of interaction region temperature. Solid lines indicate least-squares fit to the data.

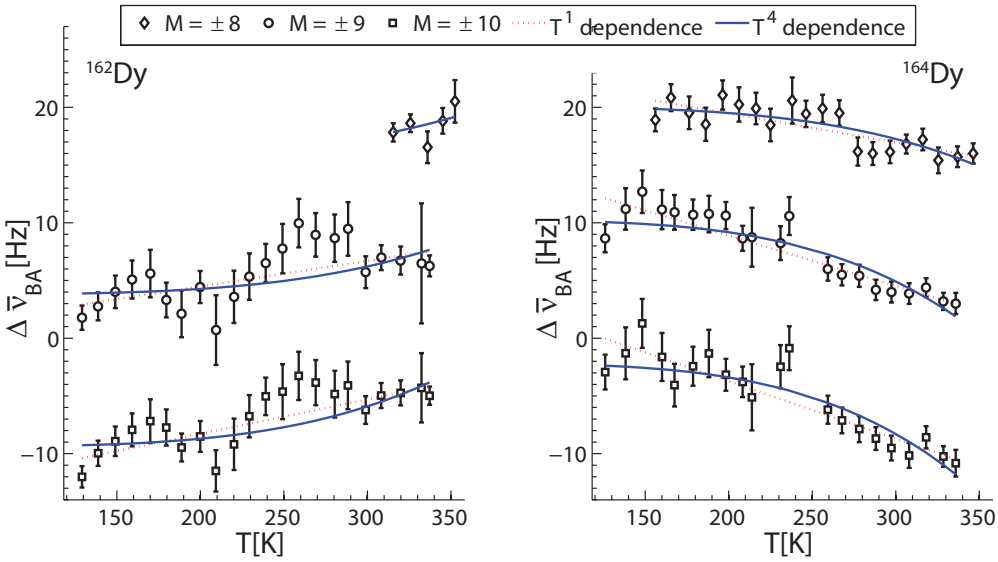

Figure 5.8: Average of the $\pm M$, $B \rightarrow A$ transition frequencies as a function of the interaction-region temperature. The $M = \pm 9$ and $M = \pm 10$ transition frequencies for both isotopes were measured in the same run. Plots for different sublevels have been offset vertically for visibility.

contributing significantly to BBR shifts. In Dy the closest neighbor state at 19,558 cm^{-1} is only 7 THz removed from A or B, compared to the 24 THz peak of the BBR spectrum at 300 K, with a full-width at half-maximum bandwidth of 27 THz.

The transition frequencies were also measured across a larger temperature interval, see Fig. 5.8. For these measurements a $\approx$ 650 mG magnetic field was applied to resolve the Zeeman structure and more effectively cancel drifting magnetic fields. The temperature of the light collection mirrors was varied from 120 K to 340 K.

The differential scalar polarizabilities obtained from a T^4 least-squares fit to the data are consistent in sign and magnitude for the two isotopes, but are not consistent within errors. These measurements appear to be influenced by systematic errors uncorrelated with BBR intensity, as evidenced by relatively large deviations from the T^4 dependence in the ^{162}Dy data that are not present in the ^{164}Dy data. One hypothesis is that large changes in the magnetic field, possibly due to thermoelectric currents generated by temperature gradients across dissimilar metals, are not completely canceled out in the $\pm M$ average frequency. These results should be considered preliminary due to the presence of this unexplained departure from the T^4 dependence in only one isotope.

5.9 Summary

We have presented measurements of the off-resonant differential polarizabilities of states A and B in ^{162}Dy and ^{164}Dy for radio-frequency electric fields, and the effect of temperature

on the transition frequency between these states in both isotopes.

Non-zero off-resonant polarizabilities could result in systematic errors in the measured value of ν_{BA}. In the experiment dedicated to constraining variation of α we are not concerned with the overall systematic error, but the *stability* of the systematic error over the course of the experiment's lifetime. The stability of each ac-Stark related systematic is discussed in order to project the systematic limits on a search for variation of α.

The probe electric field in the rf spectroscopy of the $B \to A$ transition has a typical mean-squared amplitude of $E^2 = 4.5\ \mathrm{V^2/cm^2}$. Assuming a stability of $\delta E^2 = 0.45\ \mathrm{V^2/cm^2}$, the two-state ac-Stark shift for a resonant probe field contributes a systematic frequency uncertainty of

$$\begin{aligned}\sigma_{\nu_{BA}} &= \|d_{BA}\|^2 F(\nu_{BA}, \nu_{BA}) \delta E^2 \sum_M a_M \frac{|\langle JM10|JM\rangle|^2}{2J+1} \\ &= \begin{cases} 8\ \mathrm{mHz} & {}^{162}\mathrm{Dy} \\ 2\ \mathrm{mHz} & {}^{164}\mathrm{Dy} \end{cases},\end{aligned} \tag{5.25}$$

where the sum is over the normalized signal amplitudes, a_M, of the unresolved Zeeman transitions. These amplitudes are measured with the Zeeman structure of the transition fully resolved (see Appendix B.

The systematic uncertainty arising from off-resonant ac-Stark shifts is evaluated with the maximum likelihood differential polarizabilities from Eq. (5.16):

$$\begin{aligned}\sigma_{\nu_{BA}} &= \frac{1}{2}\delta E^2 \sum_M a_M \left(\overline{\boldsymbol{\alpha}}^{(0)}_{BA} + \overline{\boldsymbol{\alpha}}^{(2)}_{BA} \frac{3M^2 - (J(J+1))}{J(2J-1)} \right) \\ &= 32\ \mathrm{mHz}.\end{aligned} \tag{5.26}$$

The temperature of the light collection mirrors was found to vary between 294 °C and 298 °C for measurements spanning over two years. Using the result of Eq. (5.23) gives an estimate of the stability of ν_{BA} due to temperature dependent effects of

$$\sigma_{\nu_{BA}} = 66\ \mathrm{mHz}. \tag{5.27}$$

Dysprosium atoms are also subject to the thermal radiation from the atomic-beam oven. The higher temperature of the oven (1400 K vs. 300 K) makes its radiation ≈ 470 times more intense. Due to the distance between the interaction region and the oven, however, the intensity of oven BBR at the rf region is reduced by a factor $\approx 10^{-4}$. The typical temperature variability of the oven of is ± 10 K, and neglecting the change in the frequency spectrum of BBR, the systematic uncertainty due to oven BBR radiation is

$$\sigma_{\nu_{BA}} = 16\ \mathrm{mHz}. \tag{5.28}$$

The four systematic uncertainties discussed are added in quadrature to evaluate the total ac-Stark related systematic uncertainty:

$$\sigma_{\nu_{BA}} = 75 \text{ mHz}. \tag{5.29}$$

For two measurements, separated by one year, of the transition frequencies ν_{BA} in each isotope this systematic uncertainty will limit the experimental sensitivity to variation of α at the level of $|\dot{\alpha}/\alpha| = 2.6 \times 10^{-17}$ yr^{-1}, which would be comparable to the present best limit [31]. The ac-Stark systematic limit can be reduced by better stabilization of the interaction region temperature and improved stability of the rf-field amplitude. Further studies of the BBR induced shifts may allow frequency measurements to be corrected for drifts of the interaction region temperature. We have also shown that the off-resonant polarizabilities contribute substantially to the differential dc-polarizability of levels A and B.

This work, in addition to helping constrain systematics uncertainties for searches of variation of α also provides additional spectroscopic information about the states A and B that can be used to test the atomic-structure calculations that are used in conjunction with these experiments [51].

6 — Conclusion

The results in this work are some of the best bounds on variation of the fine-structure constant and possible Lorentz violating effects for electrons. Both results show potential for improvement, although the systematic limitation due to electronic offsets of the constraint on varying α is unlikely to be easily addressed. The work on Lorentz violation currently shows more promise for rapid improvement. The possibility of putting the experiment on a rotating platform and acquiring constraints on $c_{\mu\nu}$ over the course of hours, rather than days or years, drastically reduces the susceptibility of the experiment to the kinds of slowly varying systematic effects believed to currently limit our results. Work is currently underway to implement this, and it should be noted that data acquired for Lorentz violation is always complementary to data constraining variation of α, assuming that rotating the experiment does not introduce new unforeseen systematic effects.

Beyond these two results, plans are in place to use the present apparatus to resume investigations into atomic parity nonconservation. The last attempted measurement of this effect in dysprosium yielded a result consistent with zero and limited by statistics [41], but was inconsistent with theoretical calculations at the time [88]. With revised calculations that still predict a non-zero effect but resolve this inconsistency [73], we expect that the improved sensitivity of the apparatus will allow us to finally determine if Dy is a viable candidate for the study of parity violation in atoms.

Bibliography

[1] G. Aad et al. "Observation of a new particle in the search for the Standard Model Higgs boson with the ATLAS detector at the LHC". In: *Physics Letters B* 716.1 (2012), pp. 1–29. DOI: 10.1016/j.physletb.2012.08.020.

[2] S. Chatrchyan et al. "Observation of a new boson at a mass of 125 GeV with the CMS experiment at the LHC". In: *Physics Letters B* 716.1 (2012), pp. 30–61. DOI: 10.1016/j.physletb.2012.08.021.

[3] Peter Higgs. "Broken Symmetries and the Masses of Gauge Bosons". In: *Physical Review Letters* 13.16 (1964), pp. 508–509. DOI: 10.1103/PhysRevLett.13.508.

[4] Claus Kiefer. "Quantum Gravity and Fundamental Constants". In: *Astrophysics, Clocks and Fundamental Constants*. Ed. by S. G. Karshenboim and E. Peik. Vol. 127. Bad Honnef, Germany: Springer, Berlin Heidelberg, 2004, pp. 115–127. DOI: 10.1007/978-3-540-40991-5_8.

[5] M Aguilar et al. "First Result from the Alpha Magnetic Spectrometer on the International Space Station: Precision Measurement of the Positron Fraction in Primary Cosmic Rays of 0.5350 GeV". In: *Physical Review Letters* 110.14 (2013), p. 141102. DOI: 10.1103/PhysRevLett.110.141102.

[6] S. Perlmutter et al. "Measurements of Ω and Λ from 42 HighRedshift Supernovae". In: *The Astrophysical Journal* 517.2 (1999), pp. 565–586. DOI: 10.1086/307221.

[7] Sean M Carroll. "Dark Energy and the Preposterous Universe". In: (2001), p. 17.

[8] P. A. M. Dirac. "The Cosmological Constants". In: *Nature* 139.3512 (1937), pp. 323–323. DOI: 10.1038/139323a0.

[9] Nima ArkaniHamed, Savas Dimopoulos, and Gia Dvali. "The hierarchy problem and new dimensions at a millimeter". In: *Physics Letters B* 429.3-4 (1998), pp. 263–272. DOI: 10.1016/S0370-2693(98)00466-3.

[10] P. A. M. Dirac. "Cosmological Models and the Large Numbers Hypothesis". In: *Proceedings of the Royal Society A: Mathematical, Physical and Engineering Sciences* 338.1615 (1974), pp. 439–446. DOI: 10.1098/rspa.1974.0095.

[11] Holger Müller et al. "Tests of Relativity by Complementary Rotating Michelson-Morley Experiments". In: *Physical Review Letters* 99.5 (2007), p. 050401. DOI: 10.1103/PhysRevLett.99.050401.

[12] Jean-Philippe Uzan. "The fundamental constants and their variation: observational and theoretical status". In: *Reviews of Modern Physics* 75.2 (2003), pp. 403–455. DOI: 10.1103/RevModPhys.75.403.

[13] Jean-Philippe Uzan. "Varying Constants, Gravitation and Cosmology". In: *Living Reviews in Relativity* 14 (2011). DOI: 10.12942/lrr-2011-2.

[14] Edward Witten. "Search for a realistic Kaluza-Klein theory". In: *Nuclear Physics B* 186.3 (1981), pp. 412–428. DOI: 10.1016/0550-3213(81)90021-3.

[15] William Marciano. "Time Variation of the Fundamental "Constants" and Kaluza-Klein Theories". In: *Physical Review Letters* 52.7 (1984), pp. 489–491. DOI: 10.1103/PhysRevLett.52.489.

[16] John Webb et al. "Search for Time Variation of the Fine Structure Constant". In: *Physical Review Letters* 82.5 (1999), pp. 884–887. DOI: 10.1103/PhysRevLett.82.884.

[17] V. A. Dzuba, V. V. Flambaum, and J. K. Webb. "Calculations of the relativistic effects in many-electron atoms and space-time variation of fundamental constants". In: *Physical Review A* 59.1 (1999), pp. 230–237. DOI: 10.1103/PhysRevA.59.230.

[18] V. A. Dzuba, V. V. Flambaum, and J. K. Webb. "Space-Time Variation of Physical Constants and Relativistic Corrections in Atoms". In: *Physical Review Letters* 82.5 (1999), pp. 888–891. DOI: 10.1103/PhysRevLett.82.888.

[19] J. K. Webb et al. "Further Evidence for Cosmological Evolution of the Fine Structure Constant". In: *Physical Review Letters* 87.9 (2001), p. 091301. DOI: 10.1103/PhysRevLett.87.091301.

[20] M. T. Murphy et al. "Possible evidence for a variable fine-structure constant from QSO absorption lines: motivations, analysis and results". In: *Monthly Notices of the Royal Astronomical Society* 327.4 (2001), pp. 1208–1222. DOI: 10.1046/j.1365-8711.2001.04840.x.

[21] M. T. Murphy, J. K. Webb, and V. V. Flambaum. "Further evidence for a variable fine-structure constant from Keck/HIRES QSO absorption spectra". In: *Monthly Notices of the Royal Astronomical Society* 345.2 (2003), pp. 609–638. DOI: 10.1046/j.1365-8711.2003.06970.x.

[22] R. Srianand et al. "Limits on the Time Variation of the Electromagnetic Fine-Structure Constant in the Low Energy Limit from Absorption Lines in the Spectra of Distant Quasars". In: *Physical Review Letters* 92.12 (2004), p. 121302. DOI: 10.1103/PhysRevLett.92.121302.

[23] H Chand et al. "Probing the cosmological variation of the fine-structure constant: Results based on VLT-UVES sample". In: *Astronomy and Astrophysics* 417 (2004), pp. 853–871. DOI: 10.1051/0004-6361.

[24] M. Murphy, J. Webb, and V. Flambaum. "Comment on Limits on the Time Variation of the Electromagnetic Fine-Structure Constant in the Low Energy Limit from Absorption Lines in the Spectra of Distant Quasars". In: *Physical Review Letters* 99.23 (2007), p. 239001. DOI: 10.1103/PhysRevLett.99.239001.

[25] R. Srianand et al. "Srianand et al. Reply:" in: *Physical Review Letters* 99.23 (2007), p. 239002. DOI: 10.1103/PhysRevLett.99.239002.

[26] R Quast, D Reimers, and SA Levshakov. "Probing the variability of the fine-structure constant with the VLT/UVES". In: *Astronomy and Astrophysics* 11 (2004). DOI: 10.1051/0004-6361.

[27] J. K. Webb et al. "Indications of a Spatial Variation of the Fine Structure Constant". In: *Physical Review Letters* 107.19 (2011), p. 191101. DOI: 10.1103/PhysRevLett.107.191101.

[28] J. C. Berengut and V. V. Flambaum. "Manifestations of a spatial variation of fundamental constants in atomic and nuclear clocks, Oklo, meteorites, and cosmological phenomena". In: *EPL (Europhysics Letters)* 97.2 (2012), p. 20006. DOI: 10.1209/0295-5075/97/20006.

[29] V. Flambaum et al. "Limits on variations of the quark masses, QCD scale, and fine structure constant". In: *Physical Review D* 69.11 (2004), p. 115006. DOI: 10.1103/PhysRevD.69.115006.

[30] V. A. Dzuba. "V^{NM} approximation for atomic calculations". In: *Physical Review A* 71.3 (2005), p. 032512. DOI: 10.1103/PhysRevA.71.032512.

[31] T. Rosenband et al. "Frequency ratio of Al+ and Hg+ single-ion optical clocks; metrology at the 17th decimal place." In: *Science (New York, N.Y.)* 319.5871 (2008), pp. 1808–12. DOI: 10.1126/science.1154622.

[32] Don Colladay and V. Alan Kostelecký. "CPT violation and the standard model". In: *Physical Review D* 55.11 (1997), pp. 6760–6774. DOI: 10.1103/PhysRevD.55.6760.

[33] D Colladay and V. Kostelecký. "Lorentz-violating extension of the standard model". In: *Physical Review D* 58.11 (1998), p. 116002. DOI: 10.1103/PhysRevD.58.116002.

[34] V. Alan Kostelecký and Stuart Samuel. "Spontaneous breaking of Lorentz symmetry in string theory". In: *Physical Review D* 39.2 (1989), pp. 683–685. DOI: 10.1103/PhysRevD.39.683.

[35] V. Alan Kostelecký and Charles Lane. "Constraints on Lorentz violation from clock-comparison experiments". In: *Physical Review D* 60.11 (1999), p. 116010. DOI: 10.1103/PhysRevD.60.116010.

[36] V. Alan Kostelecký and Neil Russell. "Data Tables for Lorentz and CPT Violation". In: January (2013), p. 59. DOI: 10.1103/RevModPhys.83.11.

[37] B. Altschul. "Limits on Lorentz Violation from Synchrotron and Inverse Compton Sources". In: *Physical Review Letters* 96.20 (2006), p. 201101. DOI: 10.1103/PhysRevLett.96.201101.

[38] B. Altschul. "Synchrotron and inverse Compton constraints on Lorentz violations for electrons". In: *Physical Review D* 74.8 (2006), p. 083003. DOI: 10.1103/PhysRevD.74.083003.

[39] Leslie Foldy and Siegfried Wouthuysen. "On the Dirac Theory of Spin 1/2 Particles and Its Non-Relativistic Limit". In: *Physical Review* 78.1 (1950), pp. 29–36. DOI: 10.1103/PhysRev.78.29.

[40] V. Alan Kostelecky and Charles D Lane. "Nonrelativistic quantum Hamiltonian for Lorentz violation". In: *Journal of Mathematical Physics* 40.12 (1999), p. 6245. DOI: 10.1063/1.533090.

[41] A.-T. Nguyen et al. "Search for parity nonconservation in atomic dysprosium". In: *Physical Review A* 56.5 (1997), pp. 3453–3463. DOI: 10.1103/PhysRevA.56.3453.

[42] D. Budker, DF Kimball, and D. DeMille. *Atomic physics: an exploration through problems and solutions*. Oxford University Press, 2004.

[43] V. Kostelecký and Matthew Mewes. "Signals for Lorentz violation in electrodynamics". In: *Physical Review D* 66.5 (2002), p. 056005. DOI: 10.1103/PhysRevD.66.056005.

[44] Holger Müller et al. "Optical cavity tests of Lorentz invariance for the electron". In: *Physical Review D* 68.11 (2003), p. 116006. DOI: 10.1103/PhysRevD.68.116006.

[45] Holger Müller. "Testing Lorentz invariance by the use of vacuum and matter filled cavity resonators". In: *Physical Review D* 71.4 (2005), p. 045004. DOI: 10.1103/PhysRevD.71.045004.

[46] W. Haxton and E. Henley. "Enhanced T-Nonconserving Nuclear Moments". In: *Physical Review Letters* 51.21 (1983), pp. 1937–1940. DOI: 10.1103/PhysRevLett.51.1937.

[47] N. Leefer et al. "Transverse laser cooling of a thermal atomic beam of dysprosium". In: *Physical Review A* 81.4 (2010), p. 043427. DOI: 10.1103/PhysRevA.81.043427.

[48] Mingwu Lu, Seo Ho Youn, and Benjamin L. Lev. "Trapping Ultracold Dysprosium: A Highly Magnetic Gas for Dipolar Physics". In: *Physical Review Letters* 104.6 (2010), p. 063001. DOI: 10.1103/PhysRevLett.104.063001.

[49] Mingwu Lu et al. "Strongly Dipolar Bose-Einstein Condensate of Dysprosium". In: *Physical Review Letters* 107.19 (2011), p. 190401. DOI: 10.1103/PhysRevLett.107.190401.

[50] A. Kramida et al. "NIST Atomic Spectra Database". In: *NIST Atomic Spectra Database (ver. 5.0)* (2012).

[51] V. A. Dzuba and V. V. Flambaum. "Relativistic corrections to transition frequencies of AgI, DyI, HoI, YbII, YbIII, AuI, and HgII and search for variation of the fine-structure constant". In: *Physical Review A* 77.1 (2008), p. 012515. DOI: 10.1103/PhysRevA.77.012515.

[52] Michael a. Hohensee et al. "Equivalence Principle and Gravitational Redshift". In: *Physical Review Letters* 106.15 (2011), p. 151102. DOI: 10.1103/PhysRevLett.106.151102.

[53] S. Herrmann et al. "Rotating optical cavity experiment testing Lorentz invariance at the 10-17 level". In: *Physical Review D* 80.10 (2009), p. 105011. DOI: 10.1103/PhysRevD.80.105011.

[54] Dmitry Budker et al. "Experimental investigation of excited states in atomic dysprosium". In: *Physical Review A* 50.1 (1994), pp. 132–143. DOI: 10.1103/PhysRevA.50.132.

[55] A.-T. Nguyen et al. "Towards a sensitive search for variation of the fine-structure constant using radio-frequency E1 transitions in atomic dysprosium". In: *Physical Review A* 69.2 (2004), p. 022105. DOI: 10.1103/PhysRevA.69.022105.

[56] A. Cingöz et al. "Limit on the Temporal Variation of the Fine-Structure Constant Using Atomic Dysprosium". In: *Physical Review Letters* 98.4 (2007), p. 040801. DOI: 10.1103/PhysRevLett.98.040801.

[57] S. J. Ferrell et al. "Investigation of the gravitational-potential dependence of the fine-structure constant using atomic dysprosium". In: *Physical Review A* 76.6 (2007), p. 062104. DOI: 10.1103/PhysRevA.76.062104.

[58] A. Cingöz et al. "A laboratory search for variation of the fine-structure constant using atomic dysprosium". In: *The European Physical Journal Special Topics* 163.1 (2008), pp. 71–88. DOI: 10.1140/epjst/e2008-00810-0.

[59] N. Leefer et al. "Variation of the Fine-Structure Constant and Laser Cooling of Atomic Dysprosium". In: *Proceddings of the 7th Symposium: Frequency Standards and Metrology*. Ed. by Lute Maleki. Asilomar: World Scientific, 2008, pp. 34–43.

[60] A.-T. Nguyen. "A Search for Temporal Variation of the Fine-Structure Constant in Atomic Dysprosium". PhD thesis. University of California, Berkeley, 2005.

[61] A. Cingöz. "A Laboratory Test of Einstein's Equivalence Principle in Atomic Dysprosium: Search for Temporal and Gravitational Variation of the Fine-Structure Constant". PhD thesis. University of California, Berkeley, 2009.

[62] A.-T. Nguyen et al. "Efficient population transfer in a multilevel system using diverging laser beams". In: *Physical Review A* 63.1 (2000), p. 013406. DOI: 10.1103/PhysRevA.63.013406.

[63] Jürgen Müller and Liliane Biskupek. "Variations of the gravitational constant from lunar laser ranging data". In: *Classical and Quantum Gravity* 24.17 (2007), pp. 4533–4538. DOI: 10.1088/0264-9381/24/17/017.

[64] J. Guéna et al. "Improved Tests of Local Position Invariance Using ˆ{87}Rb and ˆ{133}Cs Fountains". In: *Physical Review Letters* 109.8 (2012), p. 080801. DOI: 10.1103/PhysRevLett.109.080801.

[65] Ekkehard Peik. "Fundamental constants and units and the search for temporal variations". In: *Nuclear Physics B - Proceedings Supplements* 203-204 (2010), pp. 18–32. DOI: 10.1016/j.nuclphysbps.2010.08.003.

[66] M. E. Tobar et al. "Testing local Lorentz and position invariance and variation of fundamental constants by searching the derivative of the comparison frequency between a cryogenic sapphire oscillator and hydrogen maser". In: *Physical Review D* 81.2 (2010), p. 022003. DOI: 10.1103/PhysRevD.81.022003.

[67] S. Blatt et al. "New Limits on Coupling of Fundamental Constants to Gravity Using Sr87 Optical Lattice Clocks". In: *Physical Review Letters* 100.14 (2008), p. 140801. DOI: 10.1103/PhysRevLett.100.140801.

[68] T. Fortier et al. "Precision Atomic Spectroscopy for Improved Limits on Variation of the Fine Structure Constant and Local Position Invariance". In: *Physical Review Letters* 98.7 (2007), p. 070801. DOI: 10.1103/PhysRevLett.98.070801.

[69] M Fischer et al. "New Limits on the Drift of Fundamental Constants from Laboratory Measurements". In: *Physical Review Letters* 92.23 (2004), p. 230802. DOI: 10.1103/PhysRevLett.92.230802.

[70] E. Peik et al. "Limit on the Present Temporal Variation of the Fine Structure Constant". In: *Physical Review Letters* 93.17 (2004), pp. 15–18. DOI: 10.1103/PhysRevLett.93.170801.

[71] Adrian J. de Nijs et al. "UV-frequency metrology on CO (aˆ{3}Π): Isotope effects and sensitivity to a variation of the proton-to-electron mass ratio". In: *Physical Review A* 84.5 (2011), p. 052509. DOI: 10.1103/PhysRevA.84.052509.

[72] T. Dinh et al. "Sensitivity of hyperfine structure to nuclear radius and quark mass variation". In: *Physical Review A* 79.5 (2009), p. 054102. DOI: 10.1103/PhysRevA.79.054102.

[73] V. A. Dzuba and V. V. Flambaum. "Theoretical study of some experimentally relevant states of dysprosium". In: *Physical Review A* 81.5 (2010), p. 052515. DOI: 10.1103/PhysRevA.81.052515.

[74] M. A. Hohensee et al. "Limits on violations of Lorentz symmetry and the Einstein equivalence principle using radio-frequency spectroscopy of atomic dysprosium". In: (2013).

[75] A. Cingöz et al. "Collisional perturbation of radio-frequency E1 transitions in an atomic beam of dysprosium". In: *Physical Review A* 72.6 (2005), p. 063409. DOI: 10.1103/PhysRevA.72.063409.

[76] Holger Müller et al. "Offset compensation by use of amplitude-modulated sidebands in optical frequency standards". In: *Optics Letters* 28.22 (2003), p. 2186. DOI: 10.1364/OL.28.002186.

[77] M. S. Safronova, Dansha Jiang, and U. I. Safronova. "Blackbody radiation shift in the ˆ{87}Rb frequency standard". In: *Physical Review A* 82.2 (2010), p. 022510. DOI: 10.1103/PhysRevA.82.022510.

[78] C. T. M. Weber, N. Leefer, and D. Budker. "Investigation of ac-Stark shifts in excited states of dysprosium in a search for variation of the fine-structure constant". In: ().

[79] V. V. Flambaum. "Variation of the fundamental constants: theory and observations". In: *International Journal of Modern Physics A* 22.27 (2007), pp. 4937–4950. DOI: 10.1142/S0217751X07038293.

[80] J. C. Berengut et al. "Proposed Experimental Method to Determine α Sensitivity of Splitting between Ground and 7.6eV Isomeric States in Th229". In: *Physical Review Letters* 102.21 (2009), p. 210801. DOI: 10.1103/PhysRevLett.102.210801.

[81] J. C. Berengut et al. "Optical Transitions in Highly Charged Californium Ions with High Sensitivity to Variation of the Fine-Structure Constant". In: *Physical Review Letters* 109.7 (2012), p. 070802. DOI: 10.1103/PhysRevLett.109.070802.

[82] W. Misner, K. S. Thorne, and J. A. Wheeler. *Gravitation*. San Francisco: Freeman, 1970.

[83] Thibault Damour. "Testing the equivalence principle: why and how?" In: *Classical and Quantum Gravity* 13.11A (1996), A33–A41. DOI: 10.1088/0264-9381/13/11A/005.

[84] V. Alan Kostelecký and Neil Russell. "Data tables for Lorentz and CPT violation". In: *Reviews of Modern Physics* 83.1 (2011), pp. 11–31. DOI: 10.1103/RevModPhys.83.11.

[85] Clifford M. Will. "The Confrontation between General Relativity and Experiment". In: *Living Reviews in Relativity* 9 (2006). DOI: 10.12942/lrr-2006-3.

[86] V. Alan Kostelecký and Jay Tasson. "Matter-gravity couplings and Lorentz violation". In: *Phys. Rev. D* 016013 (2010), p. 59. DOI: 10.1103/PhysRevD.83.016013.

[87] V. A. Dzuba, V. V. Flambaum, and I B Khriplovich. "Enhancement of P- and T-nonconserving effects in rare-earth atoms". In: *Zeitschrift für Physik D Atoms, Molecules and Clusters* 1.3 (1986), pp. 243–245. DOI: 10.1007/BF01436678.

[88] V. A. Dzuba, V. V. Flambaum, and M. Kozlov. "Calculation of the weak interactions in dysprosium". In: *Physical Review A* 50.5 (1994), pp. 3812–3817. DOI: 10.1103/PhysRevA.50.3812.

[89] V. A. Dzuba, V. V. Flambaum, and M. Marchenko. "Relativistic effects in Sr, Dy, Yb II, and Yb III and search for variation of the fine-structure constant". In: *Physical Review A* 68.2 (2003), p. 022506. DOI: 10.1103/PhysRevA.68.022506.

[90] B. Altschul. "Laboratory bounds on electron Lorentz violation". In: *Physical Review D* 82.1 (2010), p. 016002. DOI: 10.1103/PhysRevD.82.016002.

[91] R. Vessot et al. "Test of Relativistic Gravitation with a Space-Borne Hydrogen Maser". In: *Physical Review Letters* 45.26 (1980), pp. 2081–2084. DOI: 10.1103/PhysRevLett.45.2081.

[92] Robert Bluhm et al. "Clock-Comparison Tests of Lorentz and CPT Symmetry in Space". In: *Physical Review Letters* 88.9 (2002), p. 090801. DOI: 10.1103/PhysRevLett.88.090801.

[93] B. Altschul, Quentin G. Bailey, and V. Alan Kostelecký. "Lorentz violation with an antisymmetric tensor". In: *Physical Review D* 81.6 (2010), p. 065028. DOI: 10.1103/PhysRevD.81.065028.

[94] N. Leefer et al. "New limits on variation of the fine-structure constant using atomic dysprosium". In: (2013), p. 5.

[95] Ch. Eisele, a. Nevsky, and S. Schiller. "Laboratory Test of the Isotropy of Light Propagation at the 10-17 Level". In: *Physical Review Letters* 103.9 (2009), p. 090401. DOI: 10.1103/PhysRevLett.103.090401.

[96] F. Klinkhamer and M. Schreck. "New two-sided bound on the isotropic Lorentz-violating parameter of modified Maxwell theory". In: *Physical Review D* 78.8 (2008), p. 085026. DOI: 10.1103/PhysRevD.78.085026.

[97] Keith D. Bonin and Michael A. Kadar-Kallen. "Linear Electric-Dipole Polarizabilities". In: *International Journal of Modern Physics B* 08.24 (1994), pp. 3313–3370. DOI: 10.1142/S0217979294001391.

[98] D. R. Dounas-Frazer et al. "Measurement of dynamic Stark polarizabilities by analyzing spectral line shapes of forbidden transitions". In: *Physical Review A* 82.6 (2010), p. 062507. DOI: 10.1103/PhysRevA.82.062507.

[99] M. Auzinsh, D. Budker, and S. M. Rochester. *Optically polarized atoms*. Oxford University Press, 2010.

[100] Filippo Levi et al. "Measurement of the blackbody radiation shift of the ˆ{133}Cs hyperfine transition in an atomic fountain". In: *Physical Review A* 70.3 (2004), p. 033412. DOI: 10.1103/PhysRevA.70.033412.

[101] W M Itano, L. Lewis, and D. J. Wineland. "Shift of ˆ{2}S_{1/2} hyperfine splittings due to blackbody radiation". In: *Physical Review A* 25.2 (1982), pp. 1233–1235. DOI: 10.1103/PhysRevA.25.1233.

A — Frequency measurements

During data collection the 564-nm fluorescence light emitted by Dy atoms during the final decay step of level A to the ground state is detected with a photomultiplier tube (PMT). The PMT signal is sent to a lock-in amplifier that detects the signal components at the first and second harmonics of the modulation frequency. The theory of lock-in detection is briefly summarized in Sec. C.1. The lock-in amplifier, a Signal Recovery 7280, simultaneously detects both the in-phase and quadrature components of both harmonic signals. This allows the lock-in phase to be adjusted post-data collection by application of Eq. (C.17).

A measurement of the transition frequency occurs in two steps. The probe electric-field frequency is first scanned across a ~ 4 kHz range around resonance. Lock-in detected signals from such a scan are shown in Fig. A.1. Close to resonance the first and second-harmonic signals are well described by linear and constant functions, respectively. The ratio of first-harmonic to second-harmonic signals are fit to the function

$$R_\phi(\omega) = \frac{L^1_\phi(\omega)}{L^2(\omega)} = \frac{\mathcal{M}_\phi}{2\pi}(\omega - \omega_0), \tag{A.1}$$

where the transition frequency is assumed to be $\omega = \omega_0$ where $R(\omega_0) = 0$. The phase dependence of $L^2(\omega)$ is ignored as the second-harmonic detection phase is simply chosen to maximize signal size at resonance. The ratio of harmonics is chosen as it is expected to be insensitive to changes in the overall signal size, due to fluctuations in the atomic beam density, laser power, or rf power.

A measurement of the slope M_ϕ is referred to as the calibration. After calibration the electric-field frequency is set to a fixed value $\omega_{\rm rf}$ near ω_0 and the ratio $R_\phi(\omega_{\rm rf})$ acquired repeatedly. The transition frequency is calculated from the mean of the repeated measurements according to

$$\Delta\omega_0^\phi = \frac{\omega_0 - \omega_{\rm rf}}{2\pi} = \frac{-1}{\mathcal{M}_\phi}\frac{1}{N}\sum_i^N R^i_\phi(\omega_{\rm rf}). \tag{A.2}$$

The statistical uncertainty, corresponding to the half 68% confidence interval, for a measurement of $\Delta\omega_0$ is taken to be the standard error of the mean,

$$\overline{\sigma}(\Delta\omega_0^\phi) = \frac{\sigma(\Delta\omega_0^\phi)}{\sqrt{N-1}}, \tag{A.3}$$

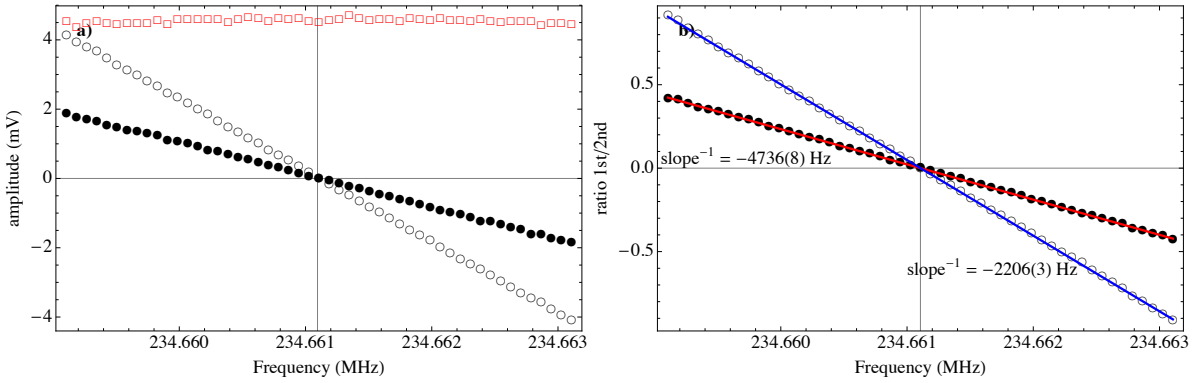

Figure A.1: a) Filled and empty circles show the in-phase and quadrature first-harmonic lock-in signals as the electric field frequency is scanned across the atomic resonance. Empty squares show the magnitude of the second-harmonic lock-in signals. b) Filled (empty) circles show the ratio of the in-phase (quadrature) first harmonic to second-harmonic lock-in signals. The reference phase of the first-harmonic channel was 60.7° for these data.

where $\sigma(\Delta\omega_0^\phi)$ is the standard deviation of the frequency measurements and assumed normally distributed measurement errors.

We have kept the dependence on phase explicit to demonstrate that acquiring data at the in-phase and quadrature channels of the lock-in amplifier allows the data to be rephased after acquisition has been performed. According to Eqs. (A.1), (A.2), and (C.17) the transition frequency at any phase ϕ can be calculated according to

$$\Delta\omega_0^\phi = \frac{-1}{\mathcal{M}_\phi}\frac{1}{N}\sum_i^N R^i_{\phi_0}(\omega_{\rm rf})\cos(\phi-\phi_0) + R^i_{\phi_0+\pi/2}(\omega_{\rm rf})\sin(\phi-\phi_0), \tag{A.4}$$

where

$$\mathcal{M}_\phi = \mathcal{M}_{\phi_0}\cos(\phi-\phi_0) + \mathcal{M}_{\phi_0+\pi/2}\sin(\phi-\phi_0). \tag{A.5}$$

The quantities $\mathcal{M}_{\phi_0}$ and $R^i_{\phi_0}$ are the in-phase slope and ratio at phase ϕ_0, and $\mathcal{M}_{\phi_0+\pi/2}$ and $R^i_{\phi_0+\pi/2)}$ are the quadrature slope and ratio at phase ϕ_0. Figure A.2 demonsrates the application of Eq. (A.4) to actual data, where the in-phase and quadrature slopes $\mathcal{M}$ were taken from Fig. A.1. Data acquisition at the RAM insensitive phase, discussed in Sec. 4.1, comes at the expense of more than a factor of two in statistical sensitivity.

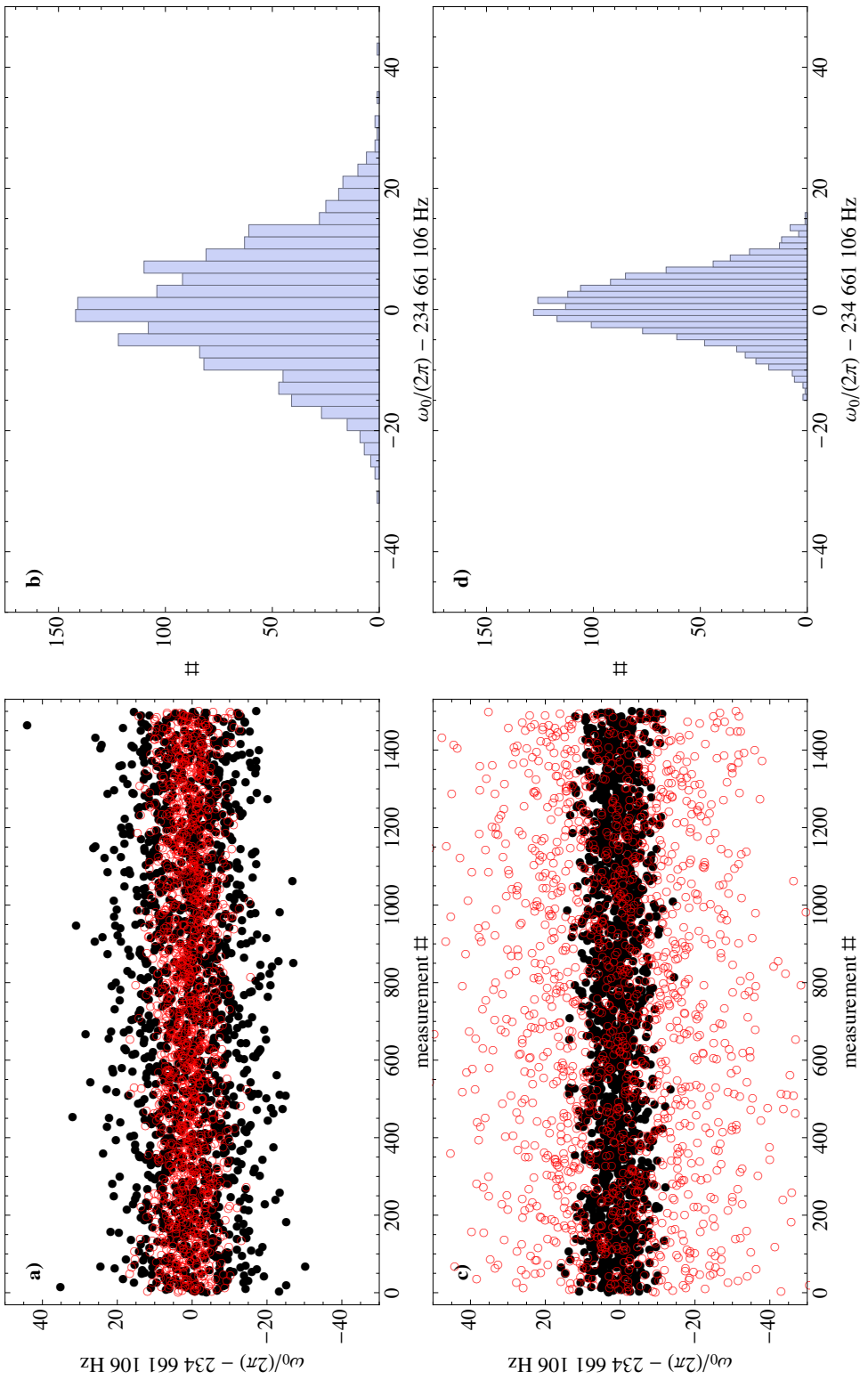

Figure A.2: **a)** In-phase (filled circles) and quadrature (empty circles) frequency measurements with the first-harmonic reference set to the RAM insensitive phase, $\phi = 60.7°$. **b)** Histogram of the corresponding in-phase frequency measurements, where $\Delta\omega_0 = 0.51(20)$ Hz. **c)** In-phase (filled circles) and quadrature (empty circles) frequency measurements with the first-harmonic reference set to the most sensitive phase, $\phi = -42°$. **d)** Histogram of the corresponding in-phase frequency measurements, where $\Delta\omega_0 = 0.82(9)$ Hz. Note that **a)** and **c)** use the same data, with the phase adjusted according to Eq. (A.4).

B — Unresolved Zeeman structure

The Zeeman structure of the $B \to A$ transition in our experiment is unresolved, as demonstrated in Fig. B.1. Selection rules allow 20 transitions between the $J = 10$ levels for a given electric-field polarization ($M = 0 \to M' = 0$ is forbidden for $\Delta J = 0$). In our experiment we define the quantization axis along the electric-field axis. With this geometry we observe only the $\Delta m = 0$ transitions. The expression for an unresolved lineshape can be written

$$\mathcal{K}(\omega) = \sum_M a_M K_M(\omega), \tag{B.1}$$

where ω is the electric-field frequency (angular) and a_M is the normalized weight of the $M_B = M \to M_A = M$ transition, determined by transition strengths and sublevel populations. The individual lineshapes $K_m(\omega)$ are arbitrary, but we will assume Lorentzians of the form

$$K_M(\omega) = \frac{\gamma^2/4}{(\omega - \omega_M)^2 + \gamma^2/4}, \tag{B.2}$$

where ω_M is the resonant frequency of the M-sublevel transition, γ is the full-width half-maximum (FWHM) linewidth of the transition, and the lineshape has been normalized to unity at resonance.

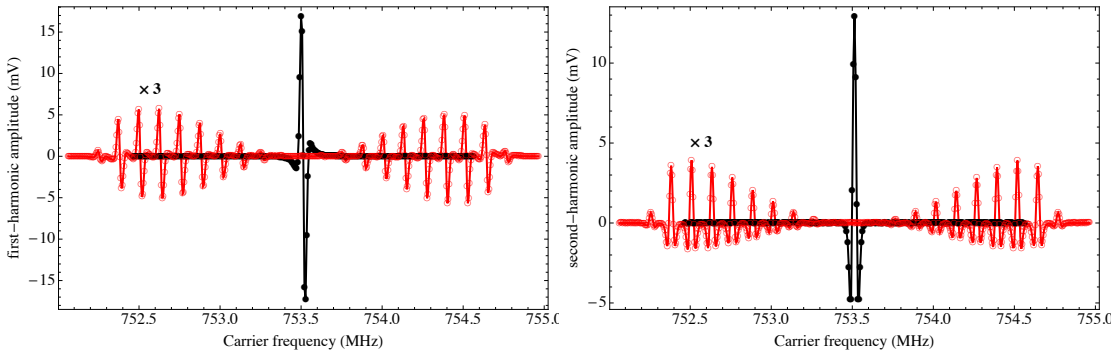

Figure B.1: The left and right plots show the first- and second-harmonic lineshapes of the ^{164}Dy transition with no magnetic field (filled circles) and ~ 575 mG magnetic field (empty circles). The resolved spectrum has been scaled on the vertical axis $3\times$ for display purposes.

The resonant frequency of a transition is taken to be the frequency at which the lineshape amplitude is maximum, or when the first derivative of the lineshape is zero,

$$\left.\frac{d\mathcal{K}}{d\omega}\right|_{\omega_o} = \sum_M a_M \frac{-2(\omega_o - \omega_M)\gamma^2/4}{((\omega_o - \omega_M)^2 + \gamma^2/4)^2} = 0, \tag{B.3}$$

where ω_o is the observed transition frequency. There is more than one solution to Eq. (B.3), but only one that corresponds to the maximum of $\mathcal{L}(\omega)$. In order to find this frequency we assume the sublevel dependent shifts are small, i.e. $|\omega_o - \omega_M| \ll \gamma/2$ for all M. We now expand Eq. (B.3), retaining terms up to order $(\omega_o - \omega_M)/\gamma$,

$$\begin{aligned}\left.\frac{d\mathcal{K}}{d\omega}\right|_{\omega_o} &\simeq \sum_M a_M \frac{-8(\omega_o - \omega_M)}{\gamma^2} = 0 \\ &\simeq \sum_M a_M \left(\omega_o - \omega_M\right) = 0.\end{aligned}$$

This has the solution

$$\omega_o = \sum_M a_M \omega_M, \tag{B.4}$$

which is simply the weighted average of the indidual Zeeman transition frequencies. A practical study of systematics on an unresolved line therefore requires knowledge of the individual Zeeman transition weights. Any effect, *e.g.* the Stark and Zeeman effects, that depend on M must take this distribution into account.

The Zeeman transition weights have been measured by applying a ~ 575 mG magnetic field along the quantization axis to completely resolve the Zeeman structure. A frequency-modulated, rf electric field is scanned across the spectrum while a photomultiplier (PMT) tube detects the atomic fluorescence at 564 nm. A lock-in detector measures the amplitude of the PMT signal contained at the first and second-harmonics of the modulation frequency. An example scan is shown in Fig. B.1.

A nonlinear least-squares fit is performed to both harmonics of the spectrum using an analytic lineshape of the form

$$\mathcal{K}(\omega) = \sum_{M\neq 0} a_M L_\phi^n \left(\omega - (\omega_{AB} + G\cdot m)\right),$$

where $M = -10 \to 10$, the a_M are normalized transition weights, $\omega_{AB}/(2\pi) \simeq 753.5$ MHz is the unshifted transition frequency, $G/(2\pi) \sim 0.126$ MHz is the magnetic field induced Zeeman splitting, ϕ is the lock-in detector phase, and n indicates the lock-in detector harmonic. The derivation of the lineshape L_ϕ^n for arbitrary harmonic can be found in Section C, Eq. (C.20). The fitting is performed on the first and second harmonics of four Zeeman spectra, giving eight measurements of the transition weights. The fits are shown in Fig. B.2 and normalized weights are shown in Table B.1.

$\|M\|$	1	2	3	4	5	6	7	8	9	10
+	0.0010(1)	0.0062(4)	0.018(1)	0.036(2)	0.056(2)	0.076(1)	0.0927(4)	0.103(2)	0.091(4)	0.016(1)
−	0.0010(1)	0.0061(5)	0.018(1)	0.036(2)	0.057(2)	0.078(2)	0.0949(3)	0.105(2)	0.093(4)	0.016(1)

Table B.1: Normalized weights of the $\pm m$ sublevels contributing to the unresolved lineshape of the $B \rightarrow A$ transition in Dy.

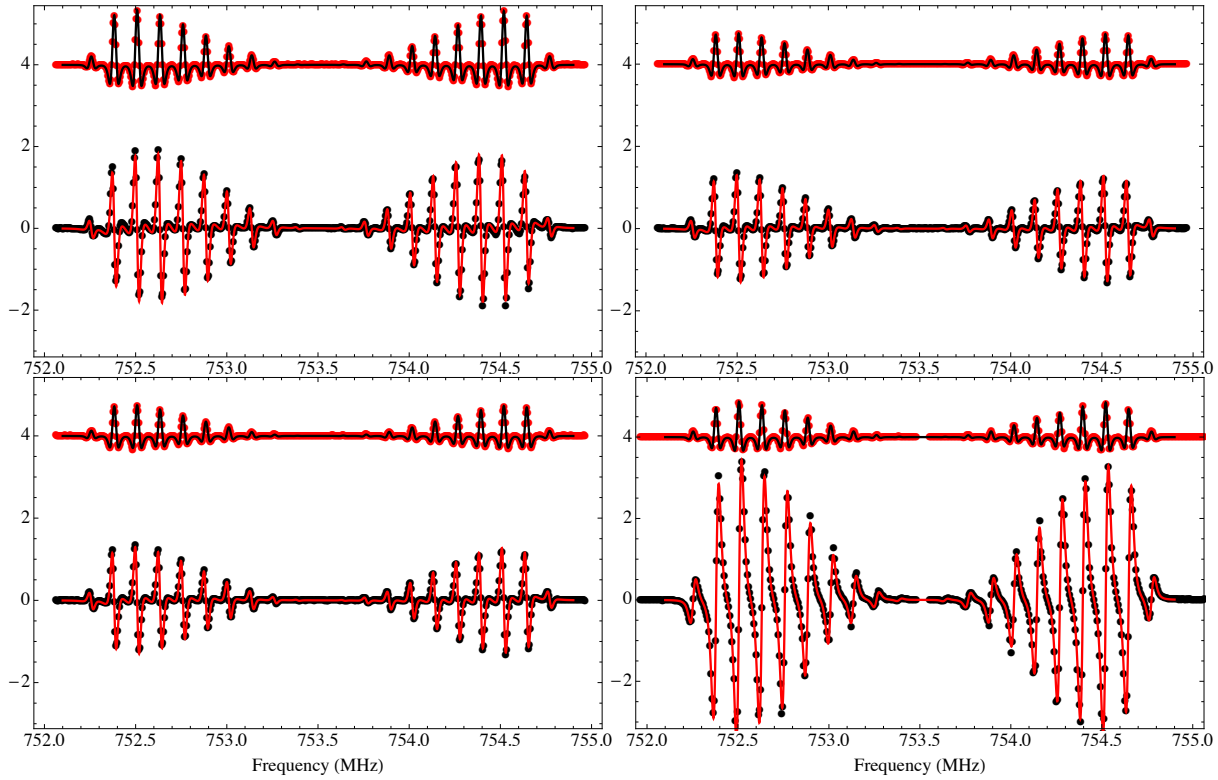

Figure B.2: The ^{164}Dy transition with resolved Zeeman structure. The top and bottom spectra are the second and first-harmonics, respectively, of the lock-in detected lineshapes. The solid lines are the results of nonlinear least-squares fits using the analytic lineshapes derived in the following section.

C — Lineshape derivation

C.1 Frequency- and amplitude modulated spectroscopy

The radio-frequency spectroscopy of Dy is performed with a frequency-modulated electric field. Frequency modulation of the electric field gives rise to amplitude modulation of the atomic fluorescence, with a phase determined by the detuning of the electric-field carrier frequency from the atomic resonance. A lock-in amplifier is used to perform phase-sensitive detection (PSD) of the fluorescence with a high level of noise rejection. In this section we derive analytic functions to describe the fluorescence lineshapes.

Electric-field frequency spectrum

The electric field used for spectroscopy has the form

$$E(t) = E_o[1 + \epsilon \cos(\Omega t + \phi_{AM})] \cos(\omega t + m \sin \Omega t), \tag{C.1}$$

where E_o is the elctric field amplitude, ϵ is a measure of RAM, ω and Ω are the carrier and modulation frequencies, respectively, and ϕ_{AM} is an arbitrary phase between the amplitude and frequency modulations. To simplify calculations we use Euler's formula to write

$$E(t) = \frac{E_o}{2}\left[1 + \frac{\epsilon}{2}\left(e^{i(\Omega t+\phi)} + e^{-i(\Omega t+\phi)}\right)\right] \cdot \left(e^{i(\omega t + m \sin \Omega t)} + e^{-i(\omega t + m \sin \Omega t)}\right). \tag{C.2}$$

This expression can be simplified further by using the Jacobi-Anger expansion,

$$e^{im \sin \theta} = \sum_{k=-\infty}^{\infty} J_k(m) e^{ik\theta},$$

where $J_k(m)$ is the k-th Bessel function. Applying this expansion yields

$$E(t) = \frac{E_o}{2}\left[1 + \frac{\epsilon}{2}\left(e^{i\Omega t}e^{i\phi} + e^{-i\Omega t}e^{-i\phi})\right)\right] \cdot \left(e^{i\omega t}\sum_{k=-\infty}^{\infty} J_k(m) e^{ik\Omega t} + e^{-i\omega t}\sum_{k=-\infty}^{\infty} J_k(m) e^{-ik\Omega t}\right).$$

The fully simplified expression is

$$E(t) = \frac{E_o}{2} \sum_{k=-\infty}^{\infty} \left[e^{i\omega t}\ G_k(m) e^{ik\Omega t} + e^{-i\omega t} G_k^*(m) e^{-ik\Omega t} \right], \tag{C.3}$$

where

$$G_k(m) = J_k(m) + \frac{\epsilon}{2} \left(J_{k-1}(m) e^{i\phi} + J_{k+1}(m) e^{-i\phi} \right). \tag{C.4}$$

Equation (C.3) is identical to the expression for a purely frequency- or phase-modulated electric field, with the regular Bessel functions, $J_k(m)$, replaced by the complex valued $G_k(m)$ defined by Eq. (C.4).

Two-level system

To derive the expected lineshape we consider a two-state Hamiltonian

$$\mathbf{H} = \begin{pmatrix} \omega_0 - i\frac{\gamma}{2} & d\,E(t) \\ d\,E^*(t) & 0 \end{pmatrix}, \tag{C.5}$$

to describe the two-state system

$$|\psi(t)\rangle = \begin{pmatrix} A(t) e^{-i(\omega_0 - i\gamma/2)t} \\ B(t) \end{pmatrix}, \tag{C.6}$$

where d is the dipole-matrix element between states A and B, ω_0 is the (positive) energy difference between A and B, and γ is the relaxation rate of state A.

Atoms in our experiment start in state B and are excited to state A. The atomic fluorescence at 564 nm is directly proportional to the population of state A, that is $P_A(t) = |\langle A|\psi(t)\rangle|^2$. To first find $A(t)$ we need to solve the Schrödinger equation

$$i\frac{\partial|\psi(t)\rangle}{\partial t} = \mathbf{H}|\psi(t)\rangle. \tag{C.7}$$

After substituting Eq. (C.6) and Eq.(C.5) in to Eq.(C.7) we get

$$i\frac{dA(t)}{dt} e^{-i(\omega_0 - i\gamma/2)t} = E(t)B(t) \tag{C.8}$$

$$i\frac{dB(t)}{dt} = E^*(t)A(t)e^{-i(\omega_0 t - i\gamma t/2)}. \tag{C.9}$$

As a first approximation we will assume that the population of atoms in state B is relatively unchanged, $B(t) \approx 1$. This leaves us with a linear equation for $A(t)$ given by

$$\frac{dA(t)}{dt} = -iE(t)e^{i(\omega_0 t - i\gamma t/2)}. \tag{C.10}$$

The solution $A(t)$ for a an electric field $E(t) = E_0 e^{i\omega t}$ is

$$A(t) = \frac{-E_0}{\omega + \omega_0 - i\gamma/2} \left(e^{i(\omega+\omega_0-i\gamma/2)t} - 1 \right), \tag{C.11}$$

and the quantity $\langle A|\psi(t)\rangle$ is

$$\begin{aligned} \langle A|\psi(t)\rangle &= A(t) e^{-i(\omega_0 - i\gamma/2)t} \\ &= \frac{-E_0}{\omega + \omega_0 - i\gamma/2} \left(e^{i\omega t} - e^{-i(\omega_0 - i\gamma/2)t} \right). \end{aligned} \tag{C.12}$$

We will define the transfer function $T(\omega) = -1/(\omega + \omega_0 - i\gamma/2)$. The solution for $\langle A|\psi(t)\rangle$ is linear in the electric field $E(t)$, and the frequency- and amplitude-modulated field from Eq. (C.3) is a simple sum over discrete oscillatory terms. The solution for the full electric field then requires making the replacement in Eq. (C.12) $\omega \to (\omega + k\Omega)$ and $E_0 \to E_0/2\, G_k(m)$, adding another term with $\omega \to -(\omega + k\Omega)$ and $E_0 \to E_0/2\, G_k^*(m)$, and summing the entire expression over k:

$$\begin{aligned} \langle A|\psi(t)\rangle = \frac{E_0}{2} \sum_k \Big[& T(\omega + k\Omega) G_k(m) \left(e^{i(\omega+k\Omega)t} - e^{-i(\omega_0 - i\gamma/2)t} \right) + \\ & T(-\omega - k\Omega) G_k^*(m) \left(e^{-i(\omega+k\Omega)t} - e^{-i(\omega_0 - i\gamma/2)t} \right) \Big]. \end{aligned} \tag{C.13}$$

The steady state population $P_A(t) = |\langle A|\psi(t)\rangle|^2$ is

$$\begin{aligned} P_A(t) \approx \frac{E_0^2}{4} \sum_{kk'} \Big[& T(\omega + k\Omega) G_k(m) T^*(\omega + k'\Omega) G_{k'}^*(m) e^{i(k-k')\Omega t} + \\ & T(-\omega - k\Omega) G_k^*(m) T^*(-\omega - k'\Omega) G_{k'}(m) e^{i(k'-k)\Omega t} \Big] \end{aligned} \tag{C.14}$$

after dropping damped terms ($t \gg 0$) and ignoring rapidly oscillating terms around 2ω. If we assume positive frequencies such that $\omega > 0$, the term $T(\omega + k\Omega)T^*(\omega + k'\Omega)$ is in general a small number and we can write

$$\boxed{P_A(t) \approx \frac{E_0^2}{4} \sum_{kk'} T(-\omega - k\Omega) T^*(-\omega - k'\Omega) G_{k'}(m) G_k^*(m) e^{i(k'-k)\Omega t}.} \tag{C.15}$$

Lock-in detection

A lock-in amplifier is a phase-sensitive amplifier that takes an input signal $f(t)$ and provides the output

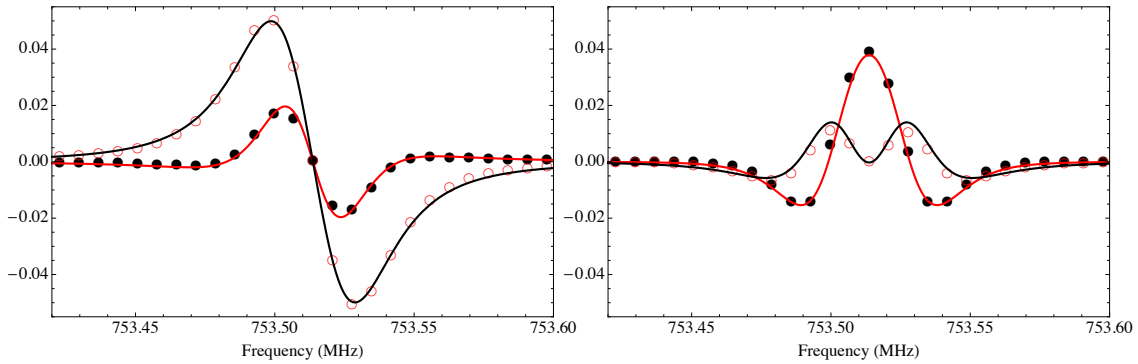

Figure C.1: First- and second-harmonic lineshapes of the ^{164}Dy transition are shown in the left and right panels, respectively. The second-harmonic has been scaled up by 3× for display purposes. For each harmonic, a single fit is performed on the combined in-phase (filled circles) and quadrature (empty circles) data. The quadrature lineshape is constrained to have the same fit parameters as the in-phase lineshape, but with a $\pi/2$ offset added to the detection phase parameter.

$$L^n(\phi) = \frac{1}{T}\int f(t)\cos\left(n\Omega t + \phi\right) dt \tag{C.16}$$

where Ω is a reference frequency, typically a multiple of some modulation frequency, n specifies the detection harmonic of the reference frequency, and T is the integration time (implied in the integration limits). An arbitrary phase, $\delta\phi$ can be added to the reference waveform such that

$$L^n(\phi + \delta\phi) = L_n(\phi)\cos\delta\phi + L_n(\phi + \pi/2)\sin\delta\phi. \tag{C.17}$$

The signals $L^n(\phi)$ and $L^n(\phi+\pi/2)$ are commonly referred to as the in-phase and quadrature amplitudes for a particular phase ϕ. Equation (C.17) shows that measuring both the in-phase and quadrature components allows a calculation of the lock-in signal at any arbitrary phase.

We now consider the lock-in amplifier outputs obtained from Eq. (C.15) for arbitrary harmonic n of the modulation frequency:

$$\begin{aligned} L^n(\phi) =& \frac{1}{2T}\int P_A(t)\left(e^{in\Omega t}e^{i\phi} + e^{-in\Omega t}e^{-i\phi}\right) dt \\ =& \frac{E_0^2}{8T}\int \sum_{kk'} T(-\omega - k\Omega)T^*(-\omega - k'\Omega)G_{k'}(m)G_k^*(m)\cdot \\ & \left(e^{i(k'-k+n)\Omega t}e^{i\phi} + e^{i(k'-k-n)\Omega t}e^{-i\phi}\right) dt. \end{aligned} \tag{C.18}$$

We assume that the finite integration time of the lock-in amplifier is long enough to make us of the identity $(1/T)\int e^{i(m-n)\Omega t}dt = \delta_{m,n}$. The final result is

$$\begin{aligned} L_\phi^n(\omega) &= \frac{E_0^2}{8}\sum_{kk'} T(-\omega - k\Omega)T^*(-\omega - k'\Omega)G_{k'}(m)G_k^*(m)\left(\delta_{k',k-n}e^{i\phi} + \delta_{k',k+n}e^{-i\phi}\right) \\ &= \frac{E_0^2}{8}\sum_{k} T(-\omega - k\Omega)T^*(-\omega - (k-n)\Omega)G_{k-n}(m)G_k^*(m)e^{i\phi} + \\ &\qquad T(-\omega - k\Omega)T^*(-\omega - (k+n)\Omega)G_{k+n}(m)G_k^*(m)e^{-i\phi}. \end{aligned} \tag{C.19}$$

The infinite sum in Eq. (C.19) allows us to substitute $k \to k+n$ in the first term only, allowing us to write

$$\begin{aligned} L_\phi^n(\omega) &= \frac{E_0^2}{8}\sum_{k} T(-\omega - (k+n)\Omega)T^*(-\omega - k\Omega)G_k(m)G_{k+n}^*(m)e^{i\phi} + \\ &\qquad T(-\omega - k\Omega)T^*(-\omega - (k+n)\Omega)G_{k+n}(m)G_k^*(m)e^{-i\phi} \\ L_\phi^n(\omega) &= \boxed{\frac{E_0^2}{4}\sum_{k} \mathrm{Re}\left\{T\left(-\omega - (k+n)\Omega\right)T^*(-\omega - k\Omega)G_k(m)G_{k+n}^*(m)e^{i\phi}\right\}.} \end{aligned} \tag{C.20}$$

An example of a nonlinear least-squares fit of Eq. (C.20) to sample lineshapes is shown in Fig. C.1.